Gravity effect on liquid film hydrodynamics and spray cooling

Vom Fachbereich Maschinenbau
an der Technischen Universität Darmstadt
zur
Erlangung des Grades eines Doktor-Ingenieurs (Dr.-Ing.)
genehmigte

Dissertation

vorgelegt von

Dipl.-Ing. Olympia Natalia Kyriopoulos

aus Darmstadt

Berichterstatter:	Priv.-Doz. Dr.-Ing. habil. I.V. Roisman, TU Darmstadt
Mitberichterstatter:	Prof. Dr.-Ing. C. Tropea, TU Darmstadt
Mitberichterstatter:	Prof. Dr.-Ing. A. Moreira, Instituto Superior Técnico
Tag der Einreichung:	04.05.2010
Tag der mündlichen Prüfung:	21.06.2010

Darmstadt 2010
D17

Eidesstattliche Erklärung

Hiermit erkläre ich an Eides statt, dass ich die vorliegende Dissertation selbständig verfasst und keine anderen als die von mir angegebenen Hilfsmittel verwendet habe. Ich erkläre außerdem, dass ich bisher noch keinen Promotionsversuch unternommen habe.

Darmstadt, den 04. Mai 2010

Olympia Kyriopoulos

Abstract

Spray-wall interaction is a key element in a multitude of technologies. It occurs in numerous industrial applications such as in internal combustion engines, gas turbines, spray drying, spray coating and cooling. A large diversity of phenomena is associated with the flow in the liquid layer initiated by single drop impacts onto a wall and their interactions. Due to the complexity of the problem, the hydrodynamics of liquid films created by sprays and the associated heat transfer are not entirely understood. Current approaches, usually presented in the form of empirical correlations or developed as a simple superposition of single drop impacts, disregard completely the physics of spray wall interaction. No reliable model describing reliably the behavior of the liquid film or predicting the effectiveness of spray cooling has been developed to date. The main difficulty in spray research is the fact that most sprays are usually polydisperse. Their behavior is governed by a large number of parameters which cannot be varied and controlled independently. Thus, it is not easy to identify the main influencing parameters or their combinations which define the problem.

This thesis is devoted to the dynamics of a liquid film produced by normal spray impact onto a heated target. It is aimed at a better understanding the hydrodynamics and heat transfer associated with spray impact onto a heated target and at providing a basis for the modeling of spray cooling. Further progress in this field of research is achieved by performing experiments for diverse spray parameters and under various gravity conditions. The experiments under microgravity conditions are performed during parabolic flights and on board a ballistic rocket. Additionally, experiments have been performed with varied gravity levels, between -20g to +20g, in a centrifuge.

Spray propagation and spray-wall interaction are observed using high-speed visualization under various gravity levels and various volumetric rates. The characteristic spray parameters are then determined with the help of image processing. Complementary to this, the spray is characterized using the phase Doppler instrument in the laboratory. To study the liquid film hydrodynamics, a robust method is developed to determine a typical film thickness created by spray impact. In addition, the heat transfer mechanisms involved in the spray-wall interaction are outlined. Heat fluxes are measured for various spray impact parameters and target temperatures. The influence of gravity, film thickness and other parameters on spray-wall interaction and spray cooling are discussed.

Based on the collected data, a sound basis for reliable modeling of spray cooling is provided and validated by comparison with other experimental data from the literature. Semi-empirical models are proposed for the secondary spray as well as for the characteristic film thickness. The values of the typical film thickness are then used for description of the spray cooling efficiency.

Kurzfassung

Spray-Wand-Wechselwirkung ist ein Schlüsselelement in einer Vielzahl von Technologien. Sie tritt in zahlreichen Industrieanwendungen auf, wie beispielsweise in Verbrennungsmotoren, Gasturbinen, Sprühtrocknung, -beschichtung und -kühlung. Eine große Vielfalt von Phänomenen ist mit der Filmströmung verbunden, initiiert durch den Aufprall einzelner Tropfen auf eine beheizte Wand und deren Interaktionen. Aufgrund der Komplexität des Problems ist die Hydrodynamik der Flüssigkeitsfilme erzeugt durch Sprays nicht vollständig nachvollzogen. Derzeitige Ansätze, in der Regel dargelegt in Form von empirischen Korrelationen oder entwickelt als Superposition einzelner Tropfenaufpralle, missachten die Physik der Spray-Wand-Wechselwirkung. Bislang wurde kein Modell entwickelt, das zuverlässig das Verhalten des Flüssigkeitsfilms beschreibt oder die Effektivität von Sprühkühlung voraussagt. Diese sind bestimmt durch eine Vielzahl von Parametern, die nicht voneinander unabhängig variiert und geregelt werden können. Folglich ist es nicht einfach, die hauptsächlichen Einflussfaktoren oder deren Kombinationen zu identifizieren, die dieses Problem definieren.

Die vorliegende Dissertation widmet sich der Dynamik des Flüssigkeitsfilms erzeugt durch Sprayaufprall auf eine beheizte Oberfläche. Das allgemeine Ziel der Untersuchungen liegt darin, die Hydrodynamik und die Wärmeübertragung beim Sprayaufprall auf einer beheizten Oberfläche besser zu verstehen und eine Grundlage für eine Modellierung von Spraykühlung zu schaffen. Weiterer Fortschritt auf diesem Gebiet wurde durch das Durchführen von Experimenten unter diversen Sprayparametern und unter verschiedenen Gravitationsbedingungen erreicht. Versuche unter Mikrogravitation wurden während Parabelflügen und an Bord einer Forschungsrakete realisiert. Zudem wurden Experimente im Bereich von -20g bis +20g in einer Zentrifuge durchgeführt.

Sprayausbreitung und Spray-Wand-Wechselwirkung werden mit Hilfe von Hochgeschwindigkeitsaufnahmen unter verschiedenen Gravitationsbedingungen sowie unterschiedlichen Durchflüssen beobachtet. Charakteristische Sprayparameter werden mit Hilfe von Bildbearbeitung bestimmt. Ergänzend wird das Spray mittels der Phasen Doppler Technik charakterisiert. Zur Untersuchung der Flüssigkeitsfilmhydrodynamik wird eine robuste Methode entwickelt, die eine typische Filmdicke, erzeugt durch Sprayaufprall, bestimmt. Zudem werden Wärmeübertragungsmechanismen umrissen, die an der Spray-Wand-Wechselwirkung beteiligt sind. Wärmestromdichten werden für unterschiedliche Sprayparameter und Wandtemperaturen gemessen. Der Einfluss von Gravitation, Filmdicke und weiterer Parameter auf die Spray-Wand-Wechselwirkung sowie auf Sprühkühlung werden diskutiert.

Basierend auf die gewonnenen Daten, wird eine solide Grundlage für eine zuverlässige Modellierung von Sprühkühlung bereitgestellt und beim Vergleich mit anderen experimentellen Daten aus der Literatur bestätigt. Es werden halbempirische Modelle sowohl für das Sekundärspray als auch für die charakteristische Filmdicke aufgestellt. Typische Filmdickenwerte werden zur Beschreibung der Sprühkühlungseffizienz verwendet.

Acknowledgements

My sincere gratitude goes to Prof. Dr.-Ing. Cameron Tropea and to Priv.-Doz. Dr.-Ing. habil. Ilia Roisman for supervising my work and being a source of inspiration. I am also indebted to Prof. Dr.-Ing. Peter Stephan and Priv.-Doz. Dr.-Ing. habil. Tatiana Gambaryan-Roisman for their scientific advice. My special thanks go to Prof. Dr.-Ing. Antonio Moreira for his willingness to be my referee.

This work has been performed in the framework of the research grant of BMWi "Sprayaufprall auf beheizte Oberflächen unter Mikrogravitation". Therefore, I would like to extend particular thanks to ESA and DLR for financial support. Sincere thanks also go to NOVESPACE, the DOLFIN team, all TEXUS-45 teams such as EADS Astrium GmbH, Kayser-Threde, MORABA and to the team of the centrifuge at ZARM for a constant cooperation. In addition, I would like to specially thank Stephanie Lath for her enormous assistance in the framework of this project. Further grateful thanks go to the SLA workshop, in particular to Ilona Kaufhold and Timm Geelhaar.

I appreciate the fruitful conversations with my Tuesday lunch group, the contribution of Armin Brandner, Hubert Marschall and of my students. My special thanks go to Benjamin Balewski for his tremendous support and to Monika Mühlbauer.

I would like to express grateful acknowledgments to my family for continuously encouraging me:

Θέλω να ευχαριστήσω τους Γονείς μου, που από τα πρώτα σχολικά μου χρόνια έως σήμερα δεν έπαψαν να με στηρίζουν, με την αγάπη τους και την πίστη τους γιά μένα. Οπως επίσης τις αδελφές μου, ιδιαίτερα την δίδυμη, που όποτε την χρειαζόμουν ήταν δίπλα μου.

Τὰ πάντα ῥεῖ καὶ οὐδὲν μένει.

Ἡράκλειτος ὁ Ἐφέσιος
(544 π.Χ. - 484 π.Χ.)

Contents

Nomenclature

A	$[m^2]$	area
a	$\left[\frac{m^2}{s}\right]$	thermal diffusivity
a, b	$[m]$	length of one-half of major and minor axes
c_p	$\left[\frac{J}{kgK}\right]$	specific heat capacity
D, d	$[m]$	diameter
D_{10}	$[m]$	arithmetic mean diameter
D_{32}	$[m]$	Sauter mean diameter
H	$[-]$	dimensionless wall film thickness
h	$[m]$	wall film thickness
L	$[m]$	perimeter
$\dot{m}$	$\left[\frac{kg}{s}\right]$	mass flow rate
P	$\left[\frac{J}{s}\right]$	heating power
p	$[Pa]$	pressure
$\dot{Q}$	$\left[\frac{J}{s}\right]$	heat transfer
$\dot{q}$	$\left[\frac{J}{sm^2}\right]$	heat flux
s	$[m]$	distance
t, T	$[s]$	time
T	$[K]$	temperature
u	$\left[\frac{m}{s}\right]$	velocity, axial velocity
$\dot{V}$	$\left[\frac{l}{s}\right]$	volumetric flow rate
v	$\left[\frac{m}{s}\right]$	velocity in the wall film
v, w	$\left[\frac{m}{s}\right]$	transverse velocities

x	$[m]$	measurement position
z	$[m]$	measurement distance

Dimensionless numbers

Bo	$[-]$	Bond number
Ca	$[-]$	Capillary number
Fr	$[-]$	Froude number
K	$[-]$	K-number
La	$[-]$	Laplace number
Nu	$[-]$	Nusselt number
Oh	$[-]$	Ohnesorge number
Pe	$[-]$	Péclet number
Re	$[-]$	Reynolds number
St	$[-]$	Stanton number
We	$[-]$	Weber number

Greek symbols

α	$\left[\frac{W}{m^2K}\right]$	heat transfer coefficient
α	$[rad]$	angle
ε	$[-]$	constant value
η	$\left[\frac{kg}{ms}\right]$	dynamic viscosity
θ	$[rad]$	beam intersection angle
ϑ	$\left[\frac{W}{K}\right]$	thermal conductance
κ	$[-]$	constant value
λ	$\left[\frac{W}{mK}\right]$	thermal conductivity

μg	$\left[\frac{m}{s^2}\right]$	microgravity
ν	$\left[\frac{m^2}{s}\right]$	kinematic viscosity
ρ	$\left[\frac{kg}{m^3}\right]$	density
σ	$\left[\frac{kg}{s^2}\right]$	surface tension
$+\acute{\upsilon}$g	$\left[\frac{m}{s^2}\right]$	positive hypergravity
-$\acute{\upsilon}$g	$\left[\frac{m}{s^2}\right]$	negative hypergravity
φ	$[rad]$	scattering angle
ψ	$[rad]$	elevation angle

Subscripts

$*$	modified
10	arithmetic mean
32	Sauter mean
-	average
a, b	after impact, before impact
d	distance
$drop$	drop
equ	equivalent
$film$	wall film
i, o	incoming, outgoing drops
L	lower
max, min	maximal, minimal value
min	minimal
opt	optimal
$ps, prim, p$	primary spray
ref	reference

S	saturation
sp	relation of secondary to primary spray
ss, sec	secondary spray
U	upper
v	viscous
w	wall

Abbreviations

BMWi	BundesMinisterium für Wissenschaft und Technologie
CAD	Computer Aided Design
CHF	Critical Heat Flux
DLR	Deutsches Zentrum für Luft- und Raumfahrt
DOLFIN	Dynamics Of Liquid Film/wall INteraction
EADS	European Aeronautic Defense and Space company
ESA	European Space Agency
ESRANGE	European Space and Sounding Rocket RANGE
HR	High-Resolution
HS	High-Speed
IR	InfRared
ISS	International Space Station
NASA	National Aeronautics and Space Administration
NI	National Instruments
pdf	probability density function
PDA	Phase Doppler Aemometry
PFC	Parabolic Flight Campaign
sdt	standard deviation

SMD	Sauter Mean Diameter
SR	Sounding Rocket
TEXUS	Technologische EXxperimente Unter Schwerelosigkeit
VOF	Volume Of Fluid
ZARM	Zentrum für Angewandte Raumfahrttechnologie & Mikrogravitation

List of Figures

List of Tables

Chapter 1

Introduction

1.1 Motivation

Spray impact occurs in many industrial applications involving multiphase flow of liquid drops in a gas, such as internal combustion engines, gas turbines, in agricultural and medical applications, spray drying, spray coating (including thermal plasma spraying, spray painting) and spray cooling. It has not only various applications on ground but is also necessary for the design of spacecraft, since spray cooling of electronic devices is part of spacecraft technology. In the space industry, traditional multiphase thermal control technologies for space flight (e.g. loop heat pipes, capillary pumped loops, etc.) satisfy the temperature control, start-up and stability requirements, but their heat flux removal capabilities are limited.

Spray impingement on a wall is either intentional and desirable, e.g. coating or cooling or unavoidable, e.g. in internal combustion engines. Spray impact can intensify the spray heating and vaporization. On the other hand, the liquid film produced by spray impact on the wall may produce negative effects such as enhanced soot formation and increased unburned hydrocarbons in internal combustion engines (Bai and Gosman (1995), Matsui and Sugihara (1986)). Many coatings of solid substrates are achieved by means of sprays; for example in the field of spray painting with the goal to achieve a more regular and homogeneous coating (Satas (1984), Chigier (2002)). In general, there is a multitude of applications with a need of applying spray impact more efficiently. However, no reliable model has yet been developed which is able to describe the outcome of spray impact and the corresponding heat transfer, because of the lack of understanding the wall film flow generated by spray impact. Hence, it is of utmost importance to understand the accompanying physical phenomena and to identify the main influencing parameters which will be used in the model formulation. Due to its extreme complexity, the mechanisms of spray cooling are not completely understood. Spray cooling is a technology of increasing interest for electronic cooling and other high heat flux applications, and is characterized by high heat transfer, uniformity of heat removal, small fluid inventory, low drop impact velocity, and no temperature overshoot (Kim (2007)). It is widely used in many industrial applications, including steel rolling industry (Estes and Mudawar (1995)), cooling of power electronics (Tilton et al. (1994b)) and cooling of human tissues in medicine (Torres et al. (1999)). But why is spray cooling so effective? Is not gas sufficient enough to cool down the same surface? Single phase jet impingement heat transfer has received a great deal of attention in the literature due to its ability to dissipate high heat fluxes at low thermal gradients (Incropera and Dewitt (1990)). Jet impingement has been used in many applications ranging from turbine blade cooling to plasma facing components to high density microelectronics applications (Lee et al. (1999)). Gas impinging jets were first studied with respect to turbine blade cooling. However, heat transfer coefficients orders of magnitude higher than gas jets can be obtained using liquid jets (Bonner et al. (2008)). Imagine also touching a hot iron or a cooker with a finger. What is the immediate reaction in order to cool down a hot surface? We place our finger under a jet of running water or under a shower. Indeed, liquid impingement cooling is one of the most effective methods of thermal control of surfaces. The impact of spray comprised of cold drops on a hot rigid wall provides an efficient and uniform cooling of a surface at a low liquid flow rate (Celata et al. (2008)).

One of the main features of this work is the investigation of the effect of gravity on the hydrodynamics and heat transfer associated with spray impact. The gravity levels are subdivided into microgravity (in brief μg), negative hypergravity (in brief -$\acute{v}$g) and positive hypergravity (in brief $+\acute{v}$g). Why is it of interest to conduct research under different gravity conditions? In most cases, the influence of gravity is evident. First, gravity has a considerable effect on the hydrodynamics of a single drop impact onto a film. Impacts with high Reynolds and Weber numbers can create a crown-like uprising sheet which falls down under the action of capillary force and gravity. Experiments in a microgravity environment are associated with the increase of time and length scales while maintaining the underlying physics and enable to take a closer look at the morphology of the near-wall flow. The height of the crown and the duration of the crown propagation should increase in the absence of gravity. Also, variable gravity environments have been found to be a very useful tool for changing of the characteristic film thickness.

Second, our motivation for performing experiments under microgravity conditions is that we can approach the modeling problem differently, by varying only one parameter (gravity). In comparison to this simplification, the reason for performing the same experiments under positive and negative hypergravity conditions represents extreme boundary conditions in order to emphasize the gravitational force and point out its influence. Such experiments may yield fundamental insights that would be unobtainable under any other conditions.

Moreover, there are some applications in which body forces, like gravity, significantly influence the outcome of spray impact. For example, the cooling of electronic equipment at microgravity as well as at positive hypergravity is important in the spacecraft industry for the phases of take-off and landing of spacecrafts.

1.2 Objectives

The focus of this thesis is aimed at experimental investigations of the hydrodynamics of spray impingement onto a rigid wall, spray cooling phenomenon and the influence of gravity in both contexts. Therefore, an experimental setup is designed and constructed for various platforms: parabolic flights, ballistic rocket, centrifuge and ground. The main aim of the experimental work is to develop an empirical model of spray impact onto a rigid wall. Particularly the hydrodynamics of the liquid film created by spray on the wall is investigated and the spray is characterized. The specific objective of microgravity investigations is the influence on the film formation produced by spray impact onto a heated target, and the associated heat transfer. By investigating the influence of gravity on spray cooling, our understanding of the phenomena can be improved and again, it allows modeling the spray cooling process.

The modeling strategy around the spray impact process onto a heated target is shown schematically in Figure 1.1. The key non-solved problems are to characterize the spray, to describe spray impingement and break-up, including the spray-wall interaction phenomenon, and to characterize the liquid film produced by spray impingement onto a wall.

In addition, the impingement of a single drop on a liquid film, as well as the interaction of their crowns after impacting on the wall, have to be understood. Other than the hydrodynamic aspects, the wall temperature field has to be taken into account and heat fluxes are measured for the development of an emprical model for spray cooling.

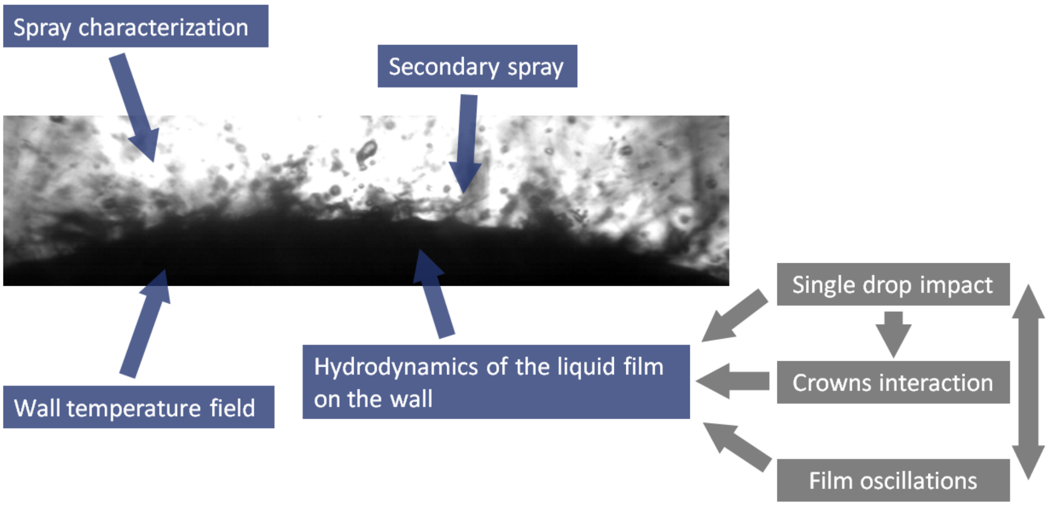

Figure 1.1: Strategy of modeling spray impact and liquid film hydrodynamics.

The task of this work is to create an experimental data base and to develop empirical correlations for the typical main scales of the parameters governing spray impact and spray cooling.

The outline of this dissertation is organized as follows:

- This introductory chapter describes spray impingement phenomena occurring in industrial applications and given the motivation and the relevance of gravity for our studies.

- Fundamental questions of spray impingement experiments as well as spray cooling are addressed in Chapter 2. An overview of the state-of-the-art, reviewing the spray impact modeling problem, the relevance of gravity and the foreseen research strategy is given. To better understand the spray cooling process, its physical working principle is explained in this chapter. Existing models for spray impact and spray cooling are discussed in order to implement the obtained experimental data in the following.

- Chapter 3 describes in detail the experimental apparatus with a full-cone spray and a heated target, consisting of several major supply systems and including measurement as well as control devices. One basic experimental facility including the test cell as the main section is presented. This common structure is implemented in different experimental platforms. Experiments are performed in microgravity during parabolic flight campaigns as well as on board a ballistic sounding rocket and in positive and negative hypergravity conditions in a centrifuge. A basic experimental procedure is described. The spray impact conditions and the wall temperature of the target's surface have been varied. Under ground conditions the investigations are also supported by phase Doppler measurements.

- In order to characterize the spray two main experimental methods are used. In a first step, the implemented spray is characterized with the phase Doppler technique using ground experiments. The primary and secondary drops resulting from the spray-wall interaction are studied. Subsequently, Chapter 4 presents a robust image processing tool that analyses high-speed images to obtain the drop velocity and the drop diameter.
- Chapter 5 focuses on the spray-wall interaction regime. Various modes of spray-wall interaction are observed and classified. The influence of gravity on the hydrodynamics of the liquid film is determined.
- The heat transfer mechanisms involved in the spray-wall interaction are outlined in Chapter 6. It focuses on the effect of gravity on spray cooling and discusses further influencing parameters.
- Recapitulatory and concluding remarks are given in Chapter 7. It is devoted to a couple of open questions and future directions in the field of spray impact and spray cooling.

Chapter 2

Background

2.1 Fundamentals

One of the first to investigate drop impact phenomena systematically was Worthington (1908). Over more than 100 years of research in this field, spray impact phenomena are still far from being fully understood and continue to attract physicists, engineers, mathematicians and even the general public. Spray impact even motivates potential consumers, given the number of commercials based on drop and spray impact scenes aired on television, shown on the web and on postcards (Yarin (2006)).

Figure 2.1: Commercial drop and spray impact scenes with crown formations, splashes, uprising sheets and jets by using different liquids.

The above illustrated drop and spray impact scenarios (see Figure 2.1) are extremely diverse, complicated and surprising with crown formations, splashes, uprising sheets and jets. The drops impacting on a wall can be spherical or due to oscillations ellipsoidal. The impact can be normal (perpendicular) or oblique, in air or in vacuum. The wall can consist of a dry solid surface, a porous material, a free surface of a liquid in a deep pool or a thin liquid film. It can be flat or curved. In addition, the wall can be heated or not heated. The influence of those diverse parameters on the outcome of drop impact is very significant.

Is spray simply a superposition of numerous single drops of various diameters and velocities? Is spray easily reproducible by using multiple drop generators? According to Nasr et al. (2002) spray is a dispersion of drops with sufficient momentum to penetrate the surrounding medium. Processes utilizing drops require enough momentum to transport the drops to where they are utilized or to provide mixing with the gas (Nasr et al. (2002)).

In general, we can distinguish two forms of atomization in a spray: primary atomization which occurs near the nozzle and secondary atomization that is the break-up of drops further downstream, also when impacting on a wall. The main stresses (force per unit area) acting on the liquid during break-up are inertial, viscous and surface tension. Their relative importance is indicated by the Reynolds number *Re* and the Weber number *We* as well as subsequently the Ohnesorge number *Oh*. A rapid and finer atomization is promoted by high values of both, *Re* and *We*. These major non-dimensional parameters governing drop and spray impact are defined in the following Equations 2.1-2.3. For describing the spray and drop impingement phenomena, there are multiple parameters affecting an atomization process such as the properties of the liquid medium and the inflow conditions: the density of the liquid ρ, its surface tension σ, the dynamic viscosity η, the kinematic viscosity ν, the drop velocity u_L and the drop diameter D.

Weber number

$$We = \frac{\rho u^2 D}{\sigma} \tag{2.1}$$

Reynolds number

$$Re = \frac{\rho u D}{\eta} = \frac{uD}{\nu} \quad \text{with} \quad \nu = \frac{\eta}{\rho} \tag{2.2}$$

Ohnesorge number

$$Oh = \frac{\sqrt{We}}{Re} = \frac{\eta}{\sqrt{\rho D \sigma}} \tag{2.3}$$

Capillary number

$$Ca = \frac{We}{Re} \tag{2.4}$$

According to the work of Yarin (2006) and Mundo et al. (1998) another important composite group named K as well as a dimensionless film thickness H, the latter defined with $\bar{h}_{film}$ (see Section 5.3), is given by

$$K = WeOh^{-2/5} = We^{4/5}Re^{2/5} = \left[\frac{\rho^3 D^3 u^5}{\sigma^2 \eta}\right]^{2/5} \quad \text{and} \quad H = \frac{\bar{h}_{film}}{D} \tag{2.5}$$

With the help of two further non-dimensional groups named Bond and Froude number the gravity (g)-related effects are characterized:

$$Bo = \frac{\rho g D^2}{\sigma} \quad \text{and} \quad Fr = \frac{u^2}{gD} = \frac{We}{Bo} \tag{2.6}$$

Spray is not simply a superposition of numerous drops. Spray and its appearance depend on fundamental physics such as inertial forces, surface tension forces and viscous forces. Sprays can be of very chaotic character and its patternation refers to both the shape of the spray boundary as well as the distribution of drops within the boundary.

Usual industrial sprays are polydispersed and are characterized by local velocity and size distribution. Moreover, the local average drop velocity can depend on its size. For example, size and velocity are positively correlated for a decelerating spray or negatively correlated for spray being accelerated by the ambient flow. Different moments of such distributions can be defined. It is sometimes convenient to work not with the entire drop size distributions but only with mean diameters. In the work of Albrecht et al. (2003), Equation 2.7 gives us a general definition of the mean diameters as a moment of the volume density distribution with A and B as integer exponents of the diameter and $n(D)$ as the number based probability density function of the particle diameter D.

$$D_{AB} = \left[\frac{\int\limits_0^\infty n(D) D^A \, DD}{\int\limits_0^\infty n(D) D^B \, DD} \right]^{\frac{1}{A-B}} \tag{2.7}$$

Next to the arithmetic mean diameter D_{10}, one of the most frequently used by investigators is the Sauter mean diameter (SMD), D_{32}, which is a diameter of a drop having the same volume-to-surface ratio as the entire spray (Lefebvre (1989)).

The outcome of drop impact depends on the impact velocity, its direction relative to the surface, drop size, the properties of the liquid, the surface or interfacial tension, the roughness and wettability of the solid surface, the nonisothermal effects and air entrapment. As a result, phenomena such as frontal ejecta and crater formation in solid-solid impacts are reminescent of those characteristic of liquid drop impact (i. e. splashing and crown formation), which led Worthington to call the former “permanent splashes” (Yarin (2006)).

A spray impacting onto a rigid wall creates on its surface a thin, moving, fluctuating liquid layer. A large variety of phenomena is associated with the flow in this liquid layer initiated by single drop impingements and their interactions. The source of the fluctuations of this film is the momentum of the impacting drops. One of the subjects of the spray impact research is the determination of the velocity fluctuation magnitude in the liquid film and parallel to the wall. In some cases these fluctuations lead to the break-up of the film and to the creation of secondary drops. The flows of these secondary drops including aspects of their total volume flux, size and velocity distribution are one of the important subjects of spray impact studies.

Figure 2.2 shows a detailed classification of phenomena occurring when spray impacts onto a wall. Different phenomena can play a dominant role for various spray impact regimes. Some lead to the creation of secondary drops, some to film fluctuations, others to corona splashes and they are all united by a common source: a single drop impact.

At small Weber numbers there is a formation of a liquid finger in the impact axis leading to smaller drops (a). The contribution of the surface forces at the boundary to the gas phase is comparable to the one of the inertial forces. Surface forces on the wall are relatively small. At higher wettability on the wall, the drop can be attached to the wall (b) and an oscillating liquid film is formed there. Drops that are impacting with a higher velocity on the liquid film create a crater which features according to the impact energy a different crown-like corona (c).

When the impact scenario is asymmetric, the kinetic energy is distributed radially uneven. A smooth transition can be then observed (d) and the corona is sidewise deformed because of the translation movement compared to the fluid film on the wall. At very high impact velocities, a so called "direct spray", is developed at the leading edge of the impacting drop (e). It detaches from the decelareted contact line (from the geometric point of view). The corona aligned in the region is instable and collapses because of rim and film instabilities, capillary forces and above all due to irregularities at the inertial forces of corona sections (Roisman et al. (2007)). Thereby, the rim immediately breaks up into several new drops (f). At a greater film thickness the fluid can diverge in depth. As the crater fronts collide again when closing not only fluid fingers and drop formation can occur but also embedment of gas bubbles (g). Another possible scenario is the collision of two neighboring primary drops that can influence each other tremendously and lead to splash without forming a corona (h). This interaction can also lead, after a longer time scale, to a film flow and film fluctuations that are very difficult to simulate (i). Also, as shown in (j), a drop impact onto a liquid film covering a hydrophobic surface, can initiate dewetting in the impacting region. If it the case that due to stability loss the liquid film becomes instable on a hydrophobic surface, large moving drops can be formed (k). At higher, more violent spray densities

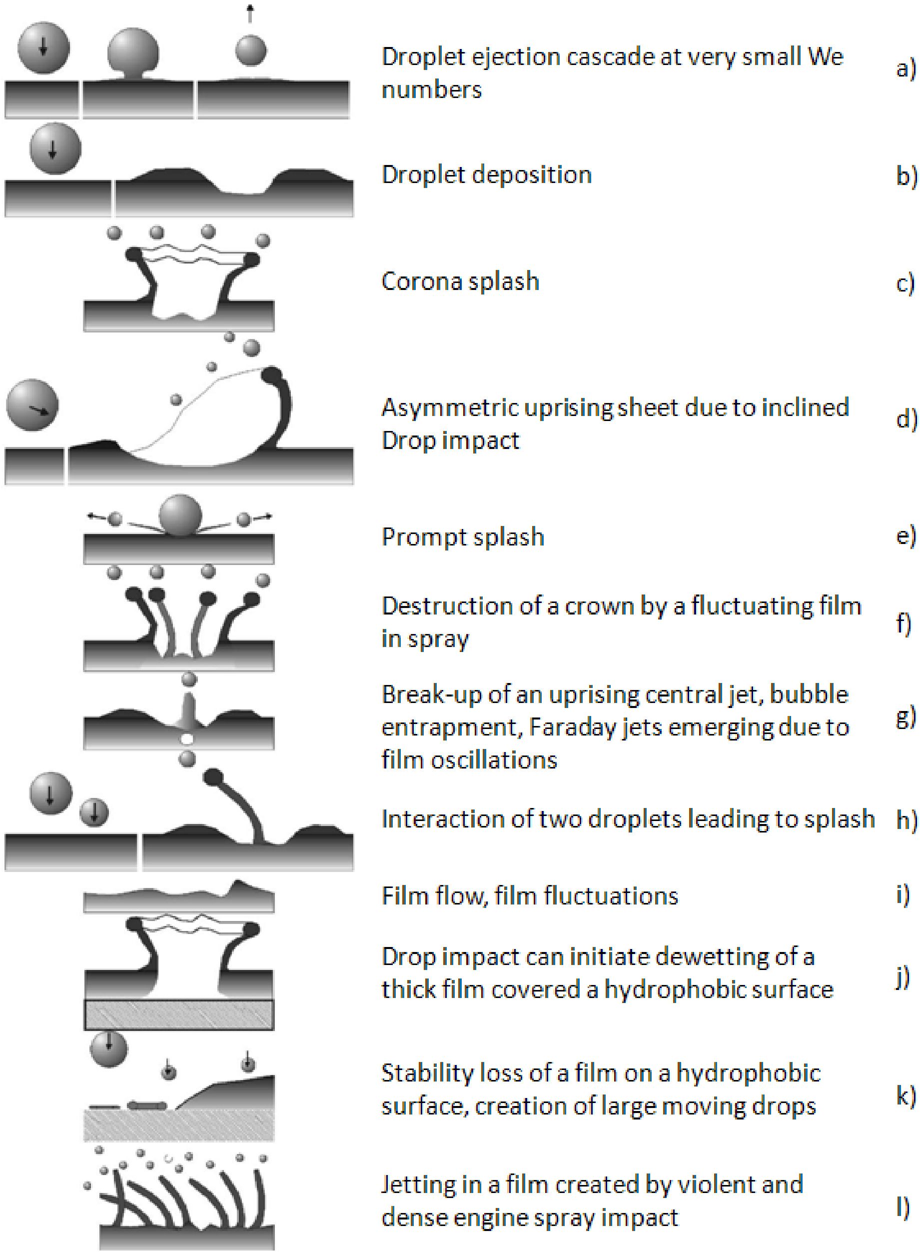

Figure 2.2: Various phenomena of spray-wall interaction (Roisman et al. (2006)).

like engine sprays, a layer can be created due to a multitude of jets interacting again with impacting drops that may not reach the film (l).

All these phenomena are not trivial. Their mechanisms are not easily recognized, especially if they appear in our experimental investigations in combination. At a spray-wall interaction we do not only deal with prompt splash, corona splash, central jet splash but also with other modes of spray impact break-up. Crowns break up not only due to the rim bending instability but also due to sheet instability in the azimuthal direction originating at the liquid film. As shown in Figure 2.3, this instability leads to the complete break-up of a crown. A rim is formed at the upper free sheet region. Due to bending disturbances and break-ups, the rim becomes unstable and holes appear in this upper sheet region. In addition, several finger-like jets are created that lead to fluctuations, stretching and finally break up into numerous smaller, rotating, nonspherical drops (Roisman et al. (2006)).

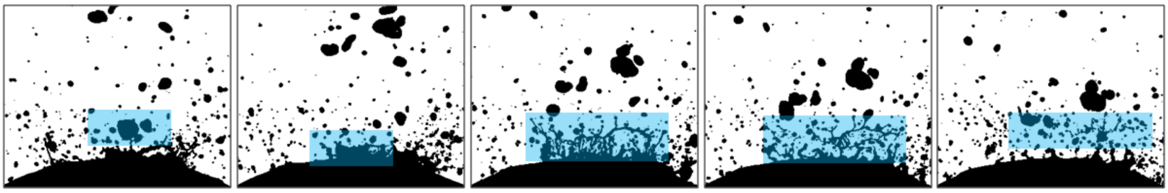

Figure 2.3: Time sequence of a spray impacting onto a fluctuating liquid film leading to various spray-wall interaction phenomena (blue box), e.g. crowns break-up, corona splashes, finger-like jets and drop creation.

The following scheme outlines the heat transfer mechanisms associated with the spray impact. According to the sketch in Figure 2.4 the total heat flow $\dot{Q}_w$ at the cooling wall surface is defined by the heat fluxes corresponding to the heat convection in the fluctuating wall film $\dot{Q}_f$, the convective heat flow provided by the primary droplets, the impacting spray $\dot{Q}_{ps}$, the associated secondary spray $\dot{Q}_{ss}$, free convection in the ambient gas $\dot{Q}_{fc}$, heat flow $\dot{Q}_e$ corresponding to the evaporation from the free film surface and the contact lines $\dot{Q}_{cl}$.

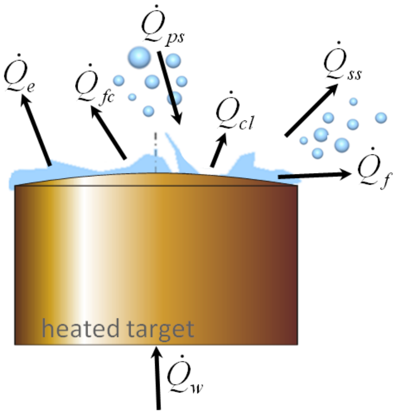

Figure 2.4: Mechanisms involved in heat transfer during spray impact onto a heated target.

The to be developed model should include the impact process, the wall film hydrodynamics as well as the heat transfer of a single drop (Mustafic et al. (2004)). According to Gambaryan-Roisman et al. (2007) the single drop impact contributes to the global mass, momentum and energy balance inside the film and modify the local velocity field in the film as well as the local film dynamics.

If we follow the circuit of only one specific drop during spray cooling, its function can be described as multitasking: a cold oscillating drop impacts onto a heated target, creates splashes, uprising sheets and jets, a corona and affects the liquid film thickness. Locally, the velocity is increased at this moment of impact and consequently the heat transfer coefficient is greater than before. During drop-wall interaction, heated fluid from the liquid film is replaced by cooled one. In a next step, the resulting secondary drops conduct the embedded heat and might collide with new cold impacting drops.

2.2 State-of-the-art

2.2.1 Spray impact

Even though the processes involved in spray impingement are very complex, the studies of Roisman et al. (2006) and Roisman et al. (2007) have distinguished and classified some frequently observable splash scenarios (see Figure 2.2). Due to the complexity of the phenomena the modeling of spray impingement mainly relies on empirical or semi-empirical correlations. In Cossali et al. (2005), a comprehensive review of such models can be found by approaching spray impingement as a superposition of single drop impacts onto a wetted or even dry wall. Although simplified models of spray impingement have been applied in this work, such modeling is usually applicable only for a restricted range of parameters as used in the corresponding experiments (Tropea and Roisman (2000)). Hence, a generalization of such models may not be considered as a universal prediction tool Roisman et al. (2006), Roisman et al. (2007)). Stated below are modeling approaches and further models used in industry as sub-models for numerical codes simulating the processes involving spray transport and impingement onto a wall.

There are three main approaches to the modeling of spray impingement onto a solid substrate. The first approach describes the process as a simple superposition of single drop impingement events (see Naber and Reitz (1988), Stanton and Rutland (1996), Stanton and Rutland (1998), Bai and Gosman (1995), Bai et al. (2002), Han et al. (2000), Mundo (1996), Park and Watkins (1996), Samenfink (1997), Senda et al. (1997) and Senda et al. (1994)). Models with varying degrees of complexity are thus formulated on the basis of available data for the single drop impact, in some cases with a complete neglect of the actual fluid mechanics or with a disregard for some influencing parameters. The examples of this approach can be found in the models for fuel spray impingement (see Bai and Gosman (1995), Stanton and Rutland (1996), Han et al. (2000), Bai et al. (2002)) and for water sprays (Samenfink (1997), Mundo et al. (1998), Marengo (1999)). A similar approach is used in the model for thermal plasma spraying (Lee and Bergman (2001)), accounting for the solidification of the drops. Such models are based on experimental studies (Harlow and Shannon (1967), Cossali et al. (1997), Rioboo et al. (2001)) or theoretical studies (Yarin and Weiss (1995)) of the single impact of a liquid drop onto a steady uniform liquid film, or into a deep pool (Oguz and Prosperetti (1990)).

The second approach is frequently applied in the description of spray painting (Eres and Schwartz (2001)). It neglects completely the inertial effects associated with spray impingement. Negative flux of secondary drops and the momentum of the oscillations of the liquid in the film on the wall are also neglected. The spray is considered only as a source of the liquid volume flux. Next, the motion of the deposited liquid film is described using the governing equations of hydrodynamics of falling films.

The third approach is based on direct numerical simulations of the spray impact. Böhm et al. (1999) have used a commercially available numerical code, based on the volume-of-fluid method, to simulate not only a single drop impingement onto a dry wall but also a multi-drop impact. The normal impingement of up to 22 uniformly distributed spatially identical drops was investigated. This multi-drop impact leads to the creation of an oscillating film. Note however that polydisperse spray impact is characterized by different length and time scales. The characteristic length scale of the film fluctuations may be much larger than the drop diameter and the characteristic time of such fluctuations is much larger than the typical time of drop impingement. This means that in order to describe the spray impact numerically, a relatively large domain size is required with a very fine mesh. Next, the time step must be small enough to describe each drop impact event. Moreover, a relatively large time duration must be simulated, such that a large number of drops will impact, in order to represent the real statistics of the spray. This problem is too complex and expensive even for modern supercomputers.

The above or similar models are used in industry as sub-models for numerical codes simulating the processes involving spray transport and impact onto a wall. It should be emphasized that such models are not universal for the description of spray impact. However, there does not yet exist a better model due to the complexity of the phenomenon. Again, there is a lack of data for the oscillations of the liquid film created by spray impact and a lack of theoretical solutions.

2.2.2 Spray cooling

Further progress in the research field of spray cooling can be only achieved when the hydrodynamics of spray impingement can be better clarified and captured in the models. In order to remove heat from hot surfaces, spray impingement is a very effective means. Heat transfer rates much higher than in pool boiling can be attained with sprays since the vapor can be removed from the surface more easily. The so called spray cooling is applied in the field of metal production (Mudawar and Deiters (1994), Hall and Mudawar (1995)), for the cooling of electronic modules (Tilton et al. (1992), Tilton et al. (1994a), Tilton et al. (1994b), Mudawar (2000)), cooling of diode laser arrays (Huddle et al. (2000)), cryogenic cooling of human tissues (Torres et al. (1999)) in medicine. With spray cooling it is possible to dissipate over 100 W/cm^2 using dielectric coolants (Mudawar (2000)). Sprays provide a high contact surface between the heated surface and the cooler and an even distribution of the cooling liquid over the relatively large hot surfaces. The temperature range of applicability of the spray cooling technique lies between the cryogenic temperatures (80 K) (Tilton et al. (1994b), Sehmbey et al. (1995), Chow et al. (1996)) to about 1300 K (Bolle and Moureau (1982)). An important demand for spray cooling of electronic equipment is the uniform heat removal from the surface and avoidance of hot spots. A comprehensive review of spray cooling at various regimes can be found in the work of Kim (2007).

Depending on the spray characteristics as well as on the wettability properties, on the surface structure and the wall temperature various reactions of the drops when impacting on the wall have been already observed. The impingement of drops onto a heated wall is experimentally investigated in Chandra and Avedisian (1991), Bernardin et al. (1997a) and Bernardin et al. (1997b). In particular, the influences of the wall temperature, the Weber number and the surface roughness on the impingement result are studied. There are some tendencies that can be stated: (i) reduction of the maximal liquid film diameter resulting from the propagation of a single drop on the surface with increasing wall temperature, (ii) enhancement of the endurance of a drop until the evaporation with diminishing wall temperature, (iii) lowering of the needed drop propagation time on the wall with increasing Weber number and (iv) descent of drop endurances with a growing surface roughness.

In spite of the multitude of flow types appearing due to spray impact on a heated wall and a liquid film, the heat transfer of a specific spray (including parameters as nozzle design, fluid flow, gas flow, nozzle-to-target-distance) can be presented with the help of a curve progression q_w, T_w-diagram (see Figure 2.5) considering a typical boiling curve as behaving in a classical pool boiling process (Carey (1992)). For each heat flux, the average heater temperature T_w is noted and serves as the abscissa for the corresponding curve point while the heat supply (i. e. heat flux q_w) serves for the ordinate. The slope of the boiling curve represents the derivative of the heat flux relatively to temperature.

When the heat flux is small, only a fluid convection can be observed whereas at a larger heat flux one can notice the regime of nucleate boiling commonly considered in a sauce pan. It features separate vapor bubbles that nucleate, form and grow at the heater. In this regime the heat transfer rate is very large due to both, the phase change (latent heat of evaporation) and the fact that the superheated liquid is carried away from the heating surface by the departing vapor bubbles. Therefore the boiling curve slope is larger than for the convection regime. The most important parameter in this curve including the absolute values of heat transfer through the wall, the curve gradient at different flow types as well as the critical heat transfer coefficient are defined by spray properties and surface qualities. In some cases, e.g. when the liquid film is very thin, the area of bulk boiling disappears in the curve. In addition, Figure 2.5 points out the singularities of the boiling curve such as the critical heat flux (CHF) and the minimum heat flux (Leidenfrost temperature).

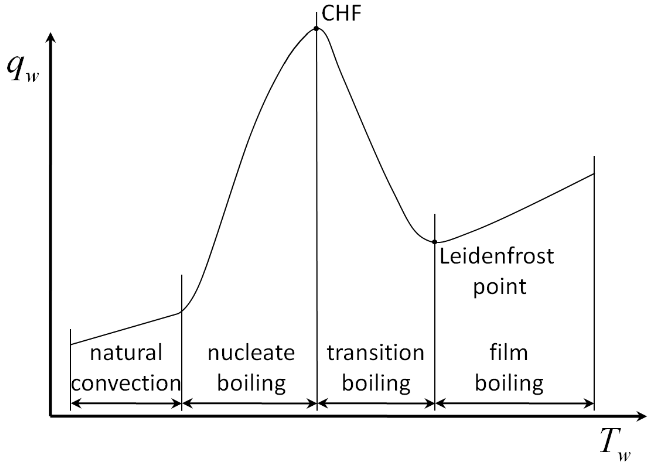

Figure 2.5: Nukiyama (Pool boiling) curve with four regions: natural convection, nucleate boiling, transition boiling, film boiling.

Numerous studies have been performed that focus on the influence of spray characteristics on heat transfer. The mechanisms by which heat is removed during spray cooling are poorly understood, however, due to its dependence on many parameters that are not easily varied independently, and predictive capabilities are quite limited (Kim (2007)).

In Table 2.1 some recent and most significant results in the field of spray cooling are reviewed from various authors (see given reference). Next to some short remarks, the herein main parameters are the liquid, the size of the drop D_{drop}, its velocity u_{drop}, the surface temperature T_w and the maximal heat flux q_w. This table demonstrates that the properties of spray cooling depend on a great number of experimental boundary conditions. This is attributed to the enormous degree of complexity of the herein investigated phenomena. Accordingly, no consensus can be obtained from the authors regarding the influence of several parameters such as volumetric flow rate of the spray, average drop diameter and velocity on the heat transfer. Apparently, the role of various parameters depends on the behavior of the liquid on the wall, the existence or the nonexistence of a continuous liquid film on the surface and so on.

Table 2.1: Existing studies on spray cooling.

ref.	liquid	D_{drop} (μm)	u_{drop} (m/s)	T_w(°C)	q_{max}(W/cm^2)	remarks
Toda, 1972	water	90-300	42-76	107-202	350	convection, evaporation
Mudawar and Valentine, 1989	water	434-2005	10.6-26.5	20-90	50	convection
Mudawar and Deiters, 1994	water	146-344	12.3-21.7	$<$400	500	beneath film boiling
Estes and Mudawar, 1995	FC-72	110-225		58-95	137	CHF rises with mass flow rate
Yoshida et al., 2001	water	60-386	5.1-10.8	100-350	300	no continuous film
Horacek et al., 2005	FC-72	50(SMD)	21	50-100	66	film distribution invest.
Li et al., 2008	water			100-126	160	copper nanorods
Lu et al., 2008	water	3200	0.6	110-190	6	evaporation+nucleation
Visaria and Mudawar, 2008	PF-5052	111-249		50-105	200	inclined spray: tilting decr. CHF
Silk et al., 2008	water				1000	spray cooling, NASA flights
Wendelstorf et al., 2008	water	300-400	13-15	199.85	75	α dep. on impact density+temp.
Strotos et al., 2008b	water	2070	0-1	60-100	300	VOF-calc. and experiment
Srikar et al., 2009	water	3000	0-1.98	60-140	15	nanomats
Panão and Moreira, 2009a						intermitt. spray cool.

Some recent work are devoted to the analysis of the most important mechanism of spray cooling. Horacek et al. (2005) investigated spray cooling on a 7.0 mm x 7.0 mm surface heated with 96 microscopic heating devices. This technique made it possible to keep the temperature at the total heated surface constant and to measure the distribution of the heat flux at the heated surface. A special, very accurate optical measurement technique called “total reflectance” was used in order to visualize wetted and dry spot regions on the spray cooled surface. A digital image processing technique was implemented to measure the total wetted surface and the contact line density. The results consider that the contribution of evaporation to the total heat transport correlate directly to the 3-phase-contact line density.

2.2.3 Spray cooling enhancement

Some authors assume that the heat transport can be improved by smart substrates and artificially increasing the contact line density. One method is to apply a rough (Pais et al. (1992)) or a fine structured surface on spray cooling investigated by Silk et al. (2004) with various structures: longitudinal ribs, cubic forms and pyramids. All structure elements have a height of 1 mm and a width of 1 mm. The spray used in this work is generated by means of a 2 x 2 matrix of nozzles. The implementation of a structured surface leads to an improvement in heat transport. The greatest performance is achieved with longitudinal ribs. The critical heat flux (CHF) is increased by 55 % in the case of the surface with longitudinal ribs compared to the flat surface. Most enhanced surface spray cooling studies have been performed using either extended or embedded surface structures. In the study of Silk and Bracken (2010), the effect of POCO HTC foam on spray cooling heat flux is investigated. The copper blocks used in the heat flux performance study have a cross-sectional area of 2 cm^2, PF-5060 is used as the working fluid. Results show that the highest heat flux attained was 133 W/cm^2 using the graphite POCO HTC foam (lightweight graphite materials) with a nozzle-to-foam distance of 17 mm. Further research in this field has been performed by Li et al. (2008) with copper nanorods and by Srikar et al. (2009) with nanomats. The authors show that there is no connection between the achieved heat flux and the heat transfer area.

Theoretical and experimental study of the effects of spray inclination on two-phase spray cooling and CHF is studied in the work of Visaria and Mudawar (2008). Experiments were conducted with PF-5052 liquid sprays impacting on a 1.0 cm x 1.0 cm heated test surface at different inclination angles, flow rates, and subcoolings. The inclination angle had no noticeable effect on the single-phase or two-phase regions of the boiling curve. The maximal CHF was always achieved with the spray impinging normal to the test surface.

A transparent heated surface in the studies of Yoshida et al. (2001) allows a visual observation of the fluid distribution. As a result of the spray impacting onto the wall discrete fluid films are formed whose thickness depends on the heater orientation relative to the gravitational field. The influence of gravity on spray cooling and on the film topology is also investigated by Sone et al. (1996) and Yoshida et al. (2001). Due to the large momentum of the drops within the spray, spray cooling is not expected to be affected by heater orientation relative to the gravity vector, or by low gravity conditions. The authors report about the results from spray cooling experiments with water and the fluid FC-72 (perfluorohexane C_4F_{16}) on ground as well as during parabolic flights in low-g (0.01g) and high-g (1.8g) environments. In their experiment copper blocks (50 mm diameter of heater surface) are heated to above the Leidenfrost temperature defined as the temperature where the total evaporation time of a drop reaches a maximum and the heat flux assumes a local minimum. Then, they are cooled down with a spray to generate data from film boiling through the nucleate boiling regime. The influence of the surface orientation of the heated surface compared to the axis of the spray on heat transfer is discussed in detail for ground tests. No effect of gravity is observed in the nucleate boiling regime and CHF. In the transition boiling regime and at minimum heat flux in the low-g environment and downward facing heaters (ground conditions) than for the upward facing heaters (ground conditions) significantly lower heat transfer is observed. This occurs due to the lack of secondary drops impacting on the target that are rebounded from the surface. Hence, low-g environments can dramatically affect spray cooling at higher flow rates if the surface becomes flooded due to inefficient removal of excess liquid. Surface tension flow around the spray nozzle leading to improper atomization is observed in the work of Baysinger et al. (2004).

The work of Silk et al. (2008) gives a technology overview of spray cooling heat transfer and assessment of future challenges for microgravity application. Advanced on-board flight systems for future NASA space exploration programs consist of components such as laser-diode arrays (LDA's) and multi-chip modules (MCM's). Thermal management of these systems require high heat flux cooling capability, tight temperature control ($\approx \pm 2$ °C), reliable start-up (on demand) and long term stability. Spray cooling can provide high heat fluxes in excess of 100 W/cm^2 using fluorinerts and over 1000 W/cm^2 with water while allowing tight temperature control at low coolant fluid flow rates. Spray cooling has been flight proven in an open loop configuration through the Space shuttle's flash evaporator system (FES). This paper provides a discussion of the current status of spray cooling technology as well as NASA's goals, current direction and challenges associated with the implementation and practice of this technology in the microgravity environment.

In the research work of Panão and Moreira (2009b), intermittent spray cooling is proposed as a new technological concept to remove heat fluxes with good performance and introduce the potential use of advanced control techniques in the development of thermal management systems. The objective is to provide further insight into the physics involved in the heat transfer process triggered by the impact of an intermittent spray, and further investigate the effects of injection system parameters, such as the frequency of injection, pulse duration, initial wall temperature, pressure of injection and impingement distance, on the intermittent cooling system's performance (see also Panão and Moreira (2009a)).

2.2.4 Modeling approach

Due to the extreme complexity of heat transport mechanisms during spray cooling there exists only a small part of literature dedicated to theoretical investigations. In the work of Wendelstorf et al. (2008), the heat transfer for spray cooling of clean surfaces using full-cone nozzles and surface temperatures between 200 and 1100 °C were investigated. From the experimental data, an analytic correlation for the dependence of the heat transfer coefficient (α) as an analytic function of the water impact density and the temperature is provided.

Computational fluid dynamics numerical simulations for 2.0 mm water droplets impinging normal onto a flat heated surface under atmospheric conditions are presented and validated against experimental data by Strotos et al. (2008a). The coupled problem of liquid and air flow, heat transfer with the solid wall together with the liquid vaporization process from the droplet's free surface is predicted using a VOF(volume of fluid)-based methodology accounting for phase-change. A kinetic theory model is used to evaluate the importance of thermal non-equilibrium conditions at the liquid-gas interface and which have been found to be negligible for the test cases investigated. The numerical results are compared against experimental data, showing satisfactory agreement. Model predictions for the droplet shape, temperature, flow distribution and vaporized liquid distribution reveal the detailed flow mechanisms that cannot be easily obtained from the experimental observations. In addition, further numerical results are compared against experiments for the droplet volume regression, life time and droplet shape change by Strotos et al. (2008b) and they show a good agreement.

A dynamic approach by Panão and Moreira (2009a) presupposes the identification of systematic periods characterizing the spray dynamic behavior and, once identified, the development of a heat transfer correlation for each period. The analysis ends with a comparison between the dynamic heat transfer correlation with a correlation obtained using the conventional approach and a significant improvement in heat transfer predictions is achieved if the spray dynamic nature is considered.

Up to now, nobody attempted either to investigate the stability properties of liquid films produced by spray impact onto a heated target or to predict the dynamic properties of the liquid film outside of the stable region. The peculiarities of mass, momentum and energy exchange between the impacting drops and the liquid film are not considered sufficiently in the present models (Kim (2007)) and pose a challenge.

Chapter 3

Experimental setup and procedure

Spray impact onto a heated target has been investigated under terrestrial conditions and compared with observations gained under microgravity, negative hypergravity and positive hypergravity conditions. This chapter is intended to provide a comprehensive description of the experimental setup (see Kyriopoulos et al. (2006)) with diverse supply systems and its structural modifications corresponding to the investigational platforms: parabolic flights, ballistic rocket, centrifuge and laboratories on ground. All parts of the various experimental setups are described in this chapter.

3.1 Main systems and test cell

A scheme of the experimental setup for the investigation of the spray impingement on a heated target and spray cooling is shown schematically in Figure 3.1. It shows the five major subsystems of the apparatus: a liquid supply system (1), a gas supply system (2), a test cell (3), a thermal system (4), an optical visualization system (5), an extraction system (6) as well as an electronic measurement and control and data acquisition system (not shown in this figure). The phase Doppler instrument used in the laboratory to characterize the spray is also not shown in Figure 3.1.

Each system will be explained in a more detailed way in the next sections. As shown in the scheme, the liquid is stored in a reservoir and is provided to the atomizer. Alongside to the liquid supply system, a gas supply system is responsible for the ventilation of the test cell.

The test cell is the heart of each experimental setup. Since the spray impact phenomenon occurs inside, it is a fundamental element for our investigations. Therein, the spray impacts onto a convex heated target positioned at a distance of 70 mm from

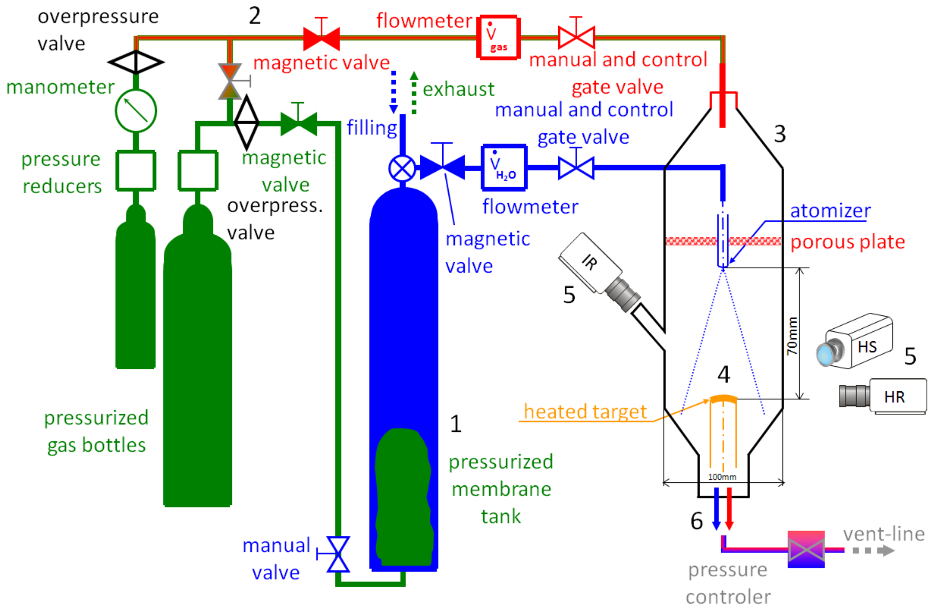

Figure 3.1: Schematic of the experimental setup consisting of five major subsystems: liquid supply (1, blue), gas supply (2, red), test cell (3), thermal system (4, yellow), optical visualization (5) and extraction system (6).

the atomizer. The water and gas supply system are brought together in this cylindrical casing including next to the atomizer a mounted heated target. Hence, the test cell functions as a container. It serves as protection against outside influences and on the other side prevents the electronics necessary for the thermal system and the surrounding camera system to get wet. Next to the thermal system and the optical visualization, an extraction system allows the water and gas to discharge.

The prototype test cell including all elements that were tested in the first two parabolic flight campaigns has been built in the workshops of the Chairs of Fluid Mechanics and Aerodynamics as well as Technical Thermodynamics (Technische Universität Darmstadt). On the third parabolic flight campaign an already modified experimental cell was implemented. For the subsequent investigations on board the TEXUS 45 sounding rocket campaign and in the centrifuge an accomplished test cell made out of aluminum (illustrated schematically in Figure 3.2) as well as an improved heated target (see Figure 3.7) have been designed and constructed by EADS Astrium on the basis of already existing mechanical drawings. The test cell's inner diameter is down to only 10 cm and its height amounts about 19 cm. In total, the designed size is compact due to the space availability defined by the rocket's inner bodyshell.

The windows of the test cell are coated with TEGOTOP®105, a product of Evonik Degussa GmbH, in order to attain a superhydrophobicity effect aimed at preventing the

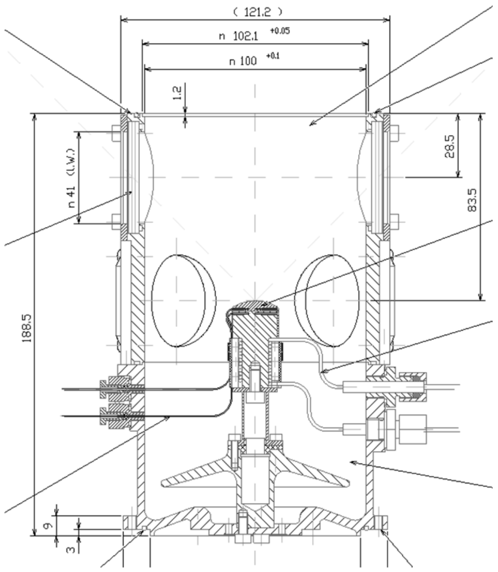

Figure 3.2: Mechanical drawing of the TEXUS-module including the heated target by EADS Astrium, its heating wire and thermocouple entries.

deposition of the drops on the windows. The optical transparency allows observation of the spray impact leading to the formation of the liquid wall-film and generation of the secondary spray. Three cameras can be integrated in the experimental rig: a high-speed video system, a high-resolution camera system and a high-speed infrared camera (see Chapter 3.5).

The main procedure on the day of experiments is to first turn on the water and gas supply system so that the spray and the gas co-flow are provided inside the chamber. Only if those requirements are complied the heating system can be activated. As another general rule, the measurements are only carried out or rather taken into account when a stationary situation (constant temperature) is achieved. Simultaneously, the cameras are operated to record spray images.

3.2 Water supply and atomization system

The liquid is stored in a reservoir in form of a pressurized membrane tank filled partly with liquid and partly with gas. The compressibility of the here utilized nitrogen gas is used for liquid storage so that the membrane tank can provide the distilled water spray.

The distilled water arising from the pressurized membrane tank is supplied to the nozzle generating spray that is installed inside the test cell.

There are different types of spray nozzles for different demands. Our water spray is generated by a full-cone pressure swirl atomizer with a cone angle of 30° (series 3001.4) and was developed by the company Spraying Systems. As general spray characteristics a full-cone nozzle provides a uniform, round and full spray pattern as shown in Figure 3.3. Very often, there is a clear peak in mass flux in the centre. Moreover, as more liquid flows into the center of the pattern, the spray pattern distribution typically deteriorates.

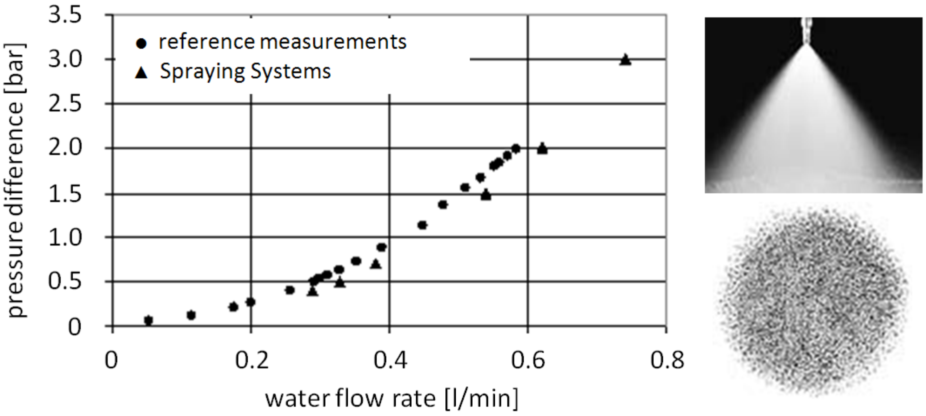

Figure 3.3: Verification of the characteristic curve of the spray nozzle provided by Spraying Systems and used in all experiments.

In order to be sure that our spray is reproducible, identical nozzles of the same type were investigated in advance at various water flow rates, starting from 0.05 l/min up to 0.6 l/min and then compared with the solely given results from Spraying Systems. The results for the pressure difference at the atomizer correlate well and are shown in Figure 3.3.

The liquid medium used throughout our experiment is distilled water. The impacting drop diameters and drop velocities for water flow rates have an order of $d_p \approx$ 100-300 μm and $u_p \approx$ 2-15 m/s respectively.

3.3 Ventilation system

The gas supply system provides not only nitrogen for the pressurized membrane tank but also a gas co-flow to the system allowing to ventilate the test cell. Inside the test cell, the air streams first through a 5 mm thick porous plate (METAPOR®CE 100 white) as shown in Figure 3.4 in order to uniform the flow. Then, the resulting air helps preventing the deposition of drops on the windows for a better optical access.

The deposited gas is finally exhausted together with the water from the test chamber using an extraction system.

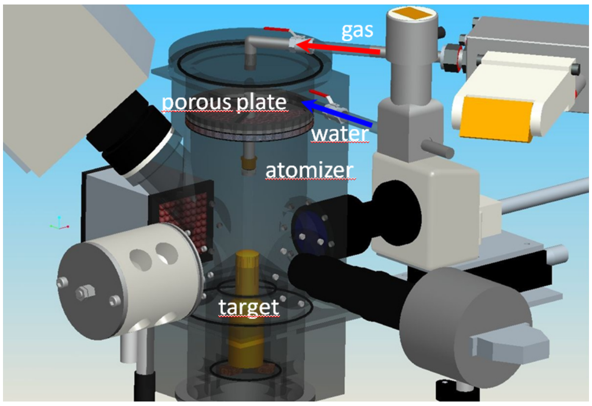

Figure 3.4: Test cell supply systems with porous plate enabling spray impact onto a target.

3.4 Thermal system

The target (see Figures 3.5 and 3.7) is made out of copper (grade Cu-ETP) and its shape is a truncated sphere ($D_{target} = 40$ mm) with the diameter of a projected area 20 mm. The convex spherical shape of the surface has been chosen to allow a precise observation of the profile of the film generated by spray impingement at the target's generatrix.

The thermal system includes the heated target, heating power supply and a set of twelve most common general purpose thermocouples of Type K (NiCr-Ni) to measure the temperature.

As shown in Figure 3.5 ten thermocouples are installed in the experimental cell: five (T_{1U} - T_{5U}) to measure the temperature in the upper part of the target about 3.7 mm below the target's surface (see also Figure 3.7, one at the axis and four to estimate the temperature gradients in the radial direction), five more (T_{1L} - T_{5L}) are installed in the lower part of the target at a depth 2 mm below the upper thermocouple group; one for the air temperature inside the chamber; one for the liquid temperature before the atomizer.

The temperature of the heated target is controlled by the upper thermocouple positioned at the apex to reach a setpoint temperature (T_S) that was manually managed and during TEXUS 45 operated through a telecommand. The temperature field inside the target is measured again with Type K thermocouples as previously described. The heater is surrounded by a Teflon shell for a better insulation against loss of heat.

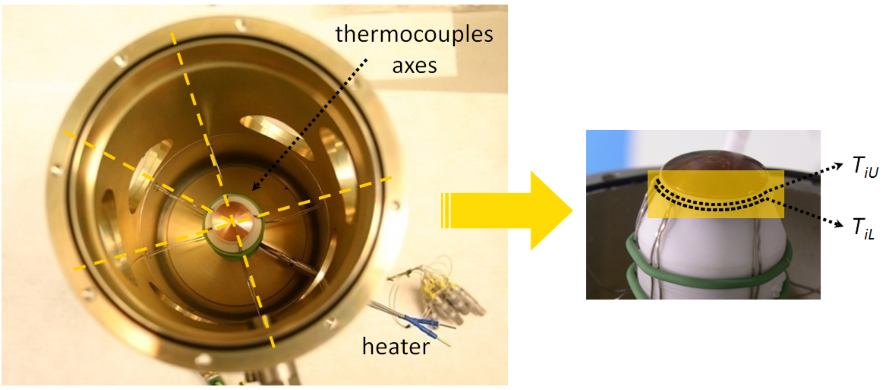

Figure 3.5: Arrangement of ten thermocouples inside the test cell along different axes (left, top view) and mounted thermocouple pairs in yellow region (five in the upper part T_{iU} and five in the lower part T_{iL}) with a depth of 2 mm below each other (right, side view, yellow region.

For the first two parabolic flight campaigns the prototype target has been heated with three heating cartridges (hotrod®type HHP Ø 8 x 50, max. 125 W, 230 V) as shown in Figure 3.6.

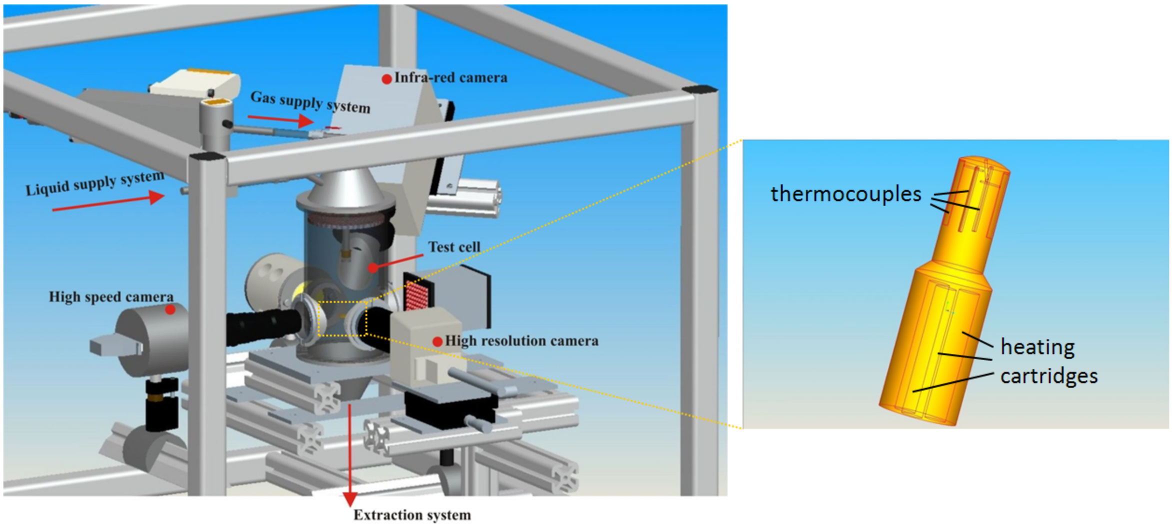

Figure 3.6: Prototype test cell with surrounding devices and heated target (3D-CAD model).

In comparison, the target from EADS is heated with a heating wire (THERMOCOAX, type 1Ncl15/65 cm/2xCM15/T-1 mm^2/0,65 m) and is directly attached to it as shown in Figure 3.7. This target consists of two parts: the upper part in the shape of a spherical cap and a lower part consisting of two cylinders of different diameters (see Figure 3.7). These two parts are separated from each other by a layer providing a homogeneous thermal resistance. With the help of the temperature reduction at the adhesive sealing the transported heat quantity can be ascertained. From experience, the sealing with the all-purpose glue is only stable up to 150 °C. In case of breakdown of the cooling spray, the surrounding Teflon insulation can be destroyed due to residual heat of the heating wire and also due to the inactivity of the thermal conduction. Figure 3.7 shows the target with the sealing layer as well as some entrances for the thermocouples. The thermal resistance layer is situated between the two thermocouple groups mentioned before.

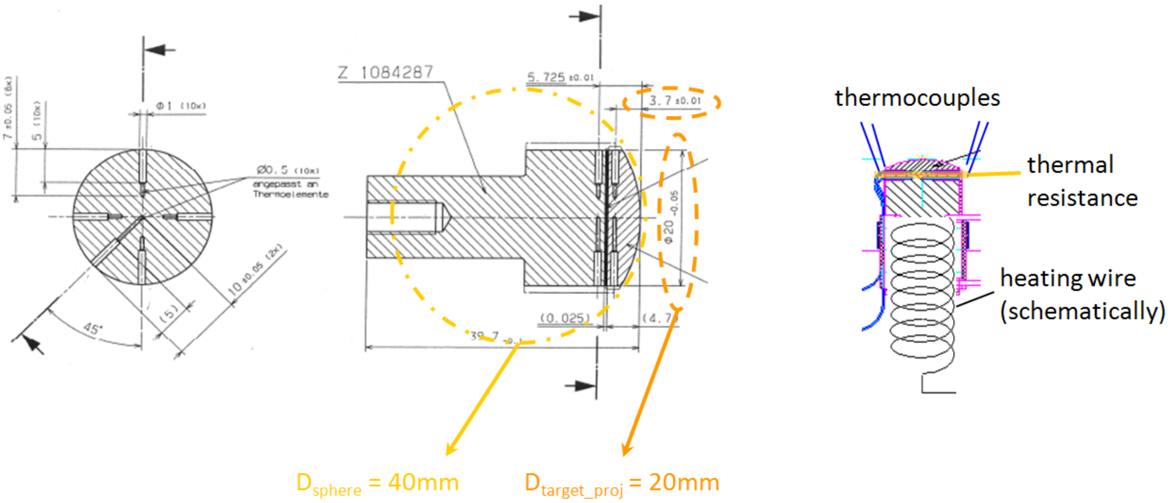

Figure 3.7: Mechanical drawing of the target showing all thermocouple entries: four radially positioned and one at the axis as well as the same quantity placed 2 mm below the upper thermocouple group (left drawing on a scale of 1:1). Schematically illustrated heating wire around the target (in this case in test cell position, see Figure 3.2), thermal resistance layer (highlighted in yellow) and four thermocouple entries from the side view (right one at 1:2).

3.5 Optical system

The experimental setups have been designed for each experimental platform in such a way that all cameras can be implemented. But not all of them were used simultaneously as illustrated in Table 3.1.

As shown in Figure 3.8 the film flow is observed at various time instants using the high-speed video system (HS). The drop size distribution is analyzed with the high-resolution camera system (HR). The film pattern is characterized with the help of the high-speed infrared camera (IR).

The images of the spray-wall interaction during parabolic flight experiments have been captured using a high-speed video system consisting of a stroboscope light source

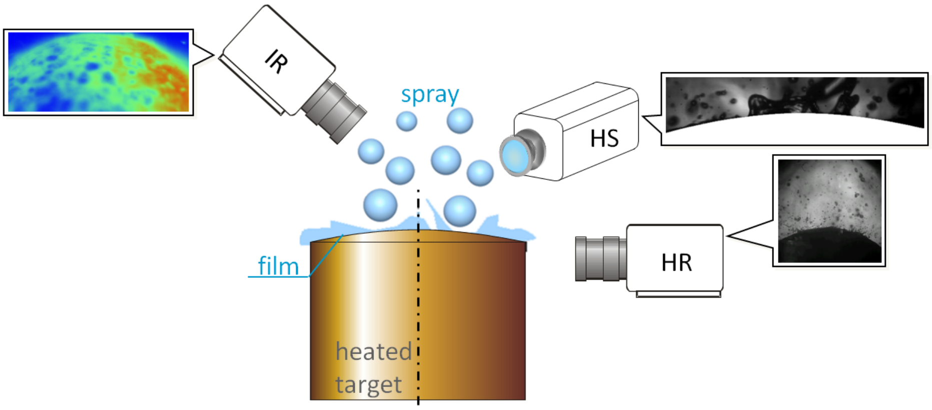

Figure 3.8: Camera system positioned close to the target: high-speed video system (HS), high-resolution camera system (HR), high-speed infrared camera (IR).

and a CMOS camera (Vosskühler HCC 1000) including a long distance microscope. The regions of spray-wall interaction and of the liquid film have been captured with a frame rate of 8000 fps and 1/21000 shutter time in series of 512 frames with a resolution of 512 x 128 pixel. Simultaneously, the images of the film-wall interaction have been collected at a frame rate of about 2 fps at 1024 x 1024 pixel using a high-resolution camera (FASTCAM Ultima 512) and an LED bulb for illumination. In addition, the target has been observed with a high-speed infrared camera (Phoenix, Indigo System Corporation) with a frame rate of 244 Hz in series of 100 frames. With the help of this high-speed infrared camera the film temperature pattern could be captured.

On board the TEXUS campaign a similar series of images have been captured at 15,000 fps using a high-speed camera Phantom 4.3 with a 10 μs shutter time and a resolution of 256 x 128 pixel. The high resolution camera Pulnix TM 4100 captured images at 5 fps and a resolution of 2048 x 2048 pixel. Despite this image processing it is strongly recommended to use uniform light illumination. In both cases, parallel light resulting from a LED field was pulsed and synchronized with the cameras.

During the centrifuge experiments the images of the spray-wall interaction have been captured at various gravity levels with a frame rate of 16,000 fps using a high-speed video system consisting of an LED light source producing uniform light and a CMOS camera named Photron FASTCAM SA1. The images have been captured with a shutter time of 1/80000 and a resolution of 512 x 256 pixel. The high frame rates have allowed observation of several stages of the same splash event.

During ground experiments the above-mentioned cameras have been used. In addition, images of the fluctuating film produced by the spray impact have been captured with the HighSpeedStar 5 camera from LaVision with a frame rate of 36,000 fps, a shutter time of 1/40000 at 512 x 128 pixel.

3.6 Measurement and control system

A number of measurement and control devices are integrated in each experimental rig. The functionality of the most important devices is presented in this section.

The water flow rate is measured with the help of a low volume rotating vane flow meter (KOBOLD Messring GmbH, DPM-1507G1C34P). The change of the water flow rate is physically based on a pressure difference. The liquid medium flows through a specially shaped fluidic casing and causes a vane to rotate. This rotary motion is sensed by optoelectronics in a non-contacting manner and converted to an analogue signal. By implementing a proportional control gate valve the water flow rate can be varied by changing the injection pressure in the water supply line. In addition, a bypass manual gate valve is included for security reasons in this supply system. According to the water supply system equivalent measurement and control devices are implemented in the gas subsystem.

The physical working principle of the gas flow meter (KOBOLD Messring GmbH, MAS-3017C400A) is based on a temperature difference. Two resistance temperature detectors are positioned on the measuring tube and deliver a constant heat quantity. At higher flow rates, the temperature difference increases. Again, a proportional control gate valve keeps the gas flux constant and can be varied by changing the injection pressure in the gas supply line and a bypass manual gate valve is included for security reasons.

The deposited liquid and the gas are exhausted from the cell using an extraction system. During parabolic flights there is the vent-line provided by the aircraft whereas for ground and other tests a vacuum pump is used. The pressure in the experimental cell is kept constant in the range of 0.8-1.0 bar using a pressure controller.

The temperature is measured with a set of thermocouples of Type K mentioned already in detail in the previous Section 3.4.

All data are collected with a data acquisition system of National Instruments consisting of a real-time controller with 256 MB DRAM, 400 MHz processor and 256 MB storage (NI cFP-2220). The embedded controller runs LabVIEW Real-Time for data logging, analysis, and process control. Several modules are connected to this compact field point system that feature input and digital output channels for each thermocouple and further devices as listed above. The Ethernet ports of the compact field point enable the transfer of the data and the LabVIEW platform where all these output signal informations are summarized is shown in the following Figure 3.9. With the help of this self-created user platform the main experimental systems, that is to say the water supply, gas supply and the heating system can be overviewed, operated and controlled by setting the desired parameters.

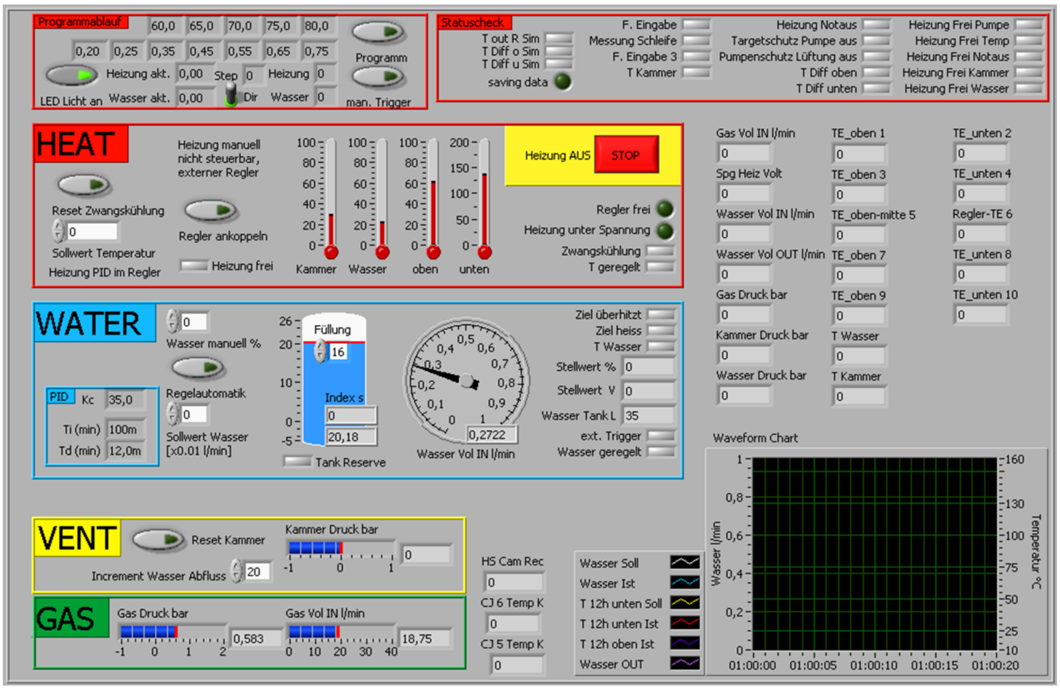

Figure 3.9: Data acquisition user platform providing an overview of all supply systems (water, gas, heating, vent-line) and created with LabVIEW.

3.7 Phase Doppler instrument

The quality of the spray has been tested with a phase Doppler technique in the laboratory. For this purpose, the inner life of the test cell consisting of the spray nozzle and the heated target, was integrated and built in the phase Doppler system as shown in the next Figure 3.10.

The phase Doppler instrument is an extension of laser Doppler velocimetry and is based upon phase Doppler principles and is based on light-scattering interferometry. For exploring and monitoring spherical drop sizes in sprays, light scattering instruments are the most common tool. Phase Doppler is an absolute measurement technique

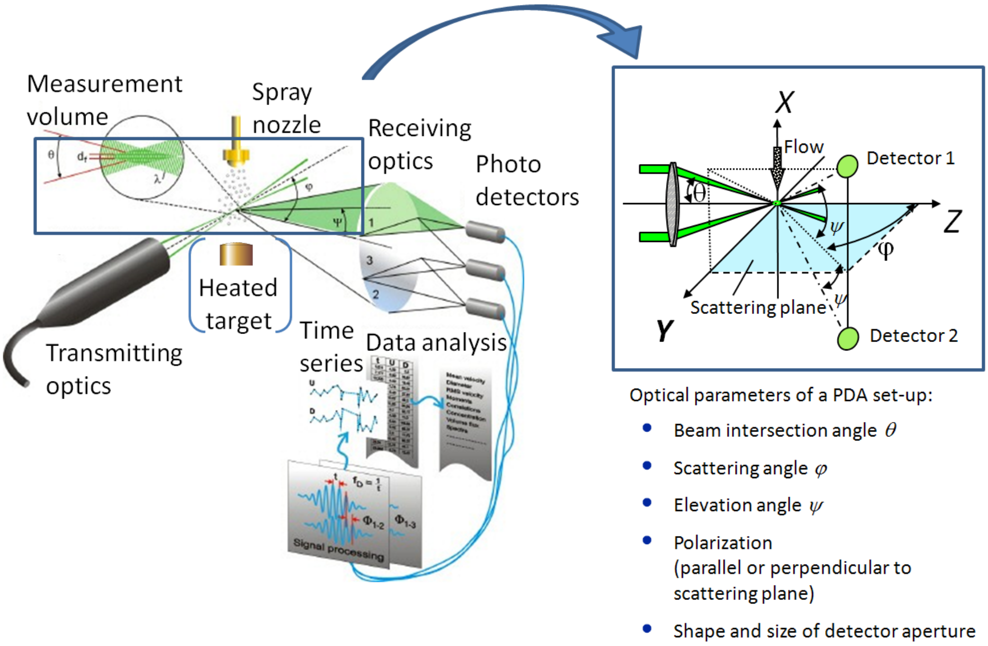

Optical parameters of a PDA set-up:

- Beam intersection angle θ
- Scattering angle φ
- Elevation angle ψ
- Polarization (parallel or perpendicular to scattering plane)
- Shape and size of detector aperture

Figure 3.10: Sketch of the test cell's inner life integrated in the phase Doppler system.

with high accurancy and high spatial resolution (small measurement volume). One advantage of the phase Doppler technique lies in the fact that no calibration is required. Due to illumination spray particles scatter light by the following three mechanisms: diffraction, reflection and refraction. The last mentioned mechanism occurs only for transparent particles. When using the phase Doppler system, two identical laser beams are crossed to form a pattern of light and dark illuminating fringes. The dimensions of this fringe-containing region define the measurement volume and they can be controlled by the optical arrangement.

The scattered light signals measured in our case by two photo detectors (see Figure 4.2) are processed to determine a drop velocity component at right angles to the fringes through the modulation frequency of the scattered light as it passes through the fringes. Particles thereby scatter light from the laser beams, generating an optical interference pattern. The drop sizes are found from the phase differences of the signals at the different photo detectors. While drop velocity measurements depend strictly on the frequency of the intensity variation of scattered light due to drop movement and fringe interactions, accurate drop diameter measurements depend on the spatial frequency of the scattered light. In essence, the scattered fringe spacing, or phase shift, is determined by the size of the scattering drop, while the frequency of the scattered light is a measure of the drop velocity. For this reason, at least two photo detectors are needed to measure drop diameters.

The optical arrangement for the phase Doppler technique can be also found in the work of Durst and Zaré (1975), Flögel (1981), Bauckhage and Flögel (1984), Bachalo and Houser (1984). The photo detectors are positioned out of the plane of the incident beams at an angle φ, usually known as the off-axis angle. The detectors are placed symmetric out of the y-z plane by the angles ψ, the elevation angles (see Figure 3.10).

A receiving optics placed at a well-chosen off-axis location projects a portion of the scattered light onto multiple detectors. Each detector converts the optical signal into a Doppler burst with a frequency linearly proportional to the particle velocity. The phase shift between the Doppler signals from different detectors is a direct measure of the particle diameter (Dantec Dynamics (2005)). Again, further information about the phase Doppler measurement technique can be found in a more detailed way in the book of Albrecht et al. (2003) as well as in the manual of Dantec Dynamics (Dantec Dynamics (2005)).

3.8 Experimental platforms

An overview of the experimental platforms included in the project structure is presented in Figure 3.11. It consists of four subprojects: ground based tests in laboratories, parabolic flights, an experiment on board TEXUS 45 (**T**echnologische **EX**perimente **U**nter **S**chwerelosigkeit) and centrifuge tests.

The experiments at zero gravity conditions have been performed during parabolic flight campaigns and on board of a ballistic rocket. Parabolic flights give researchers the possibility to work in situ directly on their experiment and observe them investigations in time, more complex reading to be obtained and if needed to interfere. Several repetitions of each experiment can be carried out on one flight day. In addition, up to 31 parabolas during one parabolic flight day enable a study with up to 31 different parameters. Although these flights attain less free-fall microgravity time than sounding rockets, its costs relative to the weight of experiments that can be carried makes these flights very cost efficient. Sounding rockets have the advantage of being relatively low cost. They are a cheap way of obtaining microgravity opportunities with a longer duration of typically 5-7 minutes compared to only 22 seconds during parabolic flights. Adjacent to the testing time, the quality of microgravity is much higher than on parabolic flights. One disadvantage is that sounding rockets do not offer researchers to be on hand on board and that direct intervention and changing of parameters through telecommand is not as easy as during parabolic flights. Therefore, pretests are often

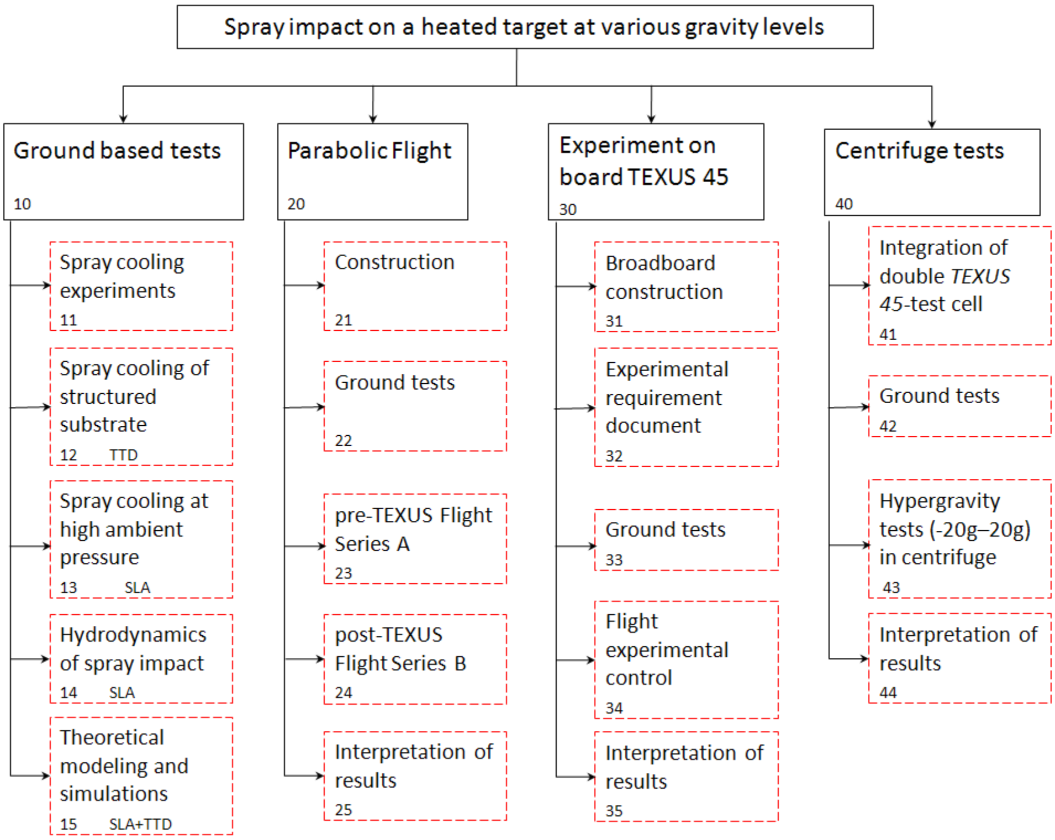

Figure 3.11: Platforms and subprojects for experimental investigations on spray impact on a heated target under various gravity levels.

performed in advance during parabolic flights in order to define the parameter field and to make a definite preselection for sounding rocket experiments. Regarding the positive and negative hypergravity experiments, they have been performed in a centrifuge at ZARM. Experiments in a centrifuge provide a very flexible access to various gravity levels for a large range of scientific experiments and technological tests. In addition, many experiments can be performed throughout a day and the experimental time is not limited as for the microgravity case once the desired gravity level is reached.

Hence, for our investigations different - according to the constraints modified - physical experimental setups have been built *ab initio* maintaining, as a matter of course, one common physical working principle already explained in Chapter 3.1.

3.8.1 Parabolic flights

NOVESPACE, subsidiary of the French National Space Center (CNES) owns and operates the Airbus A300 ZERO-G during parabolic flight campaigns. Parabolic flights are the only sub-orbital carrier to provide the opportunity to carry out experiments under simulated weightlessness conditions. They are used to conduct short-term microgravity scientific and technological investigations, e.g. to test instrumentations and systems in preparation prior to use in long-duration space missions, to validate operational and experimental procedures, to perform biomedical research experiments on human test subjects and to train astronauts for a future space flight. Researchers use microgravity to investigate biological processes, material experiments, chemical reactions and in detail various liquid flows governed by capillary forces.

Figure 3.12: ZERO-G aircraft carrying out parabolic flights and simulating weightlessness.

Our experimental fluid physics problem has been also firstly approached on the ZERO-G during several parabolic flight campaigns by eliminating gravity. Spray impact as well as spray cooling have been investigated on the following parabolic flight campaigns: 9^{th} and 10^{th} DLR- parabolic flight campaigns, 44^{th} ESA-parabolic flight campaign.

The ZERO-G flights are conducted on a specially-configured aircraft of the type Airbus A300 achieving weightlessness by following an elliptic flight path relative to the center of the earth as described in Thomson (1986). While following this path, the aircraft and its payload are in free fall. During this time the aircraft does not exert ideally any g-forces on its contents. The common microgravity level during those campaigns amounts ± 0.05g.

Initially, from horizontal flight position the aircraft first gains momentum at full thrust and then climbs up steeply with a pitch angle of about 45 degrees. At this point, all experimenters and devices on board the aircraft experience a force of 1.8g meaning 1.8 times the earth's standard gravitational acceleration, pulling them towards the floor of the Airbus A300 ZERO-G. By throttling the engines back, reducing thrust and lowering the nose to maintain a zero angle of attack, simulated weightlessness is achieved. As illustrated in Figure 3.13 this simulated microgravity period (highlighted in red) begins while ascending and lasts all the way "up-and-over the hump", until the ZERO-G aircraft reaches a declined angle of about 42 degrees. The period of microgravity lasts for a period of 20 to 22 seconds, during which there is only a residual acceleration of about one percent of the earth's gravitational pull (DLR (2008)). At this point, the aircraft has lost a significant amount of altitude, and the pilot must begin to pull out the aircraft of its steep descent on the way down. Again, positive hypergravity occurs, for about 20 seconds, the forces are roughly twice that of gravity. After this maneuver, the aircraft returns to the horizontal flight for a period of about one minute, during which the earth's normal gravitational pull returns. Subsequent, the ZERO-G aircraft is ready for being pulled again halfway up its upward trajectory so that the pilot can initiate the zero-g flight path. The Airbus A300 ZERO-G flies up to 31 parabolas daily during its total 3-4 hour flight including take-off and landing (see Figure 3.13). In general, five parabolas follow consecutively, one after another but in between those parabola packages there is a break of up to 8 minutes. In this rest period, researchers have the opportunity to change parameters and to focus on new settings. During one flight campaign, which normally consists of three individual flight days, around 93 parabolas are flown in total meaning that about 90 different parameter sets can be carried out.

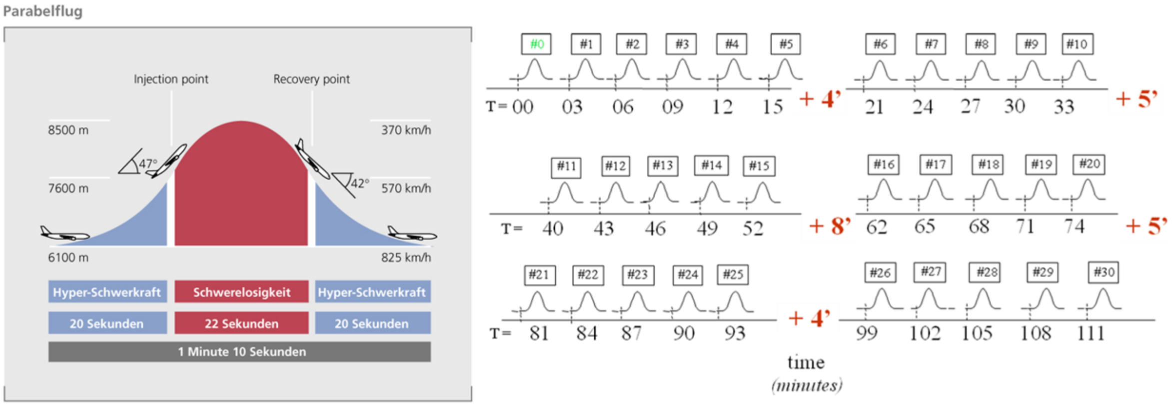

Mit freundlicher Genehmigung durch Kpt. Gilles Le Barzic

Figure 3.13: Explanation of one single parabola with three main phases (1.8g - μg - 1.8g) resembling an ideal ballistic curve. On each parabola, there are two periods of increased gravity (1.8g) that last for 20 seconds immediately prior to and following the 22 seconds period of microgravity (left). Illustration of parabola sequences during one flight campaign (right).

The initial experimental setup including a prototype test cell for spray cooling investigations has been designed, constructed and built for the first parabolic flight campaign. Figure 3.14 illustrates the interior of the Airbus A300 ZERO-G and the experiment positioned in the aircraft from two different perspectives. Regarding the capacity during one flight campaign, the number of experiments on boards amounts approximately 13.

The parabolic flight experiments have served as a test for preparation of the sounding

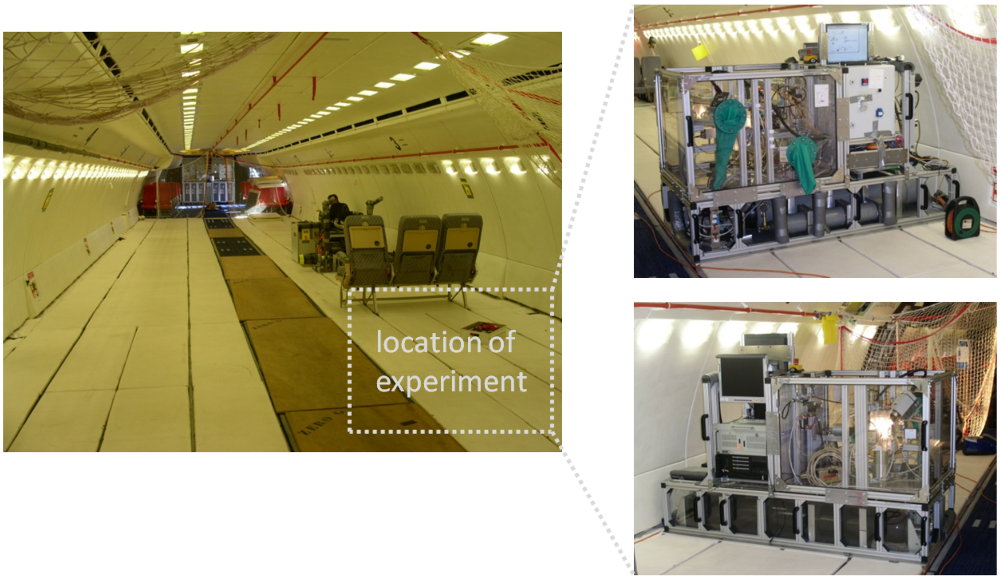

Figure 3.14: The interior of the Airbus A300 ZERO-G with the mounted experiment (front and rear view).

rocket experiment. The objective throughout all campaigns has been to check the parameters of the experiment which will be later used in the sounding rocket experiment such as the required power supply, the volume flux of the air necessary to ventilate the chamber, the functionality and reliability of the controlling electronic equipment.

3.8.2 Sounding rocket

A sounding rocket, sometimes called a research rocket, is an instrument-carrying rocket designed to take measurements and perform scientific experiments during its sub-orbital flight. The origin of the term comes from nautical vocabulary, it refers to sound, which means to throw a weighted line off of a ship to gauge the water's depth. It is intended here as taking a measurement (Marconi (2004)).

A continuative experiment has been operated on board of a ballistic sounding rocket within the framework of the TEXUS 45-campaign. The TEXUS project is a sounding rocket program with the primary aim to investigate the properties and behavior of materials, chemicals and biological substances in a microgravity environment comparable to the parabolic flight campaigns. One significant difference is the microgravity duration as the TEXUS program provides a longer duration with around six minutes of continuous microgravity, rather than just 22 seconds during parabolic flights.

The TEXUS rocket follows a parabolic path with an apogee to the extent of 250 km, depending on the payload weight. The two-stage solid-fuel rocket has a length of 13

m. Approximately 75 seconds after the launch the rocket drive is separated from the payload. For six minutes, conditions of approximate weightlessness prevail. Since the aerodynamic drag is very low in the first six minutes of the ballistic flight phase, the acceleration that is affecting on the payload is reduced to 10^{-4}g for this time duration. When re-entering into the atmosphere, the payload of the rocket, meaning the tip that contains the experimental set-ups as well as the recovery and data communication systems, is being decelerated by a parachute. After having securely reached the ground, every part is transported back to the launch site by a helicopter.

All missions are launched from the European rocket launch site ESRANGE near Kiruna in the Northern part of Sweden.

The TEXUS 45 rocket contains a Brazilian two-stage solid-fuel rocket drive named VSB30 and the payload consisting of reusable cylindrical system elements of a 438 mm diameter. The total length of the payload amounts to approximately 4 m. A typical rocket assembly with the system elements contains several scientific experiments accommodated in modules stacked one atop the other, the service system for the data communication and the feedback position control as well as the landing unit with the parachute. Figure 3.15 illustrates the total payload of the TEXUS 45-campaign with a weight of 367 kg. It contains in total three experiments on board. Our experiment is positioned in the middle part and is named “Sprayaufprall auf beheizte Oberflächen” (Spray impact onto a heated target).

Each experiment is directly monitored and controlled by researchers on the ground through telecommanding and TV streams. Scientific data are either directly transmitted during the flight by telemetry or saved after the payload has been recovered.

The experiment module has been designed, constructed and built at the company EADS Astrium GmbH in Trauen. The experimental configuration is based on the technical expertise gained during the previous parabolic flight campaigns. It allowed essential improvements of the system boundary conditions. The functional build-up is shown schematically in Figure 3.16.

The physical principle has been already described in Section 3.1. In comparison to the parabolic flight experiments the test cell construction differs as well as the heating method, the total amount of water and gas needed to be carried on board. Due to the experiment time of only six minutes for example 3 l in the water reservoir were sufficient compared to a 50 l water tank for one parabolic flight day.

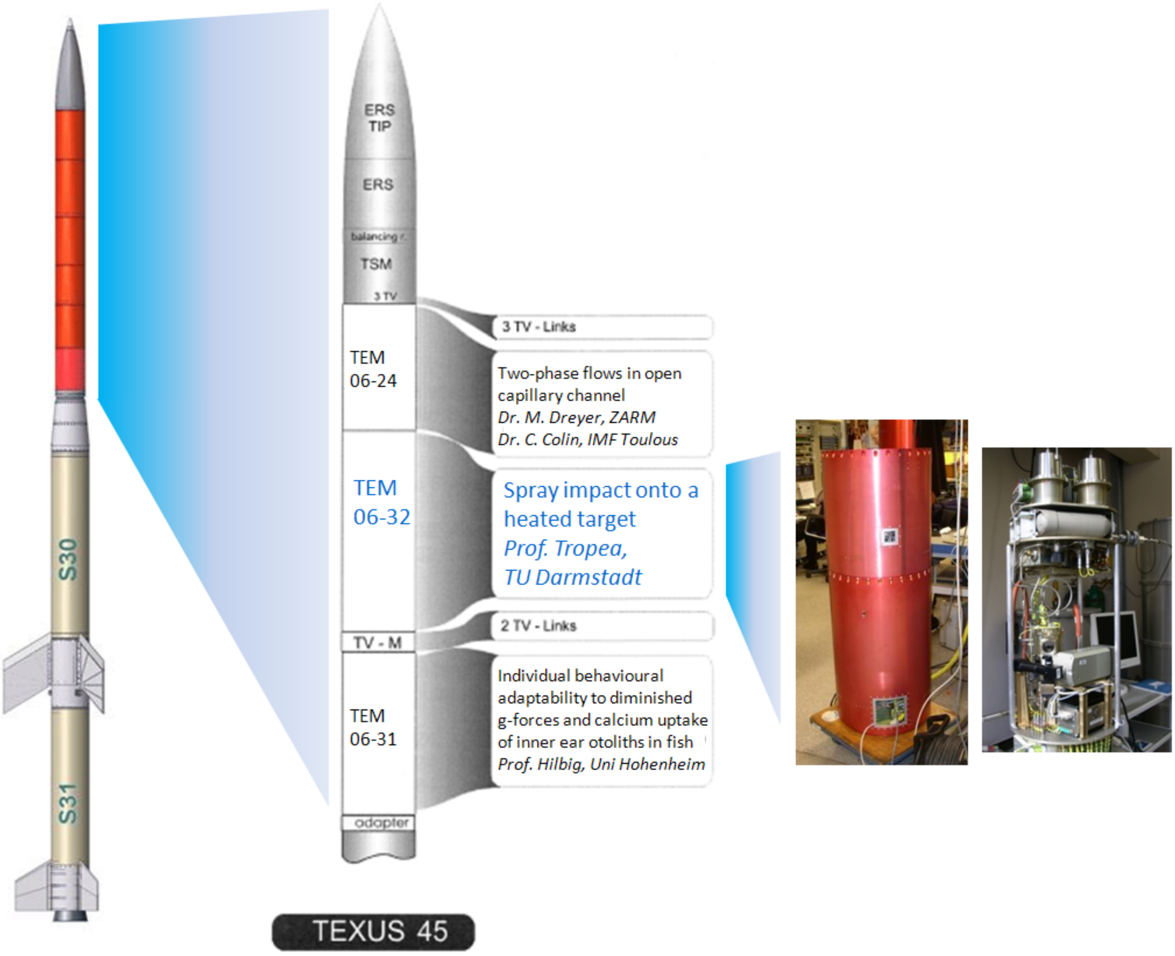

Figure 3.15: Scheme of the sounding rocket TEXUS 45 with its payload containing three experiments on board.

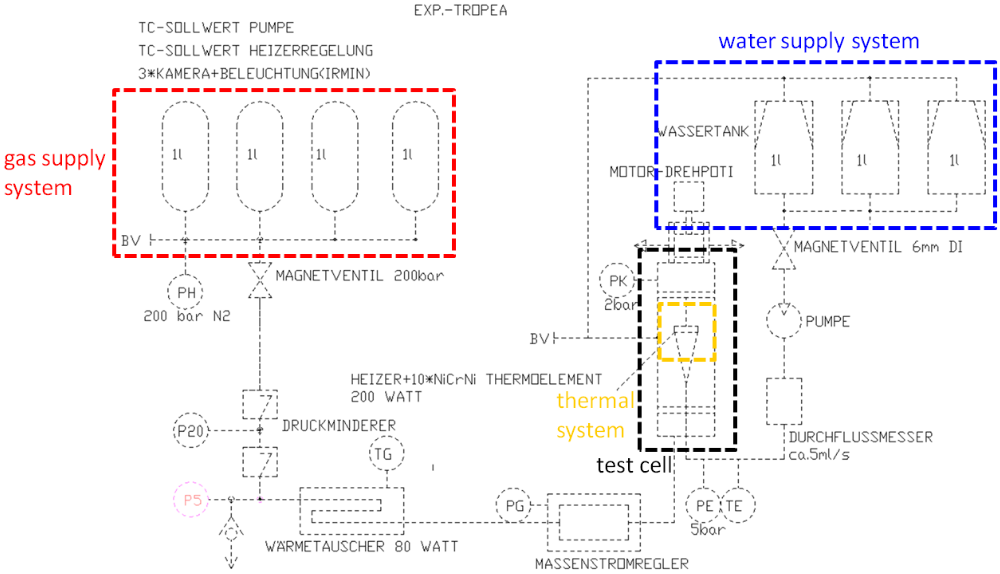

Figure 3.16: Functional chart of our TEXUS 45 experiment with diverse supply systems.

3.8.3 Centrifuge facility

For the first time, investigations in the field of fluid physics are performed in the centrifuge at ZARM, Centre of Applied Space Technology and Microgravity at the University of Bremen. It is offering a unique opportunity for carrying out experiments under a centrifugal acceleration of up to 30g. Within ZARM, the centrifuge acts as a counterpart to the Drop Tower facility, where experiments are carried out under microgravity.

Compared to ZERO-G and TEXUS experiments the Centrifuge facility provides full access and control during the testing phase that might even last for weeks or months. This fact has been a tremendous advantage while investigating throughout the campaigns. The connection of the centrifuge through a slip ring offering nearly all imaginable links for any supply system makes it possible to design experiments that have neither drawbacks nor limitations compared to a common experimental setup. Figure 3.17 shows the centrifuge facility including the base frame and the rotor shaft with two arms and struts. The front and already prepared capsule with the table always contains the experiment whereas the other one functions as a counter balance. The platform diameter amounts to approximately 13 m.

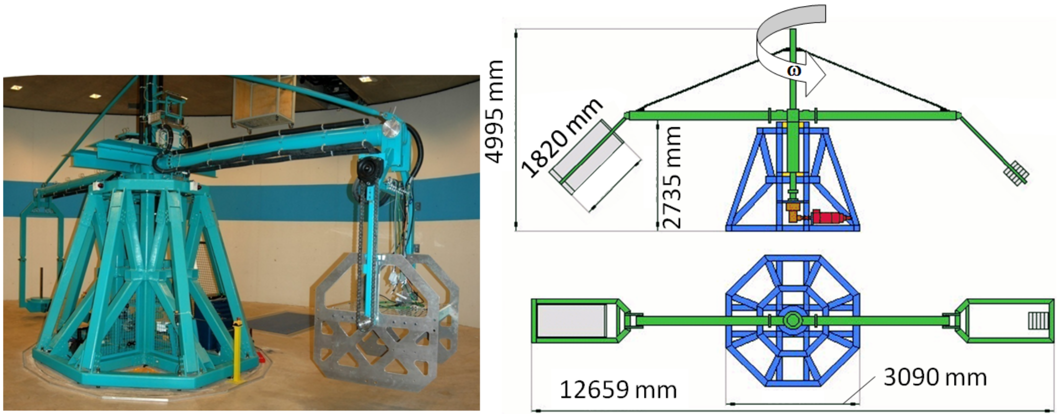

Figure 3.17: Centrifuge at ZARM (left) and scheme of the facility (right, side and top view).

Our experimental rig with a size of approximately 1 m^3 has a weight of around 140 kg. Again, the main core of the experiment is the test cell where spray impingement occurs onto a heated target. It is exactly the same one as used during the TEXUS 45 campaign.

The spray was impacting in the direction of the gravitational force during ZERO-G and TEXUS investigations, the experimental procedure has been modified for the centrifuge experiments. The test cell has been positioned in two different geometric configurations (see Figure 3.17) allowing us to investigate spray impact at positive hypergravity (+ύg) as well as at negative hypergravity (-ύg) conditions in the range of -20g to 20g.

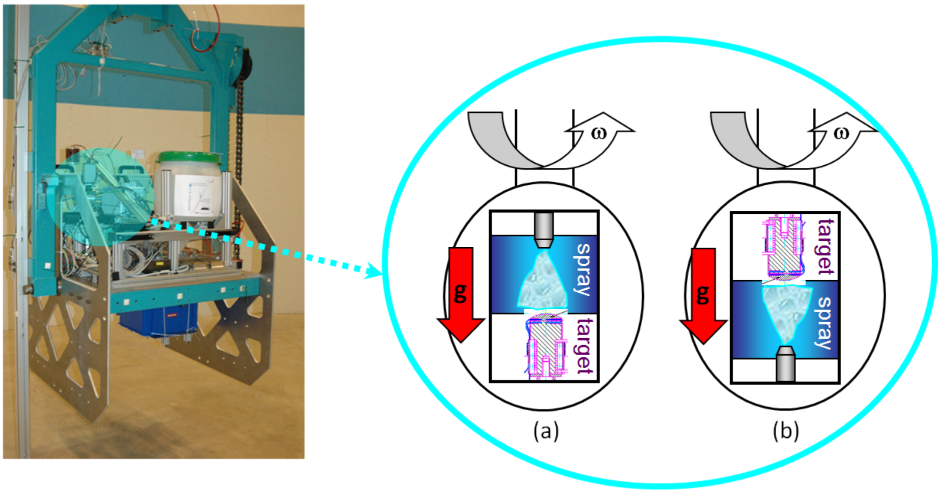

Figure 3.18: Experimental configurations of the test cell for (a) positive hypergravity (+ύ) and (b) negative hypergravity (-ύ) condition.

Thus, the parameters have been changed in comparison to those of the microgravity experiments. An overview of the expanded parameter field for the positive hypergravity investigations is given schematically in Section 3.9.

Under operating conditions the centrifuge rotates through the vertical axis so that inertial forces - additional to the earth's gravitational force - take effect outwards to the capsule mounted on the horizontal arm. Hence, the coordinate system is not inertial for the experiment platform. The determining factor is therefore the resulting system acceleration that arranges due to the mounting of the capsule always in a way that the mounting and center of gravity are aligned parallel to the resultant. The resulting acceleration affects perpendicular to the seating of the capsule. During start-up and run-down of the centrifuge tangential accelerations occur. To minimize their influence, our investigations were only performed at constant rotational speed.

3.8.4 Ground experiment

Each experimental rig for the respective platform has been tested in the laboratories under ground conditions. The same parameter field was passed through in order to ascertain that the experiment functions faultlessly and is ready for the designated platform. In addition, the spray has been characterized with a phase Doppler instrument under ground conditions.

3.8.5 System configurations

An overview considering all experimental platforms and the system modifications is given in Table 3.1. As previously presented, the target has been heated either with cartridges in the primary investigations or with a wire (since the 10^{th} DLR-PFC). Regarding the cameras, the application of the high-speed, high-resolution and infrared camera are optional and not integrated in all platforms at the same time. Due to space reasons, the only measurement system that comes into operation on ground is the phase Doppler instrument.

Table 3.1: Variations of system configuration for diverse experimental platforms.

		44th ESA	9th DLR	10th DLR	TEXUS 45	1st+2ndZARM	3rd +4th ZARM	ground
heating system	cartridges	♦	♦					♦
	wire			♦	♦		♦	♦
camera system	HSC	❖	❖	❖	❖	❖		❖
	HRC	❖	❖	❖	❖			❖
	IRC	❖	❖					❖
Phase Doppler								★

3.9 Experimental program

Table 3.2 gives an overview of the experimental investigations and the operation parameters. The water flow rates are chosen such that the results are comparable throughout the campaigns. In addition, the minimum requirement for each experimental platform (not campaign, see Figure 3.1)is one high-speed camera in order to take spray images. One significant parameter that varies is the gravity level according to the experimental platform and indirectly the test cell configuration as presented in Figure 3.18 for the centrifuge experiments.

Figure 3.19 shows high-speed images according to the water flow rate, the gravity level and the configuration, combined into numerous detected parameters during microgravity and positive hypergravity experiments. The chart on the right illustrates how the change of the water flow rate affects the high-speed images for a constant gravity level of 2g. In a next step, the water flow rate is kept constant at 0.25 l/min

Table 3.2: Overview of the experimental program for each platform.

		44th ESA	9th DLR	10th DLR	TEXUS 45	1st+2nd ZARM	3rd ZARM	4th ZARM	ground
water flow rate [l/min]	0.25		●	●		●	●	●	●
	0.35		●	●		●	●	●	●
	0.45	●	●	●	●	●	●	●	●
	0.55		●	●		●	●	●	●
	0.65			●		●	●		●
gravity level	-20g							■	
	-16g							■	
	-12g							■	
	-8g							■	
	-4g							■	
	-2g							■	
	µg	■	■	■	■				
	1g	■	■	■					■
	2g	■	■	■		■	■		
	4g					■	■		
	6g					■	■		
	8g					■	■		
	10g					■	■		
	12g					■	■		
	14g					■	■		
	16g					■	■		
	18g					■	■		
	20g					■	■		

but the gravity level is changed from μg, 1g (ground), 2g up to 20g (+úg). The bottom high-speed images are taken at 2g, 8g, 12g, 16g and 20g (from left to right). This combined data points (water flow rate ranges from 0.25 l/min to 0.65 l/min, gravity level from μg to 20g) are displayed in blue in the right diagram. The -úg-images represent a third variation in experiments (see configuration in Figure 3.18). The high-speed images in Figure 3.19 are captured at a constant gravity level of -2g and for various water flow rates from 0.25 l/min to 0.65 l/min.

The parameter field we are investigating is g $= \pm$ 20, Re $\approx$ 500-600 and We $\approx$ 20-1000.

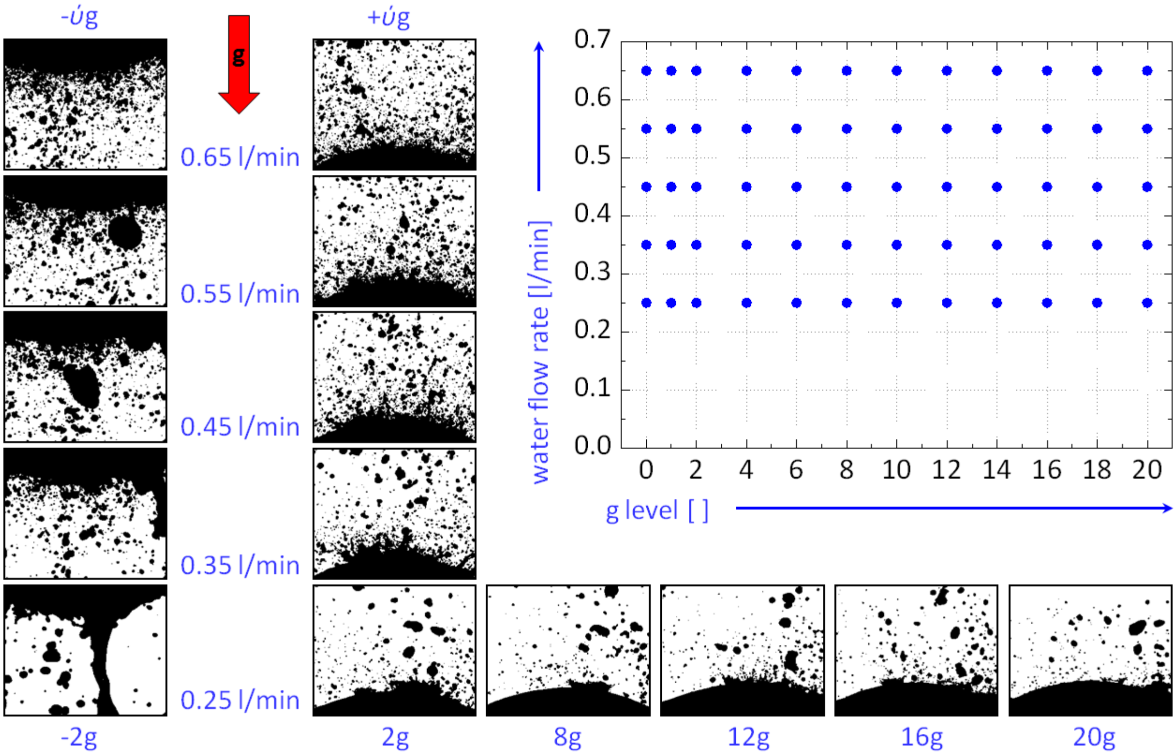

Figure 3.19: Overview of the parameter field illustrated with appropriate high-speed spray images. Variation of the water flow rate, the gravity level and the test cell configuration.

Chapter 4

Spray characterization

The main regions of interest are shown in Figure 4.1: primary and secondary spray (violet highlighted area) and liquid film hydrodynamics (blue highlighted area, see Chapter 5). According to the studied field, different techniques are used. In this chapter we are focusing on the characterization of the spray. Our research strategy is to define some spray parameters of the primary spray impinging onto the surface and secondary spray splashing from the surface. Due to the instability of the liquid sheets as it is mostly the case, they break up into secondary drops.

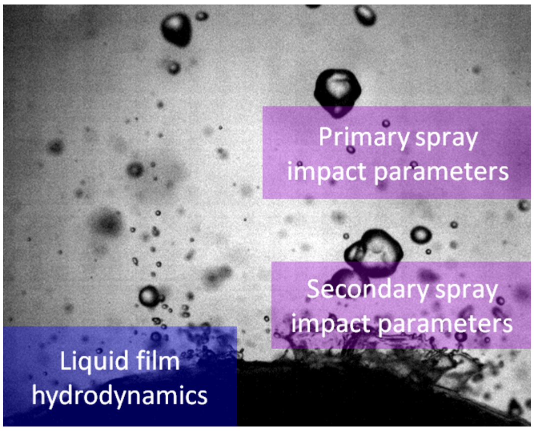

Figure 4.1: Two main regions of research interest: primary and secondary spray parameters (highlighted in violet) and liquid film hydrodynamics (blue).

One common method to characterize spray is the phase Doppler instrument. By using this technique, the spray parameters such as drop diameter and drop velocity components are characterized in the laboratory. It is commonly used in industrial and laboratory environments and one of the principal spray measurement techniques used in the laboratory environment.

In addition, an image processing software based on shadowgraphy has been programmed with assistance of a commercialized MATLAB image processing tool box. The high frame rates of the captured images allow observation of several stages of the same splash event. Hence, important characteristics relevant to splash and film dynamics can be evaluated.

The image processing technique has a great advantage when people are interested in the particle shape. In comparison to the shadowgraphy method, the phase Doppler method only takes into account almost spherical particles. Also, measurements are performed on single particles, thus allowing detailed analysis of particulate flows whereas the image processing tool detects all drops taken at one certain time in one captured image.

4.1 Phase Doppler measurements

4.1.1 Experimental system

A Dantec Dynamics dual-mode phase Doppler system using an argon-ion, water cooled laser utilizes green, blue and violet laser beams at 514.5 nm, 488 nm and 466.5 nm wavelengths (see Figure 4.2). Because of the particle sphericity checking at two different view angles, the dual mode PDA system has more stringent sphericity tolerance than the fiber PDA. The phase Doppler system is operated in first order refraction scatter and measures three velocity components simultaneously such as the axial velocity u and the transverse velocities v and w as well as the corresponding drop diameter. As displayed in Figure 4.2, the phase Doppler system consists of a laser light source, two transmitting optics, receiving optics, a signal processor and a data acquisition system (not shown in this figure).

Table 4.1 presents the most important phase Doppler system configurations of the transmitting and receiving optics. The measurement volume should be small enough such that no more than one drop at any time is placed within this region. Therefore, compared to the image processing method where a multitude of drops are detected in one single image, the phase Doppler instrument is a single particle counting technique and can accept drops arriving at up to 250 kHz.

The phase Doppler instrument is used to measure the diameter and the velocities of the spray drops passing through given positions in the spray. The measurement point is defined by the intersection of the focused laser beams passing through a 200 μm pinhole

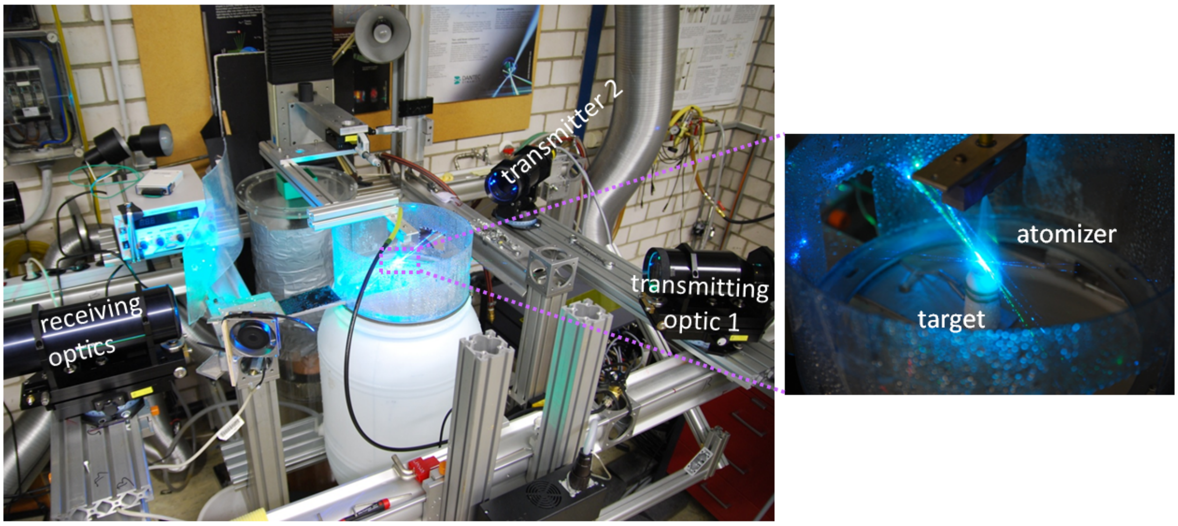

Figure 4.2: Experimental setup of the phase Doppler instrument with laser, two transmitting optics and receiving optics (left) and with the integrated target and atomizer zoomed in (right).

Table 4.1: Phase Doppler optical configuration.

Transmitting optic			
Beam system	U1	U2	U3
Wavelength [nm]	514.5	488	476.5
Focal length [mm]	600.00	600.00	600.00
Beam diameter [mm]	1.35	1.35	1.35
Expander ratio	1.98	1.98	1.98
Beam spacing [mm]	38.75	38.75	38.75
Frequency shift [MHz]	40.00	40.00	40.00
PDA receiver			
Receiver type	112 mm Dual PDA		
Scattering angle [deg]	30.00		
Receiver focal length [mm]	500.00		
Mask [Aperture]	Mask C		
Spherical validation band [%]	10.00		
Eff. slit width [mm]	0.2000		
Probe volume dx [mm]	0.1473	0.1398	0.1365
Probe volume dy [mm]	0.1470	0.1395	0.1362
Probe volume dz [mm]	2.3050	2.1860	2.1340

to the receiving optics and the measurements are performed on single particles as they move through the sample volume. Figure 4.3 illustrates schematically the mesh of the measurement planes and point positions. It ranges from −10 mm to +10 mm along the x- and y-direction with a 1 mm spacing between measuring points. In addition, the measurements were carried out at four different angles 0°, 45°, 90° and 135° in order to characterize the whole spray periphery. The experiments were performed at different heights close to the target's surface and for a constant height at various axis and angle positions. The phase Doppler technique was applied for both configurations, with (4.1.2) and without the target(4.1.4). The axial velocity u is defined as positive in the spray impacting direction as illustrated in Figure 4.3, paying attention that this definition changes for the negative hypergravity configuration (compare Figure 3.18).

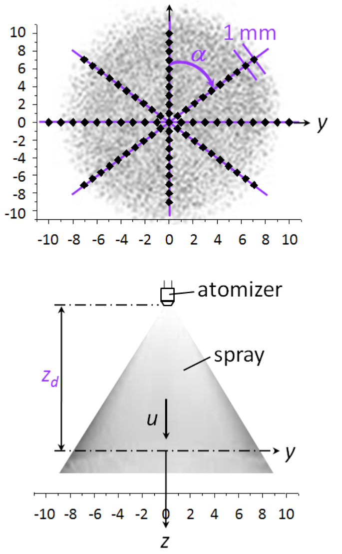

- Various axes at a distance of 1 mm for a constant height z_d

α = 0°, 45°, 90°, 135°

- PDA-measurements at different distances from the atomizer, z_d = const.

without target: z_d = 70 mm (≈ target surface)
with target: z_d = 65 mm and 68 mm

Figure 4.3: Phase Doppler measurement planes and points with varying angles α= 0°, 45°, 90° and 135° and different measurement distances z_d according to the experimental configuration.

4.1.2 Primary spray characterization without target

In order to understand the mechanisms of the spray-wall interaction detailed information on all influencing parameters are needed. A parametrical study is made to investigate the drop size distribution and velocity profiles of the primary and secondary spray parameters. One of the significant factors determining the hydrodynamic process is the primary spray generated by the full-cone pressure swirl atomizer. For the primary spray measurements without the target, phase Doppler data have been collected at one certain distance from the nozzle as shown in Figure 4.3. The reason for choosing the 70 mm distance is that the target's surface is supposed to be positioned there. If we analyze the primary spray in the configuration without the target for a constant water flow rate $\dot{V}$ but along different measurement axes (angles 0°, 45°, 90° and 135°), we receive the following results. Figure 4.4 displays the axial drop velocity for a constant water flow rate $\dot{V}$ (here 0.35 l/min) at certain measurement points along the axis α= 0°(red), 45°(green), 90°(blue) and 135°(violet). This figure proves the fact that our nozzle produces a very homogeneous spray. Independent from the measurement angle α, all velocity distributions agree very well. In addition, the maximum is at x = 0, the central spray position (according to the nozzles fixation, see Figure 4.3). One reason for the velocity shift in the region of 4 mm < x < 10 mm may be the quality of the data. Since those investigations take place at the end of a measurement axis meaning on the "back side" of the arriving laser beam, the measurement conditions are worse. Less laser power reaches the measurement position leading to lower signal power and the detection of rather large spherical drops.

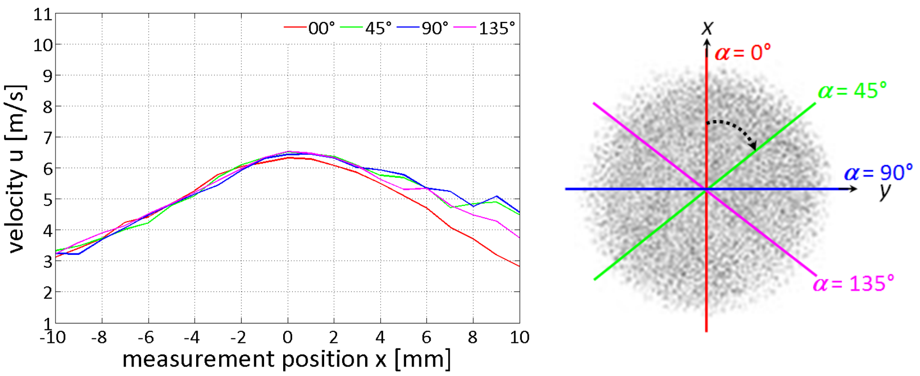

Figure 4.4: Axial velocity u for a constant water flow rate of 0.35 l/min measured along different axes (α = 0°, 45°, 90° and 135°).

Since our spray is homogeneous in reference to the velocity distribution and as later on also shown in the drop size distribution (see Figure 4.7), we continue our analysis for the main measurement axis $\alpha = 0°$ and 90° and compare the results between three different water flow rates: 0.35 l/min, 0.45 l/min and 0.55 l/min in Figure 4.5. Again, there is no dramatic change in the resulting velocity distribution between $\alpha = 0°$ and $\alpha = 90°$ for all water flow rates. The spray remains uniform and the characteristics are similar with a maximum in the zero-point of nozzle origin. However, the change of the water flow rate $\dot{V}$ affects the drop velocity. Figure 4.5 illustrates an increase of the axial velocity u at a higher water flow rate.

Regarding the two transverse velocities v and w, it is obvious in Figure 4.6 that both velocity components are very small compared to the axial velocity u. Especially the

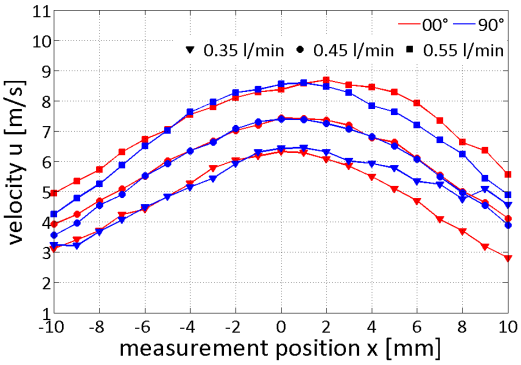

Figure 4.5: Axial velocity u for various water flow rates 0.35 l/min, 0.45 l/min and 0.55 l/min measured along different axes ($\alpha = 0°$ and $90°$).

velocity component w seems irrelevant for our studies. In addition, we can already demonstrate as follows with the help of a basic calculation that our spray image processing analysis is not affected by v and w. Taking a maximum value of 1 m/s for the transverse velocity, we receive for one drop with a time shift of $\Delta t = 62.5\ \mu s$ between two successive images a resulting track $\Delta s = 62.5\ \mu m$ which is insignificant compared to the depth of focus with ≈ 2 mm. Hence, especially the transverse velocity component w can be neglected.

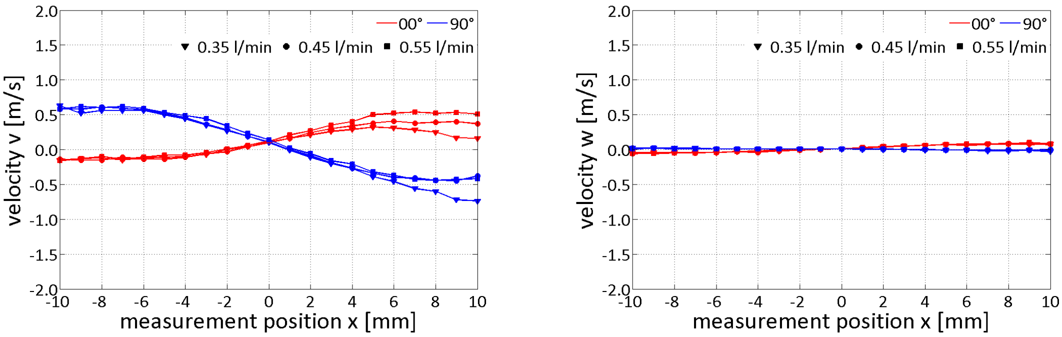

Figure 4.6: Transverse velocities v and w for various water flow rates 0.35 l/min, 0.45 l/min and 0.55 l/min measured along different axes ($\alpha = 0°$ and $90°$).

For the analysis of the drop sizes there are two main parameters that can be considered: the mean drop diameter D_{10} or the Sauter mean diameter D_{32} (SMD). Comparing again the results for the different measurement axes around the spray for a constant water flow rate of 0.65 l/min, it is obvious that the drop diameters D_{10} and D_{32} agree very well and the measurement axis has no significant effect on the drop diameter. Hence, D_{10} and D_{32} can be assumed to be constant over all measurement angles ($\alpha = 0°$, $45°$, $90°$ and $135°$). In Figure 4.7, the different colors represent the measurement angles (illustrated also in Figure 4.4) as well as the mean diameter of the drops D_{10} as dashed line and the SMD distribution D_{32} as continuous line.

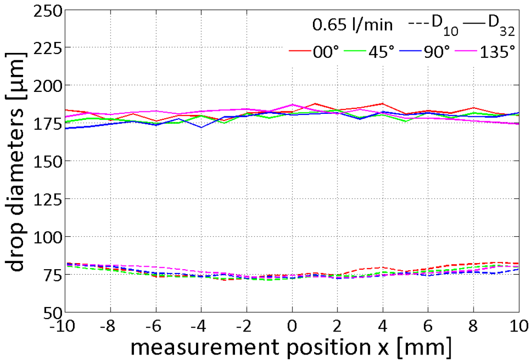

Figure 4.7: D_{10} and D_{32} distribution measured along the axes for different angles ($\alpha = 0°$, 45°, 90° and 135°) for a constant $\dot{V} = 0.65$ l/min.

Therefore, we focus only on the results for one measurement plane, here exemplary chosen $\alpha = 0°$. Figure 4.8 displays the primary spray distribution of both diameters, D_{10} as well as D_{32} for various water flow rates. Both diameters do not change significantly at different measurement positions x but there is an essential difference of about 100 μm in the drop size when comparing D_{10} with D_{32} for a constant water flow rate. Figure 4.8 also illustrates that in general the drop sizes decrease at higher flow rates.

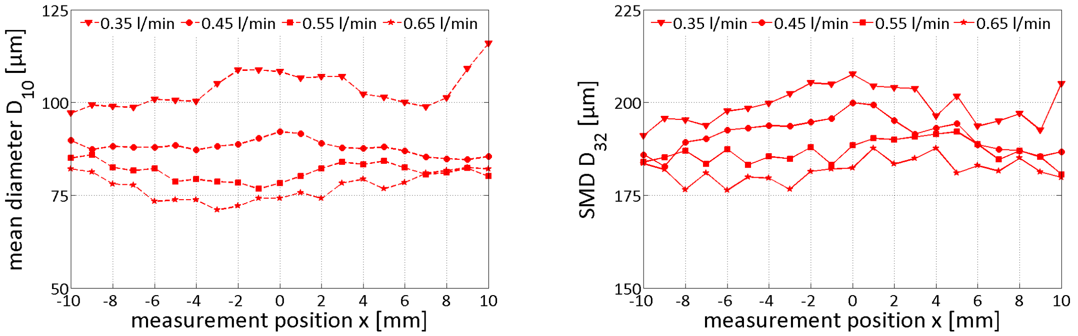

Figure 4.8: Drop diameter distribution D_{10} and D_{32} for various water flow rates (0.35 l/min - 0.65 l/min) along one measurement axis ($\alpha = 0°$).

4.1.3 Spray characterization in the presence of target

The experimental phase Doppler investigations with the target have been performed for the region -12 mm $<$ x $<$ +12 mm in order to guarantee second spray detection outside the target's zone. There are results for two different distances from the nozzle (see Figure 4.2), as close as possible to the target's surface at $z_d = 65$ mm and $z_d = 68$ mm.

In the following we are focusing on the primary as well as on the secondary spray and its velocity and diameter distribution. In Figure 4.9 firstly the impact velocities are compared between the two distances $z_d = 65$ mm and $z_d = 68$ mm for two water flow rates 0.35 l/min (left) and 0.55 l/min (right). In general, there is a difference between u_{prim} for $z_d = 65$ mm or $z_d = 68$ mm of about 1 m/s. Again, it is obvious that the values for u_{prim} are higher with an increase of the water flow rate $\dot{V}$ as also previously displayed in Figure 4.5 but by contrast the characteristics of 0.55 l/min varies. One reason for this behavior can be the disturbance of the secondary spray created due to spray impact onto the target. The phase Doppler drop detection seems to be influenced stronger at greater water flow rates.

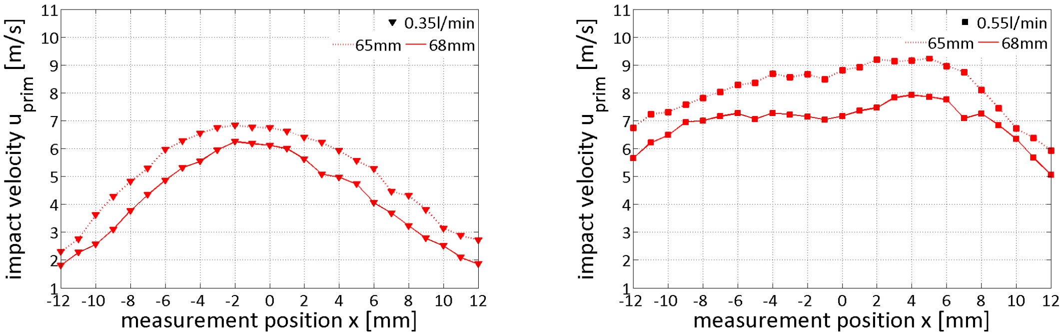

Figure 4.9: Axial velocity u_{prim} of the impacting spray along one measurement axis ($\alpha = 0°$) for a water flow rate of 0.35 l/min and 0.55 l/min.

In analogy to Figure 4.9, Figure 4.10 gives the results for the secondary spray velocity u_{sec}. There is no significant change at 0.35 l/min in comparison to 0.55 l/min. The number of secondary drops compared to primary drops are significantly higher with an increase of $\dot{V}$. In this case, the spray is so dense enabling only signals of large drops. On this account, the results are varying stronger. In addition, for both water flow rates, the measurement plane ($z_d = 65$ mm and $z_d = 68$ mm) has no influence on the axial velocity component of the secondary spray (u_{sec}).

For a well-defined comparison of the transverse velocities v and w, the results for only one constant water flow rate $\dot{V} = 0.35$ l/min is taken into account in Figure 4.11 and 4.12. Figure 4.11 illustrates the primary spray results, Figure 4.12 shows on the contrary the results for the secondary spray. In both figures there is a well-defined difference between v and w but again z_d has not influence on the results. According to Figure 4.6 and to previous calculations, the transverse velocity w_{prim} and w_{sec} can

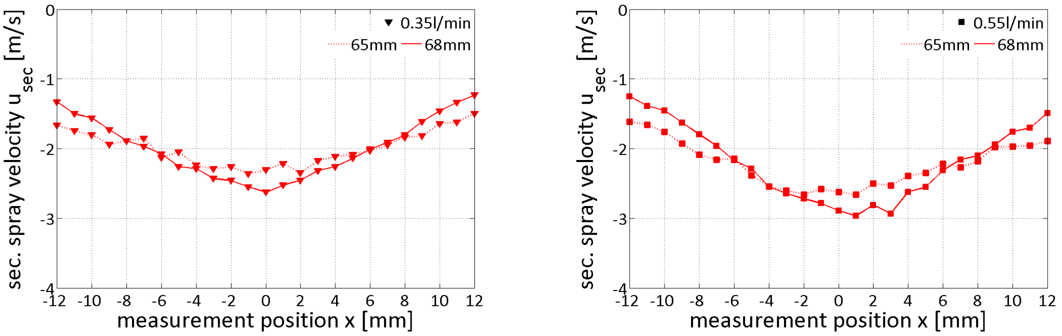

Figure 4.10: Axial velocity u_{sec} of the secondary spray after impacting onto the target along one measurement axis ($\alpha = 0°$) for a water flow rate of 0.35 l/min and 0.55 l/min.

be neglected. By focusing on the first transverse velocity component, the curve of v_{prim} and v_{sec} is point symmetric in the origin. However, the transverse velocity of the impacting drops v_{prim} is lower than the one of the secondary spray v_{sec}.

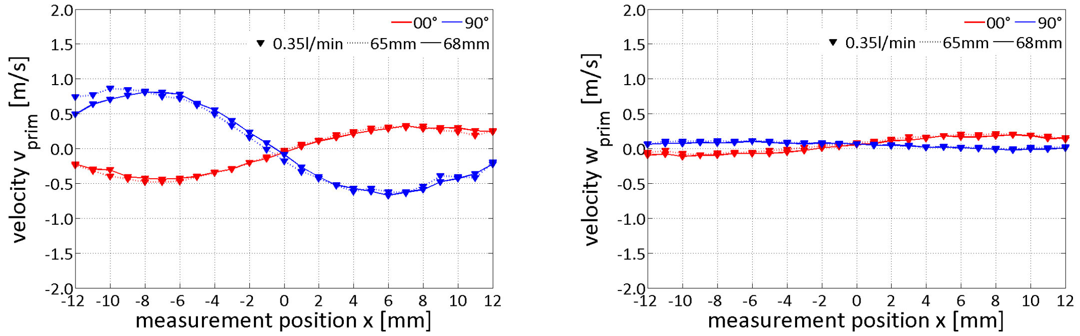

Figure 4.11: Transverse velocities v_{prim} and w_{prim} of the primary spray when impacting onto the target along two measurement axis ($\alpha = 0°$ and $90°$) for $\dot{V} = 0.35$ l/min.

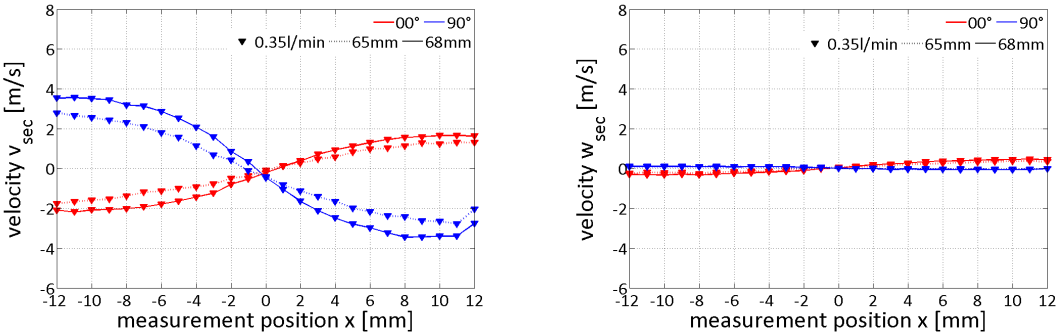

Figure 4.12: Transverse velocities v_{sec} and w_{sec} of the secondary spray after impacting onto the target along two measurement axis ($\alpha = 0°$ and $90°$) for a constant water flow rate of 0.35 l/min.

Hence, the primary spray impact is dominated by the axial velocity shown in Figure 4.9, more than by its transverse velocity components (see Figure 4.11). By comparison, the secondary spray is not influenced by u_{sec} (see Figure 4.10, left) and w_{sec} (Figure 4.12, right). These characteristics become more obvious when we take a look at the high-speed images in Section 4.2.

4.1.4 Spray characterization in the presence of a heated target

For the third experimental case where the target is heated, measurements were performed for only $z_d = 68$ mm. Figure 4.13 represents the results for the mean diameter and the Sauter mean diameter at a constant water flow rate of 0.45 l/min but for various heating powers. The experimental reference case (no heating) of spray impact onto a target is given for comparison with a heated configuration where the target is heated with various powers of 104 W, 202 W and 260 W. Those measurements are performed along one measurement axis with $\alpha = 0°$. According to Figure 4.13, the heating is not affecting the results for D_{10} and D_{32}.

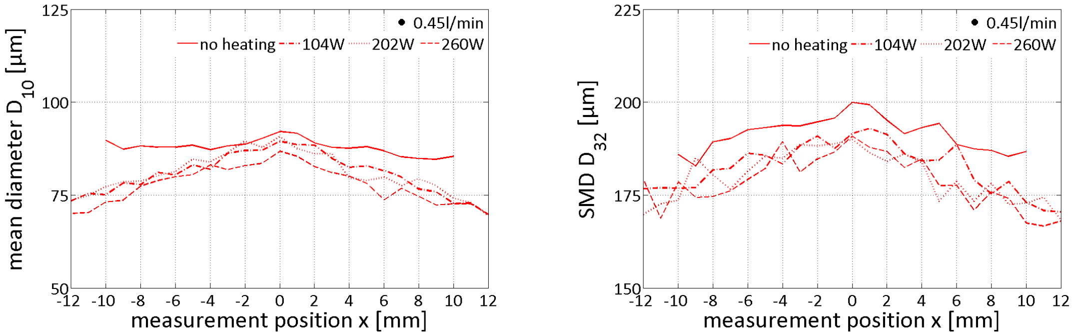

Figure 4.13: Comparison of the mean diameter D_{10} and the Sauter mean diameter D_{32} for the reference case (no heating) and when spray impacts onto a heated target with various heating powers: 104 W, 202 W and 260 W along one measurement axis ($\alpha = 0°$) for $\dot{V} = 0.45$ l/min.

When comparing the results regarding u and v for the primary and secondary spray at different heating, we notice no significant influence of the heating power as demonstrated in Figures 4.14 and 4.15 except for a marginal variation of the impacting spray velocity u_{prim} in Figure 4.14. The curve progressions remain similar to the ones of previously shown figures. The distribution of primary and secondary spray velocity is almost symmetrically.

To sum up, we have used the phase Doppler technique to measure spray at a matrix

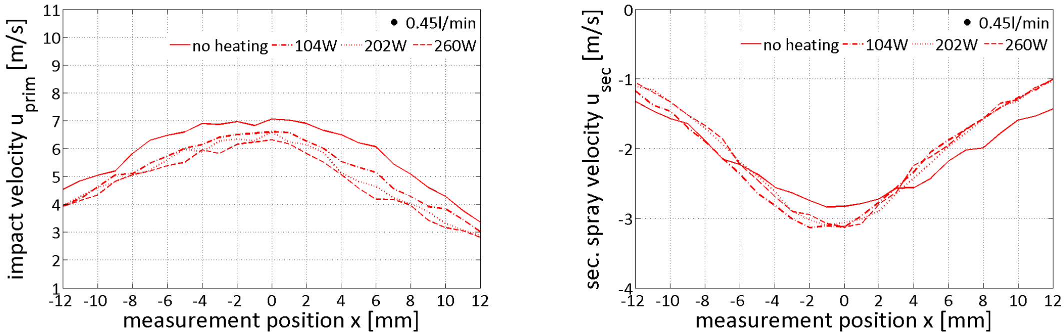

Figure 4.14: Comparison of the axial velocities u_{prim} and u_{sec} for the reference case (no heating) and when spray impacts onto a heated target with various powers: 104 W, 202 W and 260 W along one measurement axis ($\alpha = 0°$) for a constant water flow rate of 0.45 l/min.

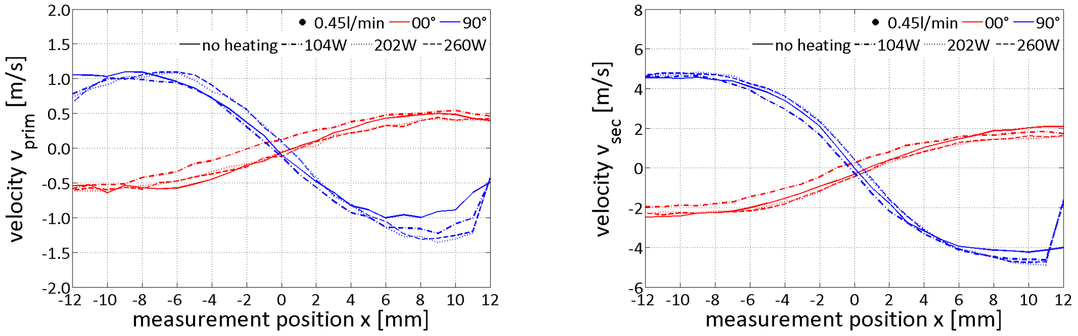

Figure 4.15: Comparison of the transverse velocity v_{prim} and v_{sec} for the reference case (no heating) and when spray impacts onto a heated target with various powers: 104 W, 202 W and 260 W along one measurement axis ($\alpha = 0°$) for a constant water flow rate of 0.45 l/min.

of positions and at each position we receive for several thousand single drops resulting data for their velocity as well as for their diameter. The investigations for the spray without impact onto the target have proven a uniformity of the spray when considering different measurement planes. Further studies with spray impacting onto a target, with and without heating, have yielded similar results for all velocity components. Since the phase Doppler instrument only takes into account spherical and rather small droplets, additional analyses for the spray characteristics are needed.

4.2 Shadowgraphy method

Due to the complexity of spray impact and the liquid film hydrodynamics phenomena, a robust image processing algorithm for shadowgraphy is needed for further evaluation. There is no alternative in performing this type of analysis manually since it would take enormous time to reach satisfactory results. Hence, to overcome this difficulty, a routine software code has been programmed.

4.2.1 Development of a robust drop detection method

A new image processing technique for extracting information such as primary and secondary drops as well as defining their size in the form of diameter and velocities is introduced. Phase Doppler is preferable to characterize small spherical drops while the shadowgraphy method is applicable to relatively large, visible and non-spherical drops. In addition, this robust method allows interpretation of the data gained under various gravity conditions. Under these extreme conditions measurement techniques as for example the phase Doppler instrument can not be applied. The high-speed image analysis is performed in three main steps: image conditioning, particles detection and size as well as velocity information. Basically, in the beginning of the image processing procedure, the equivalent commands are implemented according to the shadow principles described in detail in Chapter 5.2. In order to improve the detection, we need to continue with a clearer picture. The image background is equalized, the noise is removed from the background. Therefore, the background is more uniform and the probability of detecting false objects is reduced. The detection is based on an advanced edge detection filter. These 2D filters, combined with a user selectable detection threshold and a gray scale gradient analysis allows discarding non focused images that might be misinterpreted. The threshold level is a main parameter that helps define the contours of the drops on the images. This parameter expresses the threshold level [%] of the maximum gray level of the image. The higher this value is, the easier it becomes to identify large drops. Figure 4.16 illustrated the results after having selected a particle on one image in two windows: the first window displays the particle contour with statistical information, e.g. regarding its area and equivalent diameter, the second represents gray level characteristics as a function of position along the minima and maxima lines, including particle pixel depth and edge gradients. The edge height validation is the acceptance of particles whose edge as a proportion of total image resolution satisfies a user defined value. In many situations the visibility of drops is limited, either due to scattering of the medium or poor light access. In these cases, the edge height is limited.

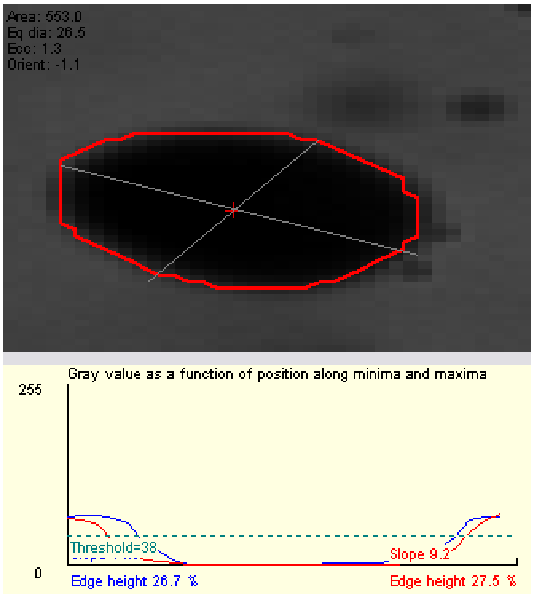
Area: 553.0
Eq dia: 26.5
Ecc: 1.3
Orient: -1.1

Figure 4.16: Particle selection and contour (above window) and threshold level definition according to gray level characteristics along the minima and maxima lines (below window) (Dantec Dynamics software Shadow Sizer Processing).

Once the particles are identified in all images after calibration, the size is simply extracted by counting the number of pixels within the detected object and converted into size information by using a conversion factor measured from a calibration image with a known object size. Figure 4.17 illustrates a series of three images captured at a constant water flow rate and gravity level at different time steps. In this sequence, specific drops can be followed from one image to the other, and new ones that are fully appearing in an image can be anew detected. These images are already analyzed with the shadow processing tool and indispensable for further velocity evaluation. Consequently, the drop detection processing is a prerequisite for the velocity analysis. The velocity computation is based on a Particle Tracking Velocity algorithm. In order to define the velocity of one single drop, its movement within a minimum of two images is required. Using double frame images, the velocity is calculated by dividing pixel displacement by time difference between two successive image frames. The gravity centre of the detected objects is taken as reference for the displacement. In Figure 4.17 many drops can be observed that move from a certain position in the initial image (t1 = 0) to another in the second (t2 = 62.5 μs) or the third image (t3 = 125 μs). In case of double frame images with different intensity, the software allows to compensate this difference to be able to use the same detection threshold.

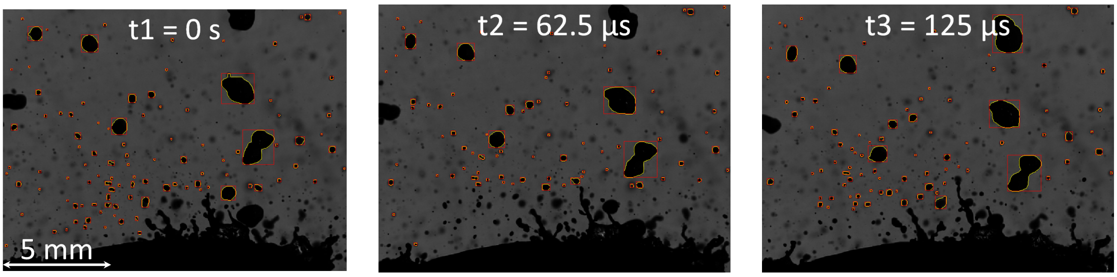

Figure 4.17: Drop detection sequence for the same parameter set that is necessary for velocity determination.

The image analysis has been performed with two different software tools: a) program with customized MATLAB routines and b) customized Dantec Dynamics Shadow Sizer Processing, both based on the same principle.

Resulting images after being processed with both softwares are exemplified in Figure 4.18. The velocities are defined as follows: axial velocity u and transverse velocity v of the impacting and secondary sprays keeping in mind that the impacting spray velocity value in the positive hypergravity case is always positive, the one for the negative hypergravity case negative (compare Figure 3.18). It seems that the impacting drops move mostly normal to the target, whereas the secondary droplets move at various angles.

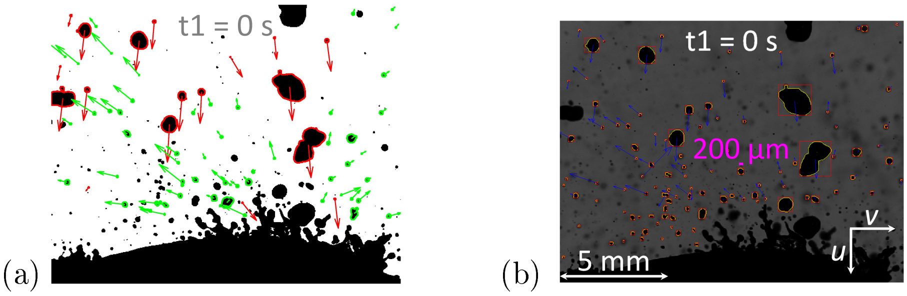

Figure 4.18: Spray detection (size and velocity) with both image processing tools: (a) self-programmed with MATLAB and (b) customized by Dantec Dynamics.

At first sight, it is obvious that not only spherical drops are detected with the image processing method. When we reminisce about the results with the phase Doppler technique shown in Section 4.1, we see that in comparison to the diameters in Figure 4.8, there are definitely drops with a size greater than 200 μm detected in Figure 4.18. When comparing the spray diagnostic results between the phase Doppler measurements and the image analysis at ground conditions and for constant water flow rates, then the values vary significantly. The following calculations illustrate how many almost spherical drops are detected in high-speed images. We proceed in analyzing the spray characteristics that is to say the relation of the drop contour length to the surface area. First, we approach one drop with the contour of an ellipse, see Figure 4.19.

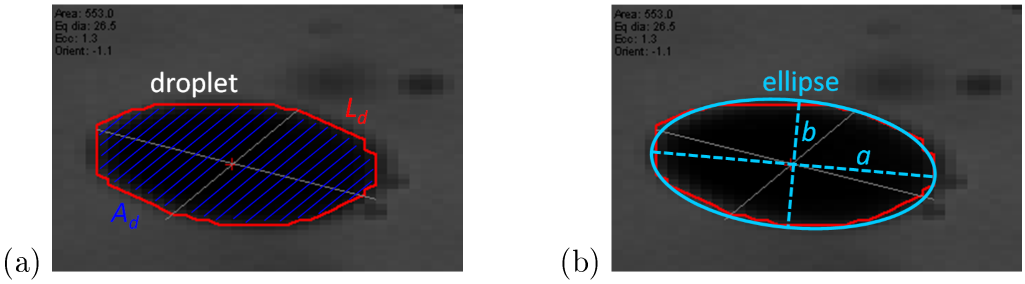

(a) (b)

Figure 4.19: Drop detection analysis: (a) determination of the contour length L_d and the surface area A_d and (b) convergence of the drop surface to an ellipse shape with major and minor axes a and b.

The area A_d enclosed by an ellipse is πab, where a and b are one-half of the ellipse's major and minor axes respectively. The perimeter L_d that surrounds this area can be defined in approximation as

$$L_d = 2\pi\sqrt{\frac{a^2+b^2}{2}} \tag{4.1}$$

With the determination of the substitution ξ as

$$\xi = \frac{a}{b} \quad \text{and} \quad A_d = \pi ab \tag{4.2}$$

we can define

$$A_d = \pi b^2 \xi \quad \text{and} \quad L_d = 2\pi b\sqrt{\frac{1+\xi^2}{2}}. \tag{4.3}$$

Hence, the resulting relation of the perimeter to the surface area is given by

$$\frac{L_d^2}{A_d} = 2\pi\left(\frac{1+\xi^2}{\xi}\right) \quad \text{since} \quad L_d^2 = 2\pi^2 b^2\left(1+\xi^2\right). \tag{4.4}$$

There are finally two solutions for ξ with

$$\xi_1 = \frac{L_d^2}{4\pi A_d} + \sqrt{\left[\frac{L_d^2}{4\pi A_d}\right]^2 - 1} \quad \text{and} \quad \xi_2 = \frac{L_d^2}{4\pi A_d} - \sqrt{\left[\frac{L_d^2}{4\pi A_d}\right]^2 - 1}. \tag{4.5}$$

The drop is ideally spherical for the case $\xi_{1,2} = 1$ meaning that $a = b$. Figure 4.20 illustrates the example image at 2g and 0.25 l/min with the detection of all drops. In addition, the quality of the drop contour is determined with ξ_1. The adequate image processing tool includes several distinct filters according to the drop contour quality (blue, best case: $\xi_1 = 1$, yellow, worst case: $\xi_1 = 3$, see Figure 4.20). Moreover, the red arrows stand for primary spray ($+u$) and the green ones for secondary spray ($-u$) *i.e.* drops after impacting onto the target.

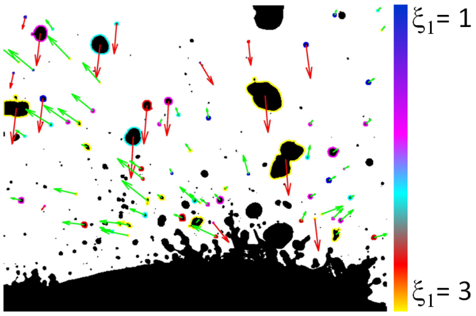

Figure 4.20: Drop contour quality differentiation for 2g, 0.25 l/min with spherical drops when $\xi = 1$ and distinction between primary (red arrows) and secondary spray (green arrows).

With the help of Equation (4.5) suitable diagrams for the above parameter set represent in Figure 4.21 not only the quality of the drop contour but also the quantity of spherical drops detected in this example image. The equivalent diameter D_{equ} is determined as the diameter of a spherical particle having the same surface as the measured object (area A_d, see Figure 4.19). This definition is also illustrated later on in Figure 4.23. As indicated in the histogram in Figure 4.21, most of the detected drops are almost spherical ($\xi_{1,2} = 1$), but there are also numerous ones that are noncircular. The right diagram demonstrates that, especially concerning large drops ($D_{equ} > 1000$ μm), their sphericity is not given whereas smaller drops at a size of $D_{equ} < 800$ μm are existent as spherical as well as irregular.

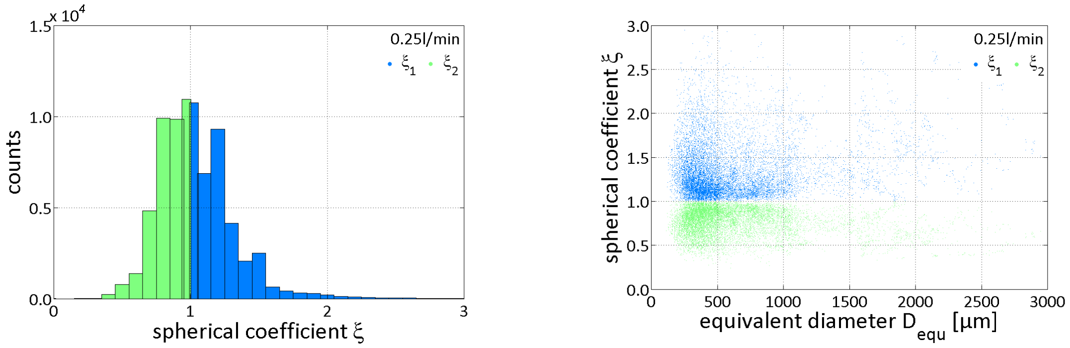

Figure 4.21: Histogram of the spherical coefficient ξ and distribution of two solutions ξ_1 and ξ_2 for $\dot{V} = 0.25$ l/min and 2g with spherical drops defined if $\xi_{1,2} = 1$.

When comparing the results of the spherical coefficient between 2g and 20g for a higher water flow rate of 0.55 l/min, then we can see in Figure 4.22 no significant difference. In both cases, there are many drops detected that are rather elliptic than spherical. In addition, this figure confirms that the drops are smaller at a higher water flow rate and that there are still a multitude of drops represented with non-spherical contour, independent from the gravity level (also at -$\acute{\upsilon}$g).

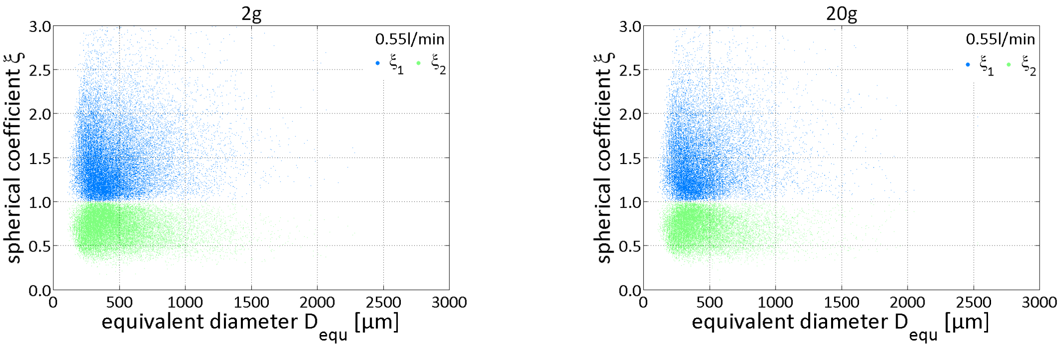

Figure 4.22: Histogram of the spherical coefficient ξ and distribution of two solutions ξ_1 and ξ_2 for a constant $\dot{V} = 0.55$ l/min and at 2g and 20g with spherical drops defined if $\xi_{1,2} = 1$.

Figure 4.23 illustrates the image after being processed with the shadowgraphy tool. The effective diameter (red contour) and the diameter of the equivalent spherical particle (yellow circle) have the same surface as the measured object. The drop is ideally spherical if the contour of the effective diameter match with the optimal spherical diameter D_{opt}. For this case we can define an optimal surface area of a sphere with

$$A_{opt} = \frac{\pi D_{opt}^2}{4} \quad \text{with} \quad \frac{L_d^2}{A_d} = 4\pi \quad \text{and} \quad L_d = \pi D_{opt}. \tag{4.6}$$

It is obvious in Figure 4.23 that most of the drops are not perfectly spherical. Besides, the phase Doppler technique and the image processing method cover different ranges. Hence, the spray characterization only with the phase Doppler technique is not sufficient. Both techniques need to be combined.

The hereby presented robust image processing tool is needed, also for further hydrodynamics investigations and only this evaluation leads to good statistics for both drop size and drop velocities. Large drops that have a great mass and need to be considered in our research study, for the characteristic film thickness in Section 5.3 and especially for the modeling approach in Chapter 5.4. In the following, the spray diagnostics is performed by image analysis. Since there are two image processing tools, firstly a comparison of the drop diameter given for its concrete location in a captured high-speed image is illustrated in Figure 4.24 for a constant parameter set (2g, 0.25 l/min). Both

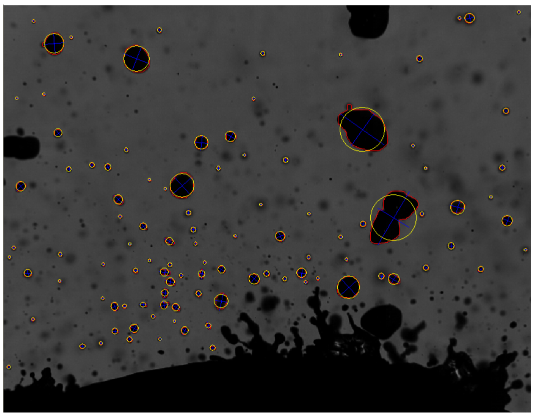

Figure 4.23: Quality of the drop size given by the effective diameter (red contour) and the diameter of the equivalent spherical particle (yellow circle).

tools agree well overall. The largest drops ($\approx$ 1000 μm - 2000 μm) are impacting in the center of the target, at the nozzle axis whereas smaller droplets belong to the secondary spray close to the target (dark blue area).

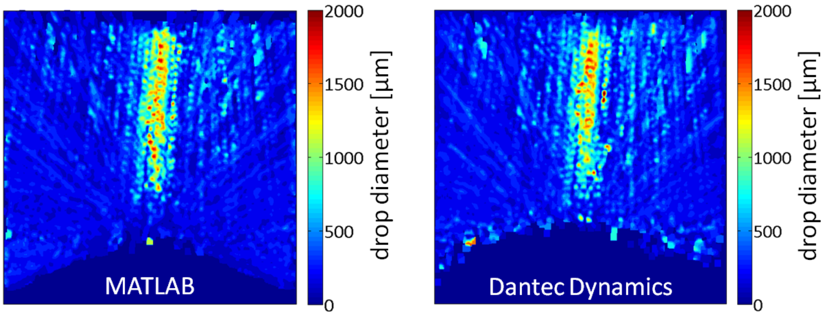

Figure 4.24: Results of the drop diameters belonging to drops passing through a specific position in a high-speed image at 0.25 l/min and 2g. Comparison of the results between two image processing tools: self-programmed with MATLAB and customized by Dantec Dynamics.

Regarding the normalized quantity of detected drops at a certain position, Figure 4.25 shows that most of the drops are passing through positions close to the target ($0.6 < \text{pdf} < 1$). Due to spray impacting onto the target, the secondary spray is stronger represented than the primary spray. In general, the behavior of the spray is symmetric and very similar in both resulting images. Furthermore, the software of Dantec Dynamics seems not to take drops into account that are very close to the target's surface compared to the MATLAB program.

When comparing the results of the Sauter mean diameter in Figure 4.26 for various water flow rates $\dot{V}$ and exemplary for a constant gravity level of 2g and 20g. We receive

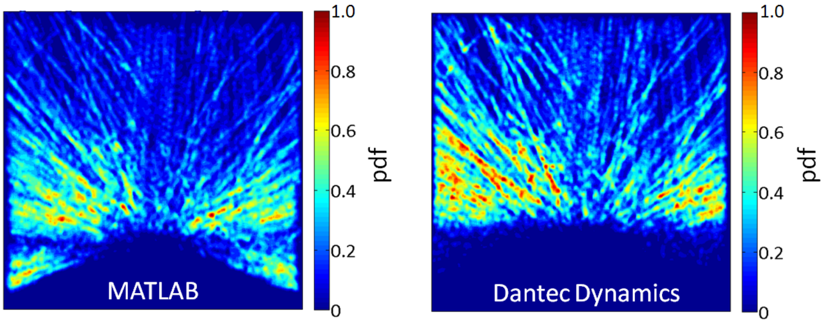

Figure 4.25: Normalized number of detected drops per location in the high-speed image, again for 0.25 l/min, 2g and for the two different image processing tools.

similar results with both tools (self-programmed tool with MATLAB and customized one by Dantec Dynamics). The difference of ≈ 40 μm can be disregarded since 30 μm correspond to about 1 pixel.

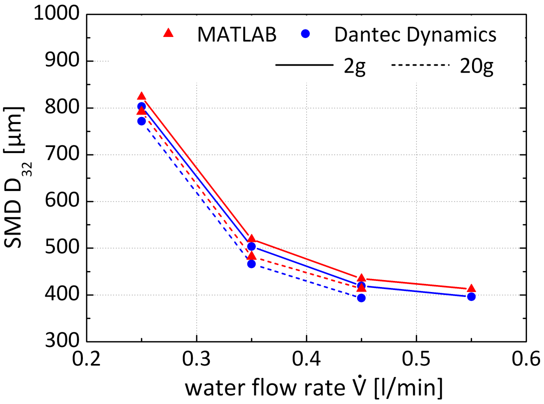

Figure 4.26: Comparison of the Sauter mean diameter results for 2g and 20g between two image processing tools: self-programmed with MATLAB and customized by Dantec Dynamics.

Hence, the evaluation of the high-speed images can be proceeded by focusing on one software tool.

4.2.2 Drop size and velocity distributions under variable gravity levels

The following analysis has been performed with Shadow Sizing by Dantec Dynamics. The question that we are addressing now is if gravity has an effect on the drop diameter and on the velocities u and v of the primary and secondary spray. By taking a look at the normalized distribution of the impact diameter for various +ú-g levels (in Figure 4.27: 2g, 12g and 20g) compared to the reference case on ground (1g), we receive very similar trends according to both water flow rates 0.25 l/min (left) and 0.55 l/min (right).

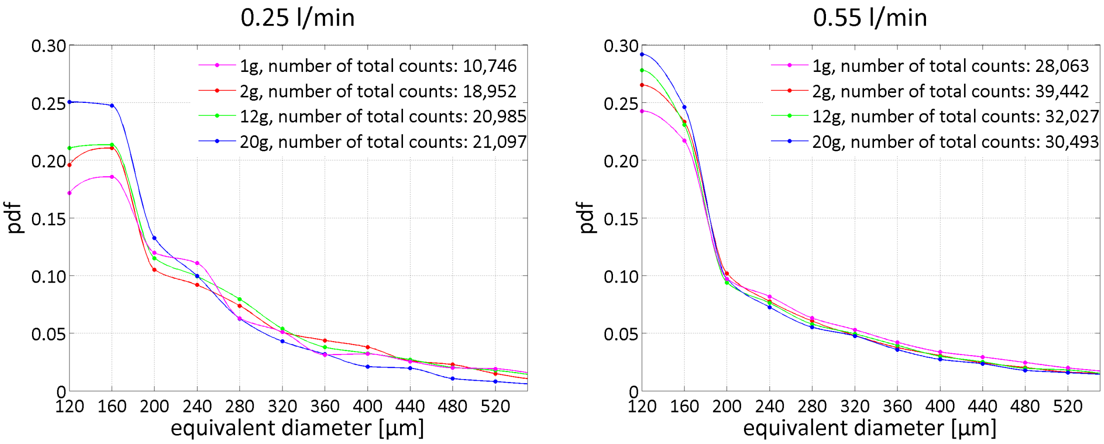

Figure 4.27: Normalized distribution of the drop impact diameter for two different water flow rates (left: 0.25 l/min, right: 0.55 l/min) and at various +ú-g levels (2g, 12g, 20g) compared with the reference case 1g.

The characteristics of the 0.55 l/min-curve are even more in agreement compared to 0.25 l/min. One reason can be that the drop impact diameters always differ stronger at lower water flow rates and are more stable regarding their size with an increase of $\dot{V}$. Besides, the peak of the curves correspond to the same equivalent diameter: $\approx$ 160 μm for 0.25 l/min, $\approx$ 120 μm for 0.55 l/min. The only difference is the normalized number of drops detected at this certain diameter which might be due to the change in velocity. In general, Figure 4.27 also shows that more smaller droplets are detected at the higher water flow rate. Figure 4.28 also confirms similar results for the drop impact velocity u at a higher water flow rate. On the left hand side the normalized u-distribution is compared for various gravity levels 2g, 12g and 20g at a water flow rate of 0.25 l/min.

A shift in the characteristics can be observed signifying that the velocity of the drops impacting onto a target increases with a higher gravity level. The right hand side illustrates the results for 0.55 l/min but in comparison to 0.25 l/min the distribution shift remains almost identical. In general, this figure displays that the drops are impacting onto a target with a greater velocity at an increased water flow rate. In Figure 4.29 all gravity results are plotted in one figure allowing a better comparison with the reference case of 1g.

The previously mentioned shift in the distribution becomes clearer for 0.25 l/min

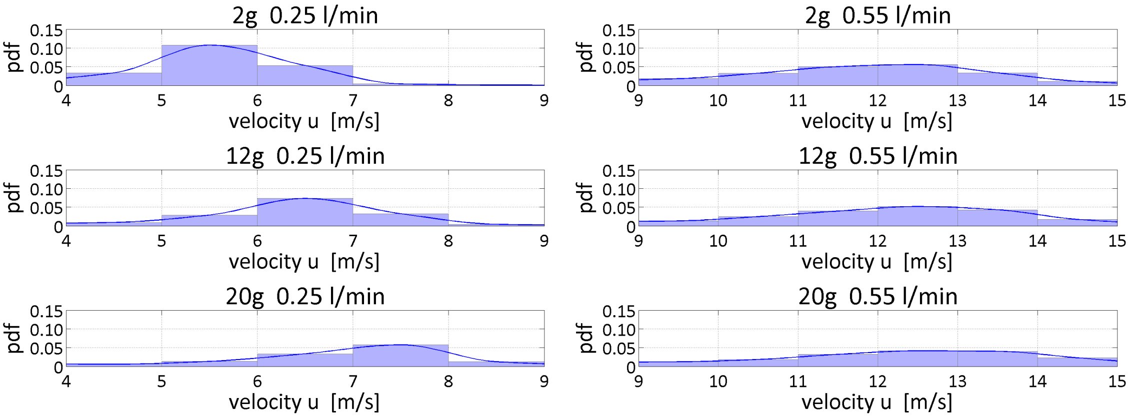

Figure 4.28: Normalized distribution of the drop impact velocity for two different water flow rates (left: 0.25 l/min, right: 0.55 l/min), at various gravity levels (2g, 12g, 20g).

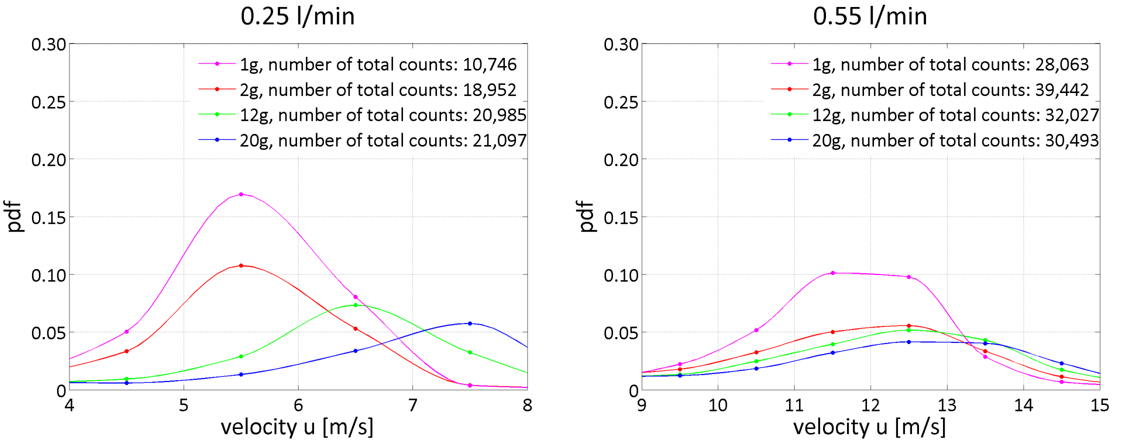

Figure 4.29: Comparison of the normalized distribution of the drop impact velocity between various $+\acute{\upsilon}$g levels (2g, 12g, 20g) and ground conditions (1g) for two different water flow rates (left: 0.25 l/min, right: 0.55 l/min).

since the peak is displaced from ≈ 5.5 m/s (1g) to ≈ 7.5 m/s (20g). Regarding $\dot{V}$ = 0.55 l/min (also in Figure 4.29), the difference to the ground condition is not that significant. The devolution of the peak is smoother ranging from ≈ 12 m/s (1g) to only ≈ 13.5 m/s (20g). Hence, the gravitational force affects much stronger the drop velocities than their sizes. Results for the transverse velocity v and for the same parameter case as previously mentioned are given in Figure 4.30. This time, for both distributions, gravity seems not to influence the results. The secondary and primary drops have a balanced behavior in their transverse velocity in all settings.

In a direct comparison with the 1g results in Figure 4.31, the transverse velocity v is not changing, independent from the water flow rate (left: 0.25 l/min, right: 0.55 l/min). Therefore, we can state that gravity plays a rather irrelevant role for the transverse

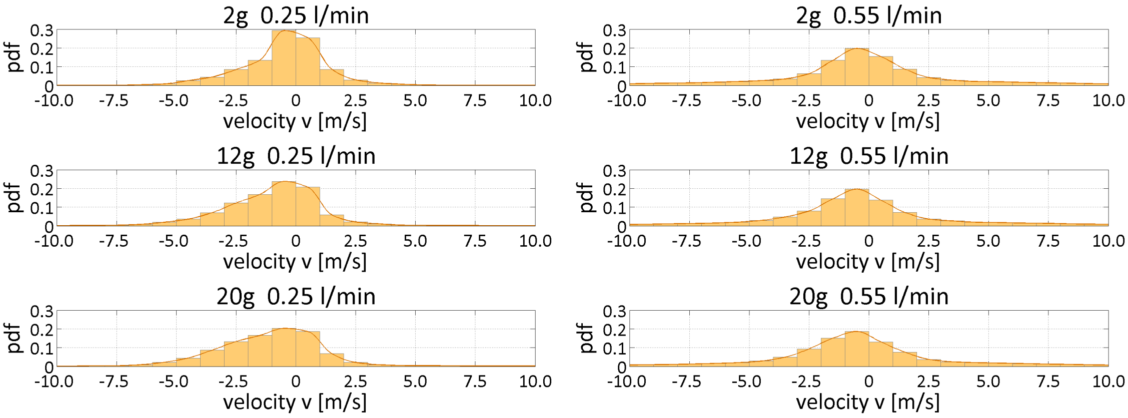

Figure 4.30: Normalized distribution of the transverse velocity v for two different water flow rates (left: 0.25 l/min, right: 0.55 l/min) and at various gravity levels (2g, 12g, 20g).

velocity v compared to the axial velocity u.

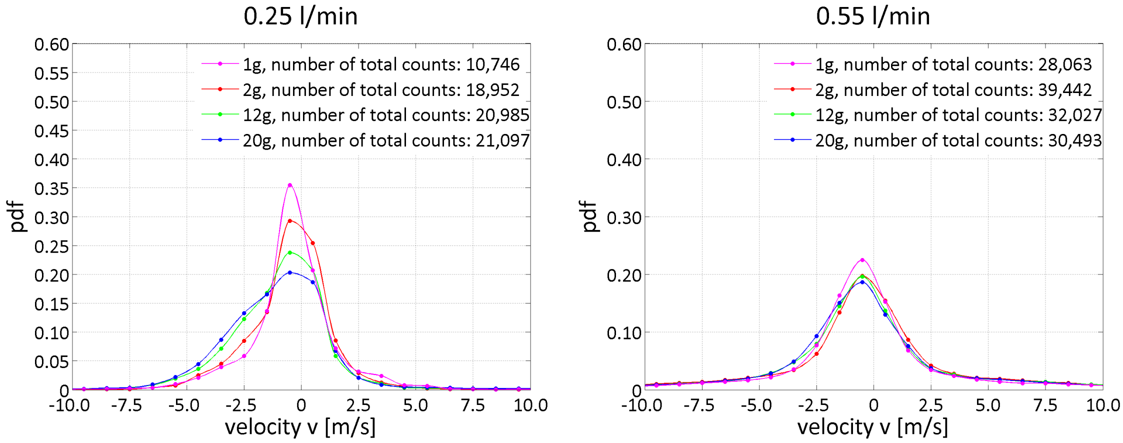

Figure 4.31: Normalized distribution of the transverse velocity v for the reference case 1g compared to 2g, 12g and 20g. Given results for two different water flow rates (left: 0.25 l/min, right: 0.55 l/min).

Analogous diagrams are presented in Figures 4.32 and 4.33 for the negative hypergravity situation where spray impacts against gravity force onto the target (see Figure 3.18). At 0.25 l/min gravity has a stronger influence on the distribution of the impacting drops whereas at 0.55 l/min the results are very similar.

Regarding the two velocity components' distribution, we are only considering the results for the greater water flow rate. As in the positive positive hypergravity case, the results are not significantly affected by the gravitational force. The findings for lower water flow rates are as disordered as in Figure 4.32 (left). Further observations,

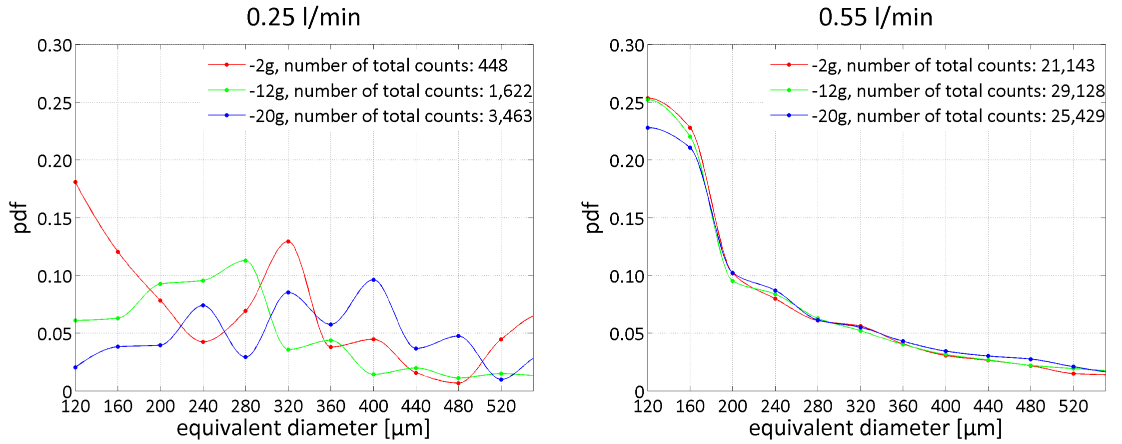

Figure 4.32: Normalized distribution of the drop impact diameter for two different water flow rates (left: 0.25 l/min, right: 0.55 l/min) and at various negative hypergravity levels (-2g, -12g, -20g).

especially on spray modes at lower water flow rate under negative hypergravity, are performed in Section 5.1.

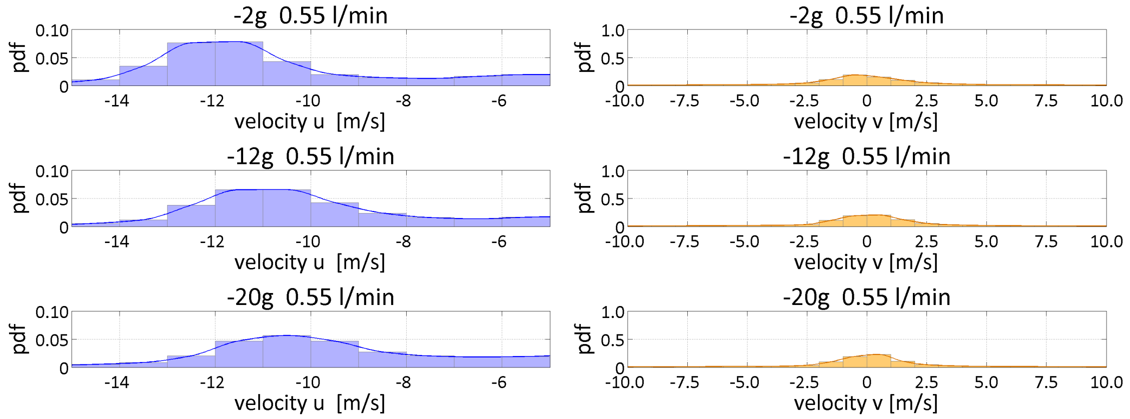

Figure 4.33: Normalized distribution of the impact velocity u and the transverse velocity v for $\dot{V} = 0.55$ l/min and at various negative hypergravity levels (-2g, -12g, -20g).

A direct correlation between the velocity and the drop size of the impacting and of the secondary spray is presented in Figure 4.34 for a constant water flow rate of 0.25 l/min but for various gravity levels 1g, 2g, 12g and 20g. The primary spray is defined by the region of $u > 0$ whereas all the points with negative u velocity (appointed by $u < 0$) correspond to secondary spray. The average u velocity of the primary drops decreases with the drop diameter. The same tendency appears for the secondary drops. In addition, a cloud of relatively small droplets with $D < 750$ μm moving towards the wall with relatively high velocities can be recognized.

The results of the primary spray correspond to the ones in Figure 4.27 and in Figure 4.28. The equivalent diameter does not differ strongly whereas the drop impact velocity is higher at 20g than at the reference case 1g, 2g and 12g.

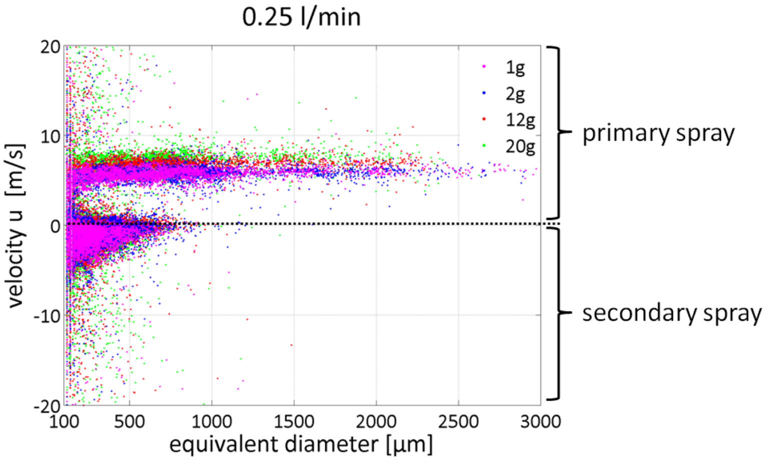

Figure 4.34: Correlation between the impact velocity and the drop impact diameter for a constant water flow rate ($\dot{V} = 0.25$ l/min) but at various gravity levels: 1g, 2g, 12g and 20g.

For the case of constant gravity levels (left: 2g, right: 20g) but for various water flow rates, Figure 4.35 clarifies the behavior of the drop size - velocity correlation. It is noticeable that the impact velocity increases with an increase of the water flow rate for both gravity cases if we follow from the blue highlighted points (0.25 l/min) to the yellow ones (0.55 l/min). In addition, the drop size decreases at a greater water flow rate. Both tendencies are confirmed in the previous phase Doppler measurements and are illustrated in Figure 4.5 and 4.8.

For the analogous parameter set, Figure 4.36 illustrates the transverse velocity correlating to the equivalent diameter for constant gravity levels and different water flow rates.

Basically, there is no clear difference in these results (Figure 4.36) as previously shown in Figure 4.6. In addition, the characteristics of u are equalized. At negative gravity condition, the spray behaves different, see Figure 4.37. On the contrary to positive hypergravity (see Figure 4.35), there is almost no secondary spray at low water flow rate (for the -$\acute{v}$g case defined as $+u$). The tendency of an impact velocity increase at higher water flow rates is again present on the left hand side of Figure 4.37. This trend is not affected whether the measurements are performed at positive or negative hypergravity.

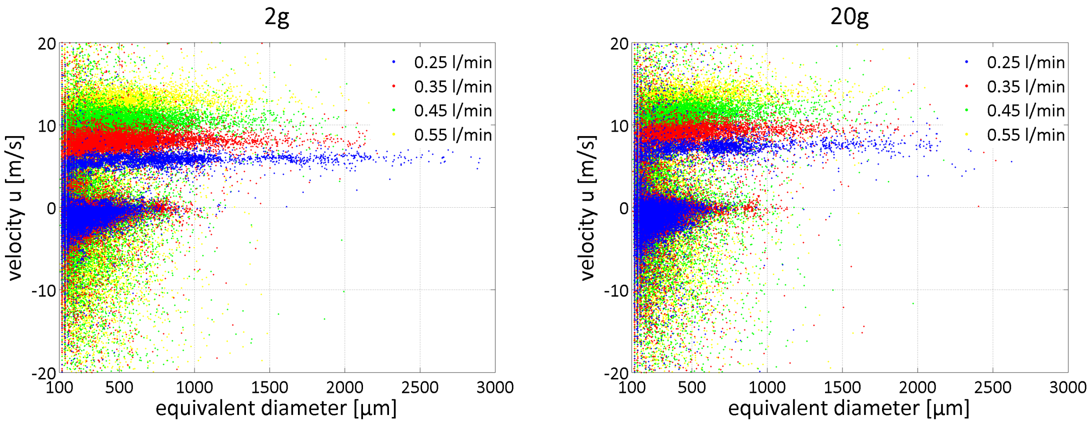

Figure 4.35: Correlation between the impact velocity and the drop diameter for various water flow rates up to 0.55 l/min at a constant gravity level (left: 2g, right: 20g); positive area: primary spray, negative one: secondary spray.

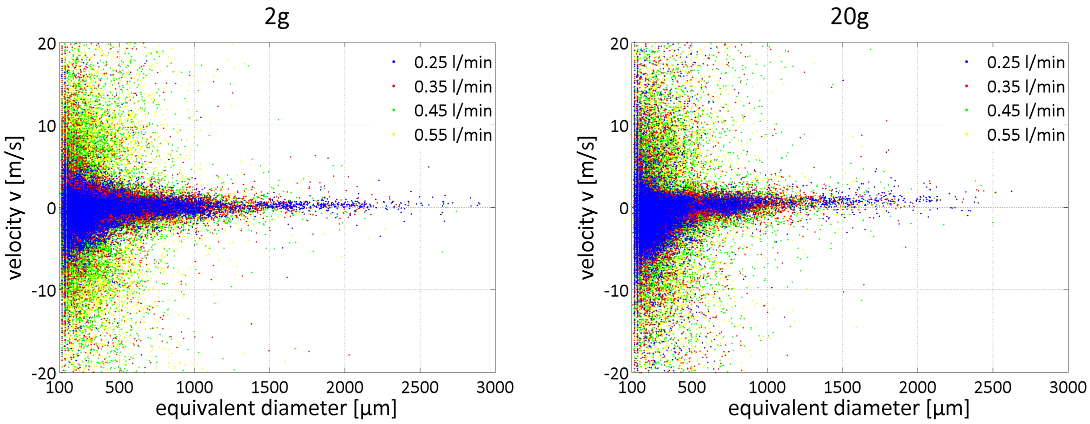

Figure 4.36: Correlation between the transverse velocity and the drop impact diameter for various water flow rates up to 0.55 l/min at a constant gravity level (left: 2g, right: 20g.

When focusing now on the results for the transverse velocity (Figure 4.37, right) the outcome is again symmetric with the difference that the band of v is much smaller for lower water flow rates. In Figure 4.36 the range of results is expanded. At 0.25 l/min the spray is mostly dominated by its axial velocity component. The transverse velocity is maximal 1 m/s for 0.25 l/min and about up to 3 m/s for 0.35 l/min. Only at higher water flow rates the transverse velocity component is emphasized (yellow and green data points).

The next figures display the direct correlation between the two velocity components u and v at a constant water flow rate. The results for 0.25 l/min are shown in Figure 4.38, the ones for 0.55 l/min in Figure 4.39. Positive u stands for the impacting spray,

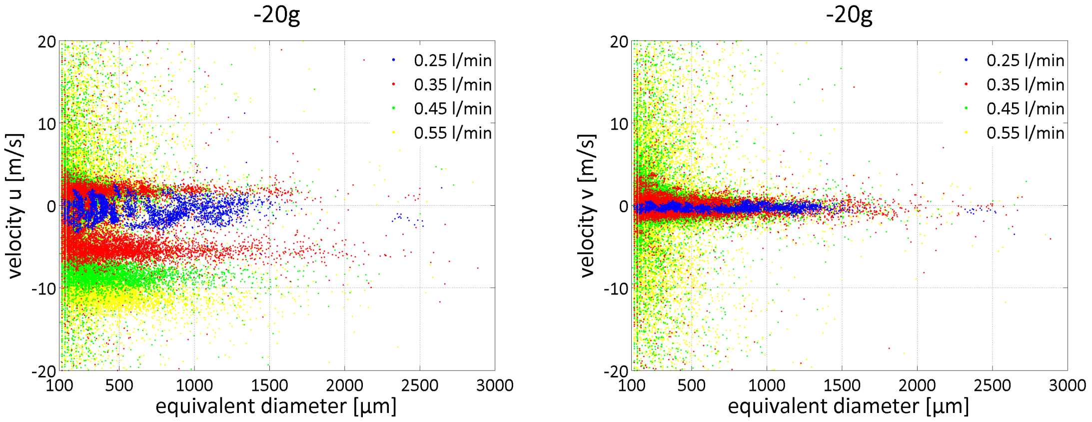

Figure 4.37: Correlation between the impact velocity u (left)/ the transverse velocity v (right) and the drop impact diameter for various water flow rates up to 0.55 l/min at a constant gravity level -20g.

negative u signifies the secondary spray. The color of the data points corresponds to the size of the equivalent diameter. In both cases, the u/v-correlations are compared directly between 2g and 20g and seem similar at first sight. All large drop diameters (highlighted in red) belong obviously to the primary spray and form a very homogeneous round data field. The data point location for the secondary spray is clearly more distributed, especially for higher water flow rates. Note that for all cases the correlation is almost symmetrical.

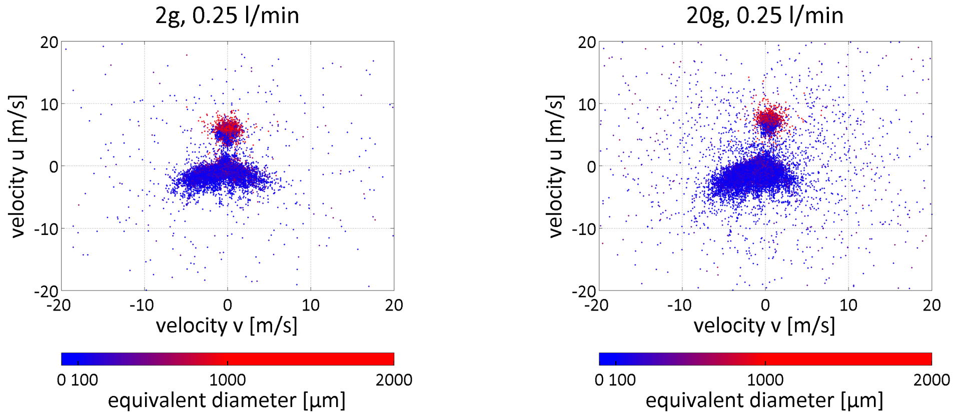

Figure 4.38: Correlation between the two velocity components u and v at a constant water flow rate of 0.25 l/min. Comparison of the results for two different gravity levels 2g (left) and 20g (right).

The results presented in Figures 4.34 - 4.39 agree very well with the Phase Doppler measurements in the work of Roisman et al. (2006). In Roisman et al. (2006) the spray is also impacting onto a metal, spherical target (93 mm in diameter) and is

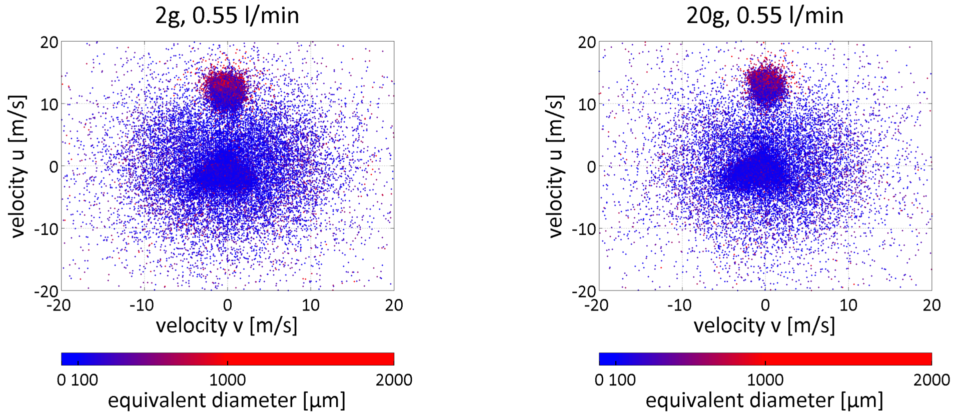

Figure 4.39: Correlation between the two velocity components u and v at a constant water flow rate of 0.55 l/min. Comparison of the results for two different gravity levels 2g (left) and 20g (right).

characterized 1 mm above the north pole with a drop diameter D and two velocity components u_X ($\hat{=}$ u) and u_Y ($\hat{=}$ v). Equivalent to our analysis, it is distinguished due to the sign of the normal-to-the-wall velocity u_X between primary drops before wall interaction when $u_X > 0$ and secondary droplets when $u_X < 0$. In Figure 4.40, a sample correlation of D and u_X as well as u_X and u_Y is given for one experimental condition for the spray directed normal to the sphere. The behavior of the here investigated spray is typical for decelerating sprays since the average velocity of the primary drops increases with the drop diameter (see (a)). As in our analysis, a cloud of droplets is formed. But in this case, they are relatively small ($D < 40$ μm) and move towards the wall with relatively high velocities, comparable with the velocity of the primary spray. According to Roisman et al. (2006), this effect can be explained by the fact that some small drops are accelerated by an air flow induced by the fast and large neighboring primary drops.

In comparison to the $+\acute{v}$g results, the ones for the negative experimental configuration vary significantly. Firstly, the lower data rate attracts attention in Figure 4.41 at 0.25 l/min, for both gravity levels, 2g and 20g. At this point, it needs to be mentioned that this parameter combination leads to exceptional spray hydrodynamics later on illustrated in Section 5.1 with high-speed images. Regarding the spray behavior at 20g, the red highlighted data points may be misinterpreted such that there are not only large impacting drops but also secondary ones. Quite the contrary, the detected drops of the primary and secondary spray shown in this diagram are identical ones since they do not reach the target due to gravitational force. Consequently, a positive axial velocity is taken into account for those large drops previously accounted as negative

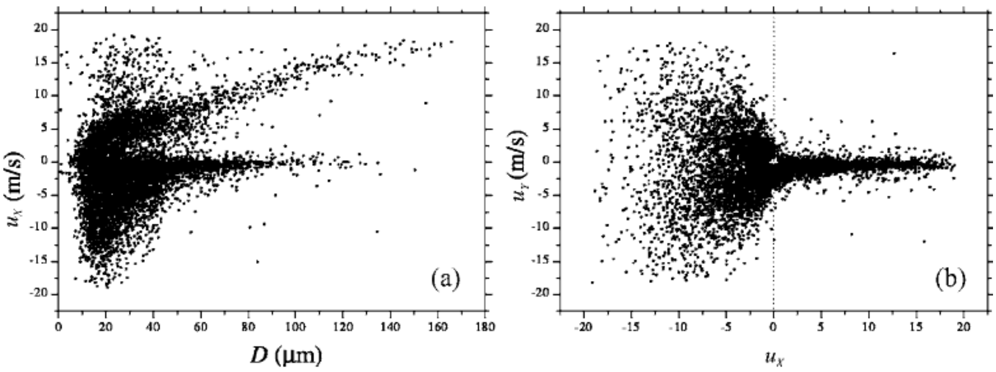

Figure 4.40: Normal impact onto a spherical target. Scatter diagram (a) [D,u_X] and (b) [u_X,u_Y]. Each point corresponds to the detected and validated drop (reprint from Roisman et al. (2006)).

values.

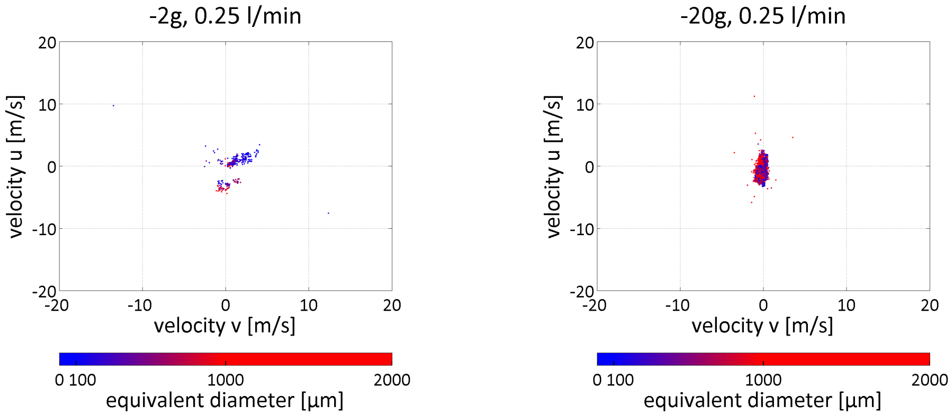

Figure 4.41: Correlation between the two velocity components u and v at a constant water flow rate of 0.25 l/min. Comparison of the results for two different negative gravity levels -2g (left) and -20g (right).

In analogy, the evaluation for a higher water flow rate of 0.55 l/min is given in Figure 4.42. Remarkably more drops are detected at this flow rate. The characteristics resemble the ones in Figure 4.39 after mirroring on the axis of axial velocity component v. But in comparison to those previous results at $+\acute{v}$g, the u/v-distribution in Figure 4.42 disaccord between -2g and -20g. Further observational studies are needed to understand the hydrodynamics for this case, they are performed in Section 5.1.

When finally comparing the results under normal gravity condition (1g) and for a constant water flow rate of 0.25 l/min between measurements with a target and measurements without a target, then we receive very similar results. It has no meaningful effect on the drop size and drop velocity of the impacting spray if measurements are per-

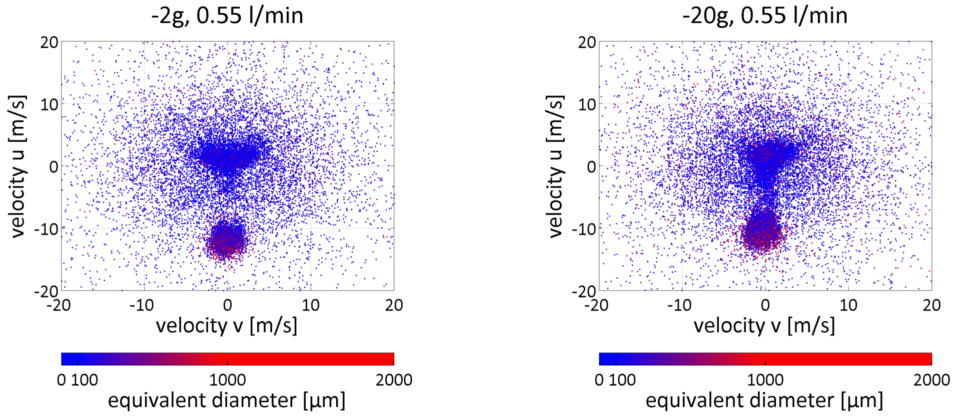

Figure 4.42: Correlation between the two velocity components u and v at a constant water flow rate of 0.55 l/min. Comparison of the results for two different negative gravity levels -2g (left) and -20g (right).

formed with or without a target. Hence, the high-speed image experiments performed without target do not need to be further analyzed.

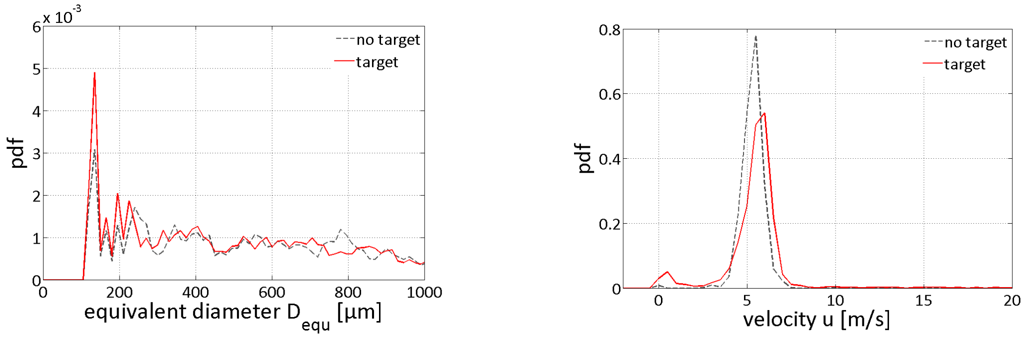

Figure 4.43: Drop velocity and size distribution at ground conditions for a constant water flow rate of 0.25 l/min. Comparison of the measurements with and without the target.

4.2.3 Secondary drop diameters

In order to filter out the major physical effects for the most effective modeling strategies further studies focusing on the parameters as a function of flow rate and gravity need to be performed.

In Figure 4.44 the distribution of (a) the mass ratio $\dot{m}_{sp}$ and (b) secondary to primary droplet size ratio D_{sp} is plotted. Both factors are considering the Sauter mean diameters (indicated in the following with D) and are defined as

$$\dot{m}_{sp} = \frac{\dot{m}_{sec}}{\dot{m}_{prim}} = \frac{\sum D_{sec}^3 u_{sec}}{\sum D_{prim}^3 u_{prim}} \tag{4.7}$$

$$D_{sp} = \frac{D_{sec}}{D_{prim}} \tag{4.8}$$

In Figure 4.44 (a), the ratio of the secondary to the primary mass flow rate is plotted for various gravity levels. In general, when looking at a constant water flow rate, the distributions vary except for the ground condition. For the case of 1g, there is a break-down in all curves.

When analyzing the results for the ratio of the drop size of secondary to primary spray in Figure 4.44 (b), the tendencies become clearer. For negative hypergravity conditions, there is a strong discrepancy of the values for all water flow rates. Some data points are even greater than one with values up to approximately $D_{sp} = 1.6$. Especially at lower water flow rates, $D_{sp} > 1.0$. These values can be explained with the spray-wall interaction morphologies such as drop formation and film jetting only appearing at $-\acute{v}$g (see Table 5.1). In direct comparison, the data points for positive hypergravity are more homogeneous and $D_{sp} < 1.0$ is obtained for all gravity levels. One reason may be that the spray phenomena for $+\acute{v}$g coincide throughout all water flow rates and gravity levels. Especially for a constant water flow rate, the results have similar values. In addition, there is a tendency that D_{sp} increases with a higher water flow rate. At 0.25 l/min the primary drops are significantly larger than the secondary drops whereas at 0.65 l/min, the drop sizes do not strongly differ. Hence, the size of the secondary drops converge the size of the primary drops with an increase of the water flow rate. This insight is important for further analysis accounting D_{sp} as a criterion for the spray-wall interaction.

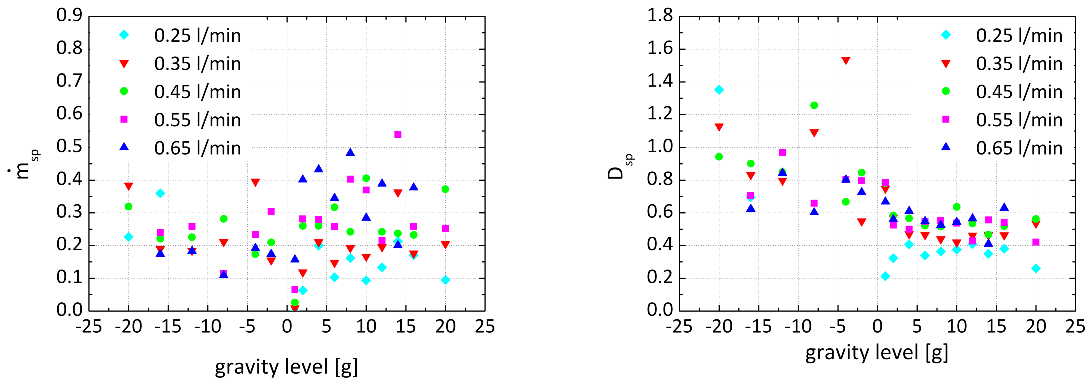

(a) (b)

Figure 4.44: Ratio of the secondary mass flow rate to the primary mass flow rate (a) and secondary to primary drop size ratio (b).

Another way to identify the effect of different factors on the spray impingement phenomenon are groups of dimensionless numbers, such as Reynolds number Re (Equation 2.2), Weber number We (Equation 2.1) and Capillary number Ca (Equation 2.4). In addition, the K-number K defined in Equation 2.5 is introduced as a fundamental dimensionless number for this field (Yarin (2006), Mundo et al. (1998)) and especially for the splash threshold in the work of Roisman et al. (2006) where a crown appears if the inertial effects in the lamella are much larger than the capillary effects.

Figure 4.45 shows the ratio of the average secondary drop diameter to the average primary drop diameter D_{sp} plotted against the K-number K from Equation 2.5. In Figure 4.45 (a), the results for D_{sp} are plotted for -$\acute{v}$g, 1g and +$\acute{v}$g. One can see that for the -$\acute{v}$g case, D_{sp} is smaller than 1.0 at higher water flow rates whereas D_{sp} increases and becomes greater than 1.0 with a decrease of the water flow rate. When considering only the +$\acute{v}$g results included in Figure 4.45 (b), D_{sp} seems almost constant in the range of approximately 0.4 to 0.6, especially for higher water flow rates.

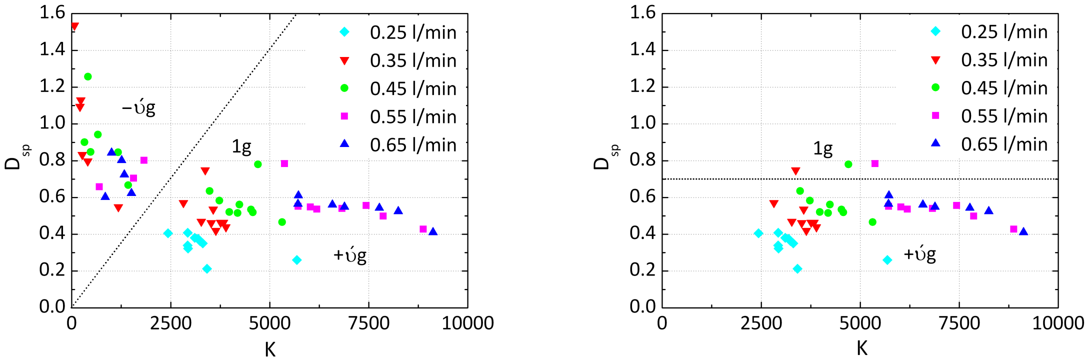

(a) (b)

Figure 4.45: Average secondary to average primary drop diameter ratio D_{sp} plotted against the K-number K for (a) ground, negative (-$\acute{v}$g) and positive hypergravity (+$\acute{v}$g) condition, (b) 1g and +$\acute{v}$g.

The data points for 1g are almost constant at 0.78 and this confirms the analysis in the work of Batarseh (2008) (see Figure 4.46) where $D_{sp} = 0.75$. Note that D_o describes the outgoing droplets and D_i the incoming ones so that $D_o/D_i \mathrel{\hat{=}} D_{sp}$.

Figures 4.47 (a) and (b) illustrate the results for another important relation between primary and secondary drops firstly presented in the work of Roisman et al. (2006). The ratio of the measured average drop diameter D_{sec} of the secondary spray to the characteristic finger radius $\sim D_{prim}\ Re_{prim}^{-1/2}$ is plotted against the Reynolds number of the primary drops Re_{prim} calculated on the basis of the averaged component of the

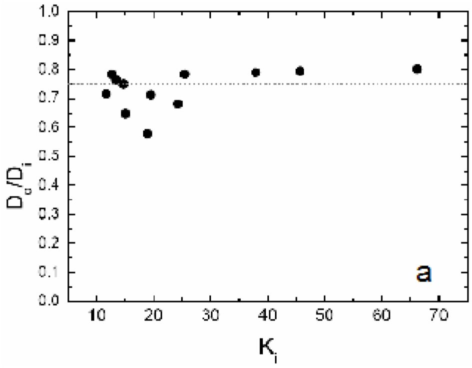

Figure 4.46: Ratio of the outgoing to incoming droplet size D_o/D_i vs. the K number K_i (reprint from Batarseh (2008)).

spray velocity normal to the wall.

$$Re_{prim}^{1/2} D_{sp} = \left(\frac{u D_{prim}}{\nu} \right)^{1/2} \frac{D_{sec}}{D_{prim}} \tag{4.9}$$

At negative hypergravity condition (see -$\acute{v}$g in Figure 4.47 (a)), there is a stronger discrepancy between the model of Roisman et al. (2006) and the results of Batarseh (2008). When disregarding the -$\acute{v}$g results, we receive a rather consistent distribution as displayed in Figure 4.47 (b). At high Reynolds numbers ($Re > 4300$) and for higher water flow rates, there is a constant ratio of approximately 38 at positive hypergravity. In general, the values tend to decrease and confirm the relation $D_{sec} \sim D_{prim} Re_{prim}^{-1/2}$.

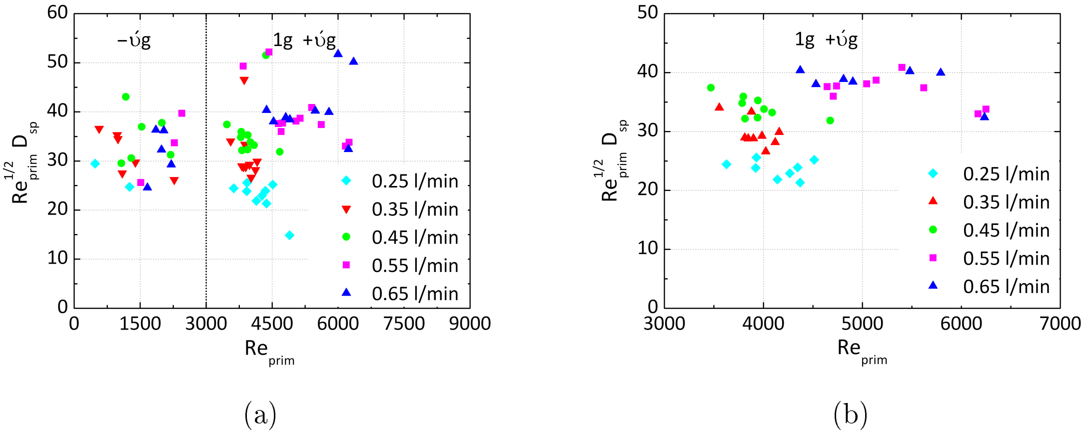

Figure 4.47: Ratio of the secondary to the primary drops scaled by the Reynolds number of the primary droplets Re_{prim} for (a) the entire g-regime and (b) 1g, $+\acute{v}$g.

Hence, the average diameter of secondary drops D_{sec} is finally determined by fitting the data of Figure 4.47 (b) as follows

$$D_{sec} = 38 D_{prim} Re_{prim}^{-1/2} \qquad \text{for } \mathrm{Re}_{prim} > 4300 \tag{4.10}$$

For comparison, the results for normal spray impact onto a rigid wall in Roisman et al. (2006) presented in Figure 4.48 have shown that at high Reynolds numbers ($Re_b > 500$) this relation has a constant value of approximately 24 (note that a = after, b = before impact). In the investigations of Batarseh (2008) performed for the case of spray impact onto inclined flat targets similar results to the normal spray impact were brought for relatively small angles (15° and 30°), which indicates that the mechanism of the secondary spray formation in spray impact onto inclined targets is the similar to normal spray impact.

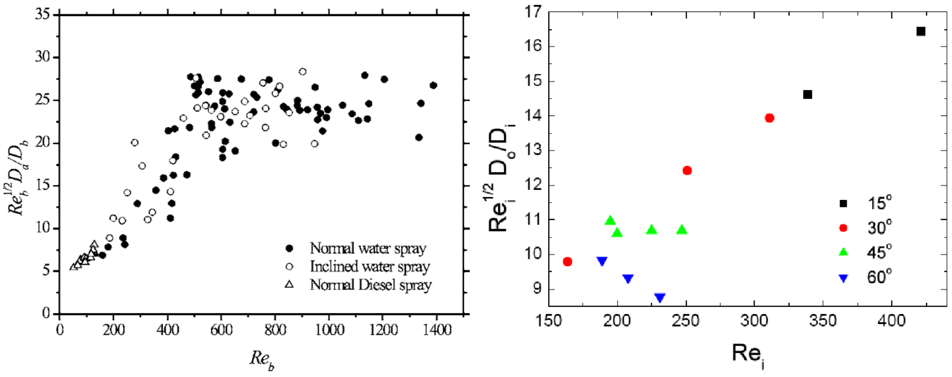

(a) (b)

Figure 4.48: Ratio between (a) the droplets after impact D_a and the droplets before impact D_b (reprint from Roisman et al. (2006)), (b) the outgoing D_o to the ingoing D_i droplets (reprint from Batarseh (2008)) scaled by Re.

Hence, our results show a good agreement with these previous studies and successfully confirm the stability analysis for various gravity levels and various water flow rates in the work of Roisman et al. (2006).

Chapter 5

Liquid film hydrodynamics

In the following, we are focusing on studying the second region of interest that is to say the hydrodynamics of the liquid film (blue highlighted area in Figure 1.1). The hydrodynamics of inertia driven flows on rigid walls is not completely understood and therefore the influence of gravity forces on the outcome of spray impact is not clear. Due to elementary observations, the influence of gravity on the spray impact scenarios and especially on the liquid film hydrodynamics is studied firstly in this chapter. Various modes of spray-wall interaction are then classified and several major elements are identified that are typical of film flows governed by inertia and surface tension.

5.1 Observations

5.1.1 Splash scenarios observed during PFC

In Figure 5.1 a time sequence of high-speed images capturing the spray-wall interaction at microgravity are shown. At first sight, the wall flow created by spray impact onto a target looks rather chaotic. Among the infinite number of configurations which can be observed during spray impact, we have recognized three main scenarios of splash leading to the formation of secondary drops. The first conventional scenario is very similar to the splash produced by a single drop impact onto a stationary uniform liquid film. The rim bounded a free uprising sheet produced by drop impact is unstable, its centerline deflects leading to the cusp formation and emergence of free finger-like jets. These jets are also unstable. Axisymmetric capillary instability leads to their break-up and formation of secondary drops. The second scenario takes place if the impact is not symmetric, for example due to the interaction with other drops or if the local wall film velocity is significant. This asymmetric uprising sheet quickly collapses, the rim bounding this sheet merges leading to the formation of bifurcating jets emerging directly from the wall film. The break-up of these jets then leads to the formation of secondary drops (Roisman et al. (2007)).

The third scenario is observed only under microgravity. Micro-g experiments enable us to expand the length and time scales. At the same time, the underlying physics are sustained. The process of drop impact, creation of the uprising sheet and its propagation take a much longer time than under 1g conditions.

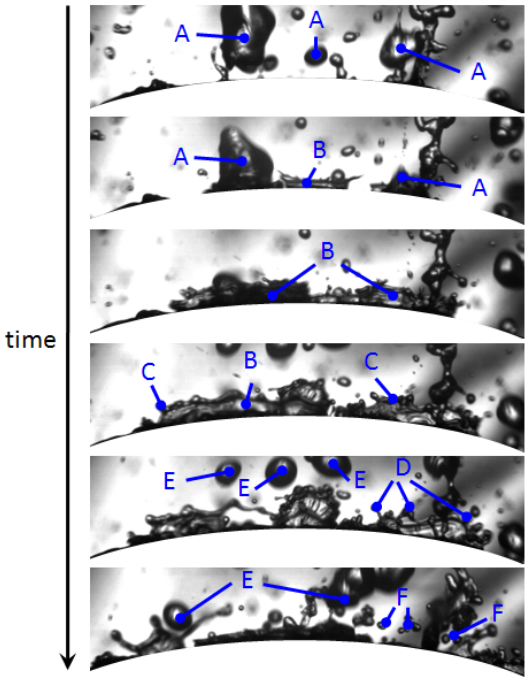

Figure 5.1: High-speed images captured at 8000 fps showing a typical film created by spray impact onto a target under μg conditions and the target in white. A - impacting drops, B - uprising sheets, C - emerging rims, D - finger-like jets appeared at the rim, E - new impacting drops, F - secondary drops.

By observing the dynamics of a film created by the deposited drops during microgravity experiments, typical scenarios are presented in Figure 5.1 when drops are impacting onto a spherical target (shown in white) such as uprising sheets (B), free rims (C), finger-like jets appearing at the rim (D) and secondary drops (F). These images have been captured using a high-speed video system at 8000 frames per second. Drops impacting onto a wall film (A) create a relatively fast radially expanding flow which interacts with the outer stationary liquid film. The interaction of these two flows gives rise to a free uprising liquid sheet (B). The motion of the edges of these free sheets is governed by the surface tension. In fact the velocity of the sheet edge is smaller than the velocity of the sheets itself. This velocity difference leads to the formation of a rim always bounding a free liquid film. The volume of the rim continuously increases due to the flow entering the rim (C) from the sheet (B).

Nevertheless, this scenario happening also on ground cannot be completely excluded for some spray parameters. In Section 5.3, the effect of the gravity on the wall film thickness have been studied. However, in this section, we are focusing on the outcome of spray impact and on the dynamics of splash associated with spray impact. In a very unusual microgravity splash scenario the rim, bounding the free uprising sheet, detaches. Figure 5.2 shows this curious splash scenario produced after the break-up of a free sheet (B) that has been noticed for the first time in a microgravity environment. Due to capillary forces the rim emerges firstly (see Figures 5.1 and 5.2,C).

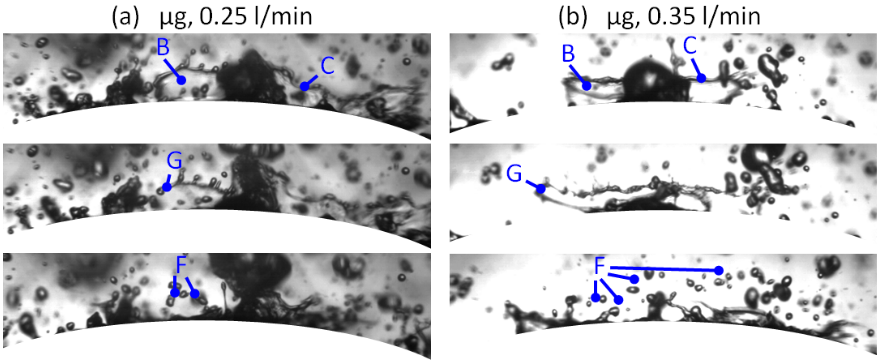

Figure 5.2: Unique splash produced after a free sheet break-up under μg for (a) 0.25 l/min and (b) 0.35 l/min with B - uprising sheets, C - emerging rims, G - rim detachment, sheet break-up and free jet forming. In the end, secondary drops are formed (F).

As shown in Figure 5.2 for $\dot{V} = 0.25$ l/min and 0.35 l/min the rim detaches from the free uprising sheet (G) and is then suspended in the air for some time. After the capillary break-up of a jet, it consequently breaks up into several secondary drops (F).

However, the phenomena of spray impact is even more complicated and rich on various phenomena (see Roisman et al. (2006)). If we compare the splash formation under microgravity environment with the one at positive hypergravity in Figure 5.3, then we observe in both cases that the splash with uprising sheets (B) leads to the formation of the jets (D) emerging directly from the rim (C). Such bifurcating jets (H) have often been observed during previous spray impact studies but the mechanism of their formation was completely unclear (Roisman et al. (2007)). Thanks to the microgravity experiments it is clear that these bifurcating jets (H) are formed after the break-up and merging of an uprising sheet (B).

In comparison, the creation of bifurcating jets during 2g (see Figure 5.3, (b)) is affected by the gravitational force. In that case, both, the finger-like jets appearing at the rim and the bifurcations are dragged down to the target's surface and have not the possibility to emerge as under microgravity environment.

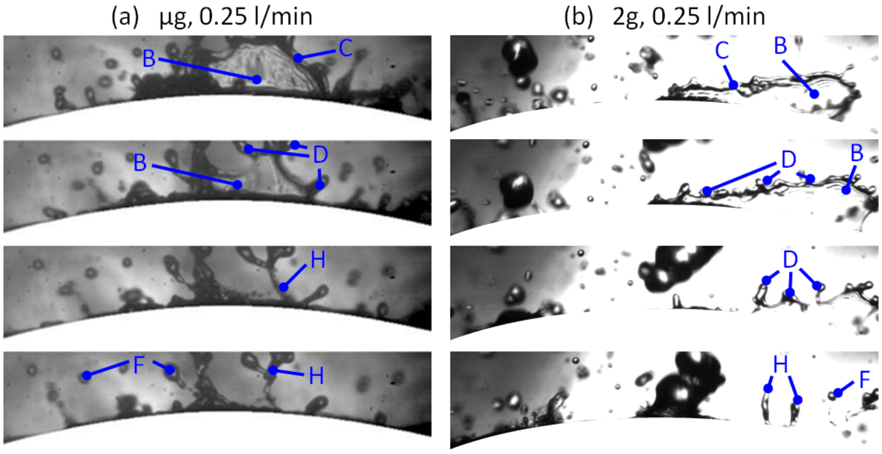
(a) µg, 0.25 l/min
(b) 2g, 0.25 l/min

Figure 5.3: Formation of single bifurcation jets (H) at 0.25 l/min, (a) μg and (b) 2g accompanied by B - uprising sheets, C - emerging rims, D - finger-like jets appearing at the rim and F - secondary drop formations.

In addition, when comparing the crown formation in Figure 5.4, again between μg and 2g, then we notice the common behavior with uprising sheets (B), emerging rims C, finger-like jets at the rim D for the case of μg whereas at 2g only a thicker merging rim (C) that is bounding the uprising sheet (B) is observable. At the end, secondary drops (F) are created in μg. On the contrary, no secondary drops are generated at 2g. The previously merged rim collapses sustaining the liquid sheet and finally coincides with the fluctuating liquid film produced by spray impact onto the target.

Hence, we can extend the phenomena of spray-wall interaction from Figure 2.2 and broaden the splash scenarios. The previously mentioned morphologies are illustrated schematically in an overview in Figure 5.5 and classified as follows: B - corona splash with uprising sheet, D - finger-like jets appeared at the rim, G - rim detachment, sheet break-up and free jet formation, H - single bifurcation jets formed after the break-up and merging of an uprising sheet.

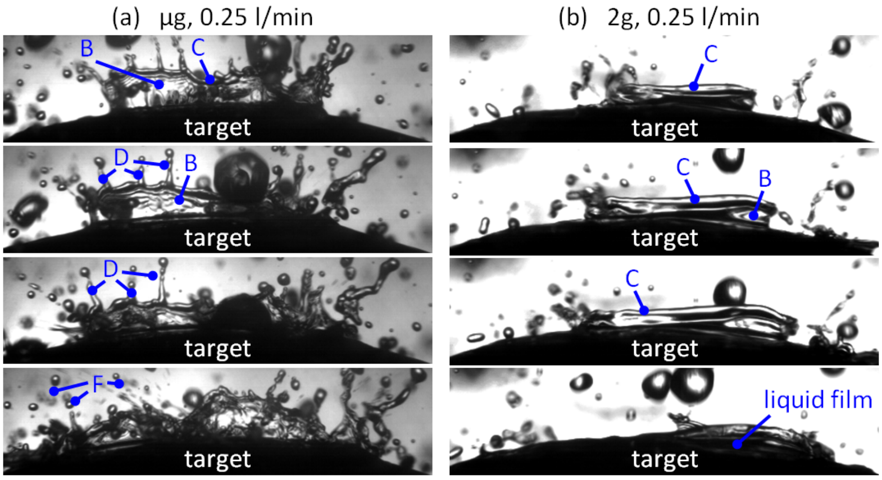
(a) µg, 0.25 l/min
(b) 2g, 0.25 l/min

Figure 5.4: Crown formation at 0.25 l/min, (a) μg and (b) 2g with B - uprising sheets, C - emerging rims, D - finger-like jets appearing at the rim and F - secondary drop formations.

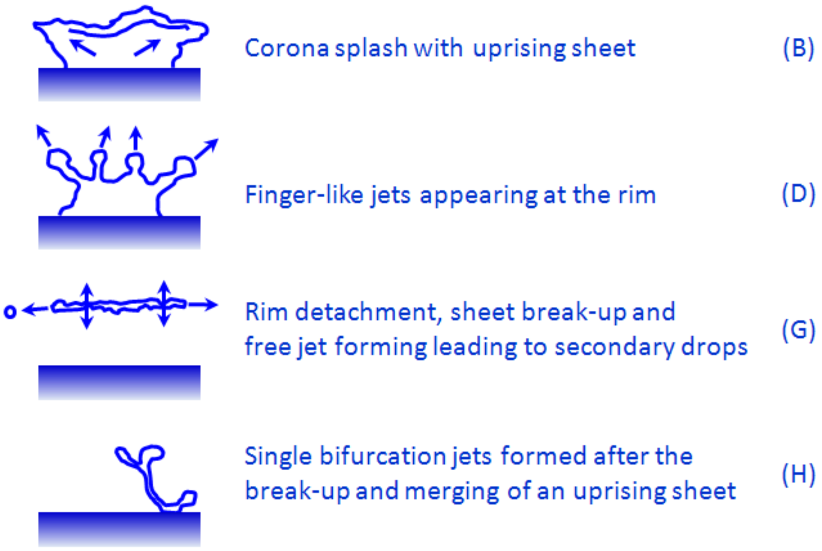

Figure 5.5: Updated phenomena of spray-wall interaction occurring in a microgravity environment.

5.1.2 Splash scenarios at $\pm \acute{v}$g

In comparison to microgravity observations where length and time are scaled up, this section analyzes the spray propagation and wall impact observed at various negative (-$\acute{v}$g) and positive hypergravity (+$\acute{v}$g) levels. Figure 5.6 shows a spray impacting onto the convex target at a constant flow rate of 0.25 l/min but for different gravity levels: from the maximal positive hypergravity condition 20g to 2g and the minimum gravity condition -20g to -2g.

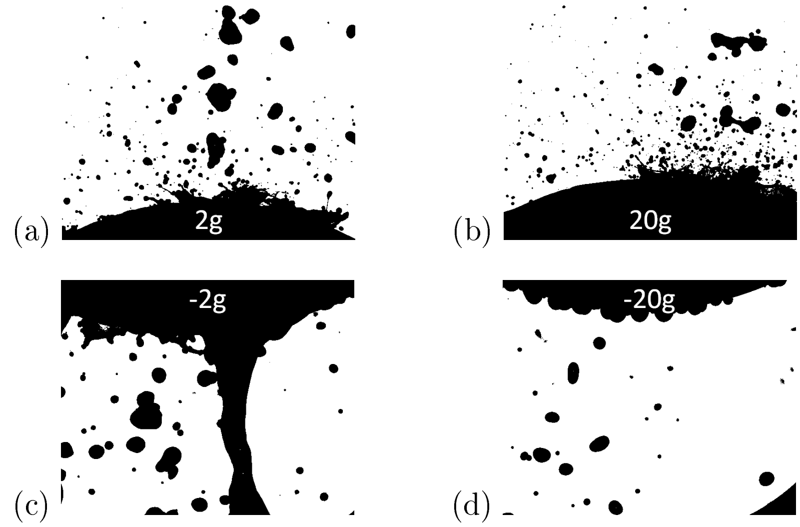

Figure 5.6: Spray impact hydrodynamics for $\dot{V} = 0.25$ l/min and at (a), (b) positive and (c), (d) negative hypergravity.

What we can see in these figures is that the spray behaves completely different although the water flow rate is constant. In Figure 5.6 (a) and (b), the spray appears comparable but a qualitative evaluation of the impacting drops in Section 4.2 has shown that the impact velocity u increases slightly at higher gravity levels. This trend is common throughout the entire range of water flow rate as previously shown in Figure 4.34. At the highest flow rate this dependence is less and the drop velocity is determined to a large extent by the velocity of the drop at the nozzle exit.

Unlike Figure 5.6 (a) and (b), the generated liquid film in Figure 5.6 (c) jets down like a filament whereas in (d) basically no drop reaches the target. At moderate negative positive hypergravity conditions, the drops experience centrifugal forces away from the target and the secondary spray after impacting forms a jet-like structure. This spray mode will be denoted film jetting and is independent from the gravity level or water flow rate (see Table 5.1).

Film jetting can be also observed when referring to the same gravity level of -20g (compare Figure 5.6 (d)) but at higher flow rates, see Figure 5.7 (a), (b) and Table 5.1.

The captured images show that at higher flow rates there are more finger-like filaments appearing from the liquid film at -$\acute{v}$g. It also looks as if there are more but thinner and smaller film jets developing with an increase of the water flow rate. Another effect that can be observed is the break-up of the film jetting at higher flow rates leading to larger secondary drops. Figures 5.7 (b) and (c) for instance, suggest that at -20g the secondary drops pinch off sooner from the film jets. There are more drop

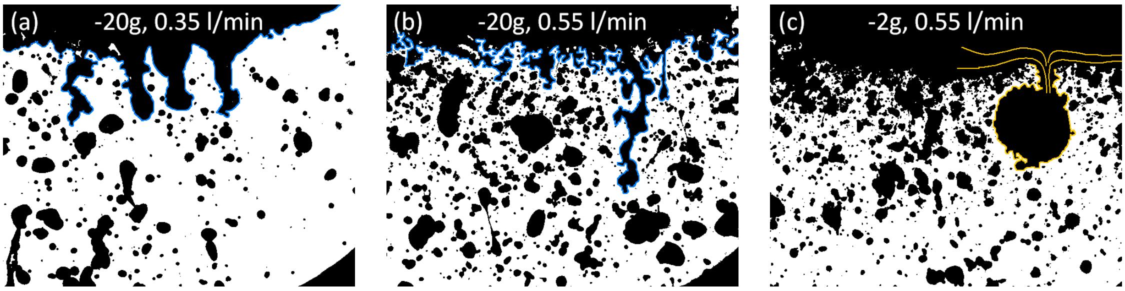

Figure 5.7: Secondary spray effects at various spray impact parameters with film jetting in (a) -20g, 0.35 l/min and (b) -20g, 0.55 l/min and enormous drop formation in (c) -2g, 0.55 l/min.

Table 5.1: Modes of spray-wall collision at various gravity levels. Notations correspond to: *n* = no secondary spray, *j* = film jetting, *d* = drop formation, *s* = common secondary spray

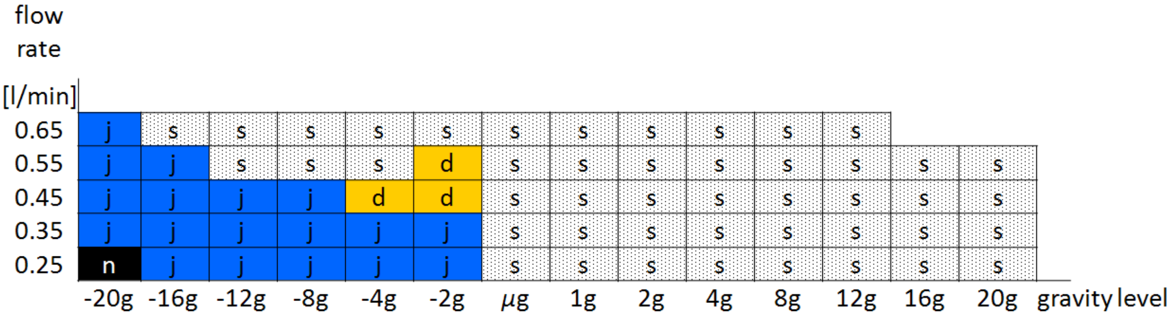

flow rate [l/min]	-20g	-16g	-12g	-8g	-4g	-2g	μg	1g	2g	4g	8g	12g	16g	20g
0.65	j	s	s	s	s	s	s	s	s	s	s	s		
0.55	j	j	s	s	s	d	s	s	s	s	s	s	s	s
0.45	j	j	j	j	d	d	s	s	s	s	s	s	s	s
0.35	j	j	j	j	j	j	s	s	s	s	s	s	s	s
0.25	n	j	j	j	j	j	s	s	s	s	s	s	s	s

formations than at -2g but in addition those drops are much smaller. Taking also a closer look at Figure 5.7 (c), at -2g the body force is not sufficient to break up the large drop and this drop grows even larger with accumulating secondary drops.

In the work of Kyriopoulos et al. (2009a), the behavior of the secondary spray is also summarized (see Table 5.1) and is illustrated in image sequences in Figure 5.8.

Gravity has a considerable effect on the morphology of the near-wall flow as presented firstly by Roisman et al. (2007). According to Figure 5.5, an overview of the spray-wall interaction phenomena occurring under positive and negative hypergravity is given in Figure 5.9: *j* - film jetting like a filament in finger-like structures resulting from the liquid film, *d* - huge secondary drops pinching off sooner from the liquid film jets, *n* - no secondary spray formation since drops that reach the target remain on its surface but most of them do not impact at all.

To summarize, the spray-wall interaction observations in this chapter answer essential and fundamental questions regarding the liquid film thickness (Kyriopoulos et al.

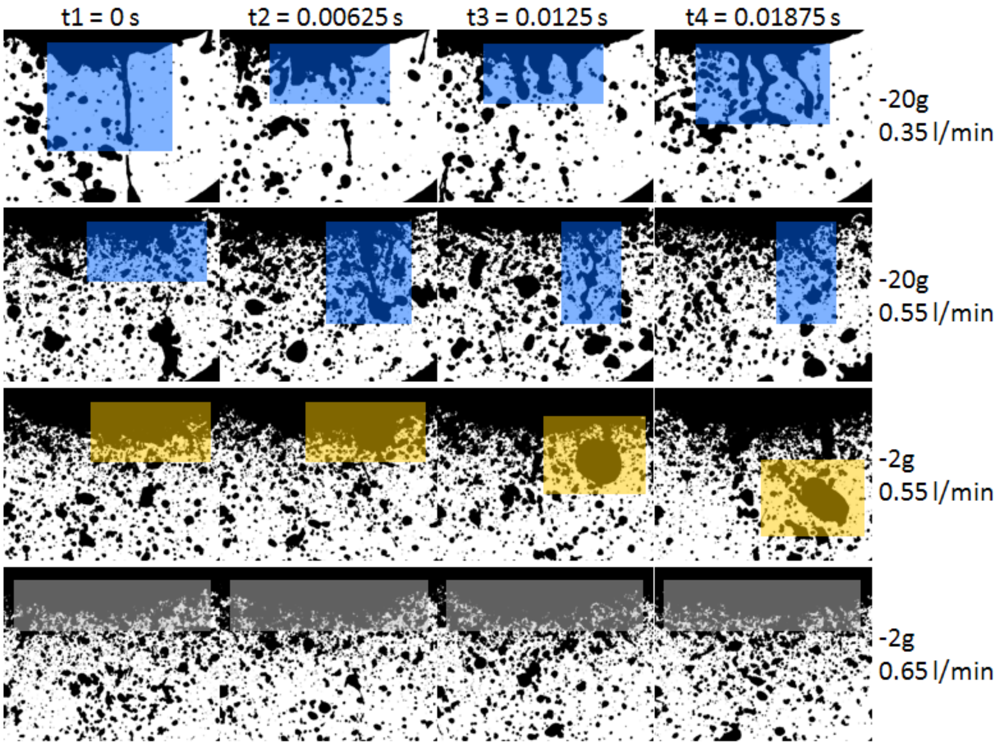

Figure 5.8: Sequences of high-speed images referring to various spray modes: film jetting (blue), drop formation (orange) and common secondary spray (gray).

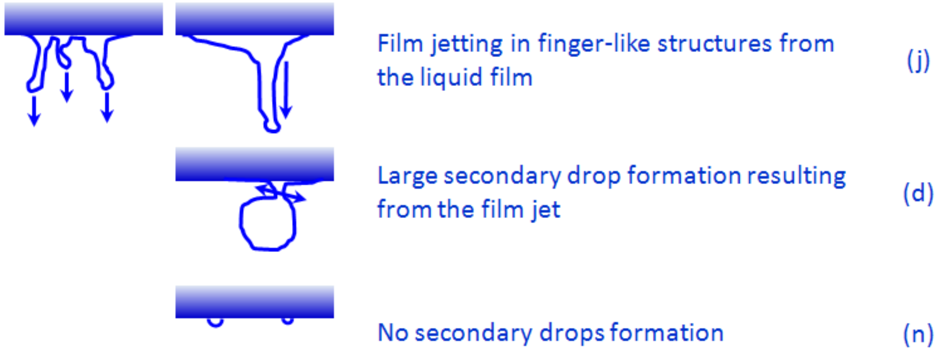

Figure 5.9: Spray-wall interaction morphologies for the case of negative positive hypergravity environment.

(2009b)). Before the performance of these experiments at various gravity levels the formation of a liquid film was uncertain. At this moment, we can definitely verify the existence of a liquid film throughout all gravity conditions and guarantee an enclosed film.

5.2 Image Processing

Previous observations gained with a high-speed infrared camera are important to firstly demonstrate that it exists a constant fluctuating film throughout the experiments. From the movies it is obvious that the liquid film is covering the target continuously. However, pictures were taken to characterize the film pattern and to compare the film distribution resulting from the drops impacting on the heated target. It is seen from the infrared images in Figure 5.10 that at the lower flow rate (a) the drops impacting onto the heated target are larger but spatially sparser than at the higher flow rate (b). The tendency that the spray drops become smaller at higher water flow rates is also proven quantitatively by the phase Doppler instrument in Section 4.1 and by image analysis in Section 4.2. As written in Kyriopoulos et al. (2008a), this is evident from the drop impact temperature footprint apparent in the images, where the darker shade represents a cooling of the surface upon drop impact.

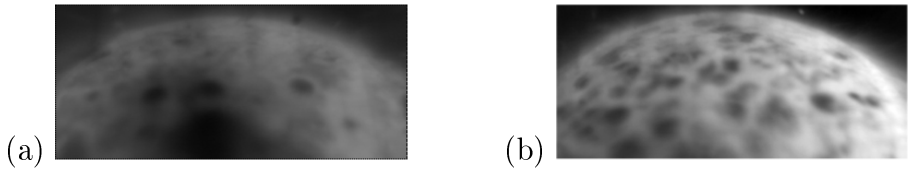

Figure 5.10: Liquid film pattern footprint when spray impacts onto a heated target at a constant gravity level for (a) 0.25 l/min and (b) 0.55 l/min. Lighter shades represent the hot water film covering the target surface, darker shades signify recent impingement of cold drops.

Since it is very difficult to find a reliable parameter accounting for the liquid film morphology only from observation, a robust method is needed to characterize the fluctuating liquid film. The collected images have been firstly processed with the help of an edge detection technique to delineate the liquid film contour of the wetted target. Then, its total length has been evaluated, compared with the contour of the dry target in order to define the averaged minimal distance from the liquid film to the dry target. Those image processing steps are now being described in more detail, beginning with the original captured image in Figure 5.11 (a).

By adjusting the image contrast and using a filter provided by MATLAB the intensity of the picture in order to heighten the gradient at the contour is regulated, see Figure 5.11 (b). The algorithm applies the image adjusting filter to the image. Then the picture is recombined again. This step is performed since the intensity level at different parts of the picture is different and should be treated separately.

In a further step, a binary image is being extracted and the threshold level for converting this image finally into a black-and-white image is determined automatically. The resulting image with a white background and a black target and liquid film part is shown in Figure 5.11 (c).

Small unnecessary objects that are still present (from the complement), as in this exemplary image Figure 5.11 (c) found inside the crowns, need to be removed in a next step, or rather refilled so that the contour can be detected correctly as a continuous line (compare Figure 5.12 (b)).

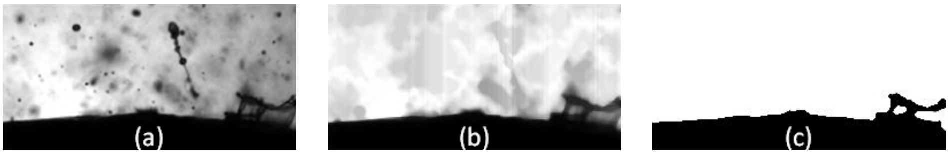

Figure 5.11: Basic image processing steps (a)-(c) starting with the original captured image (a) and leading to a black-and-white picture (c).

Now the image is ready for determining the contour and a further MATLAB command is applied which creates a cell array containing the coordinates of all objects found in this image. The boundary having maximum length is taken from this array. This should be the desired contour that we need for further analysis.

Figure 5.12 exemplifies the result when applying the previously described image processing method at another typical spray impact image ($\dot{V} = 0.30$ l/min) including crowns, craters, jets, upraising sheets with the general aim to identify the liquid film contour. In order to compute the film thickness distribution the distance from any point at the surface of the dry target perpendicular to the corresponding nearest point at the liquid film contour (marked with blue line in Figure 5.12 (b)) has been calculated. Firstly, a minimal and maximal contour-to-target distance have been determined (see Figure 5.12 (c)) but since a reliable and reproducible film thickness is essential for further investigations, only the minimal contour-to-target distance has been chosen as a meaningful one (see also Figure 5.13). The maximum or average contour-to-target has not come into consideration because of the strong involvement of crown heights and upraising sheets.

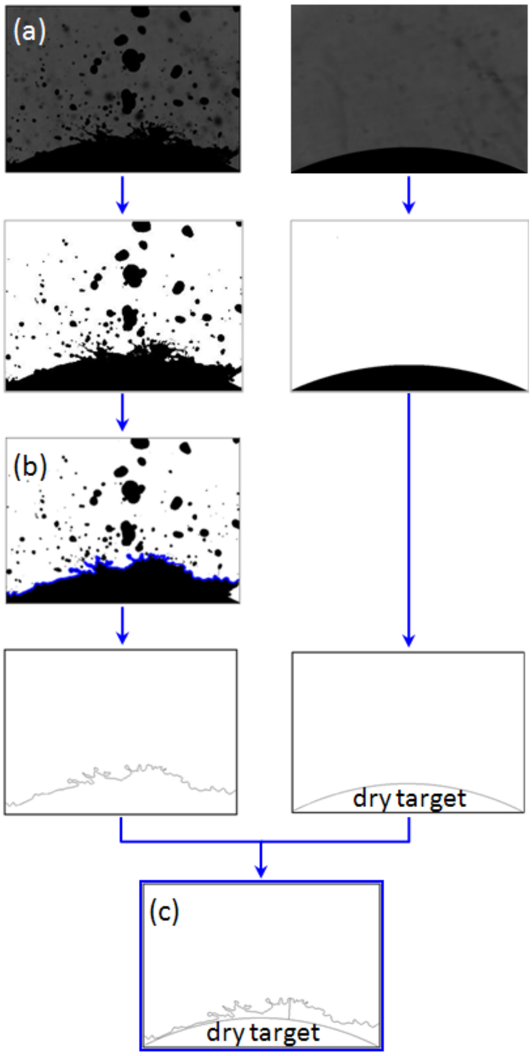

Figure 5.12: Image processing method: (a) initial image, (b) liquid film contour line, (c) liquid film thickness distribution: spherical dry target projected in white, wetted target shown in gray scale values.

5.3 Measurements of film thickness

It is not yet clear how the effects of film formation and crown development are to be modeled. In our studies the resulting averaged minimal value of the contour-to-target-distance $\bar{h}_{film}$ is defined as the characteristic film thickness (Kyriopoulos et al. (2008a)).

In a first step, in order to define the film thickness distribution, the image processing procedure shown in Figure 5.12 detects the contour of the wall film including the crowns and jets. The image processing tool by Kyriopoulos et al. (2008a) scans the whole hydrodynamic process and its film formations and calculates the distances from a point of the liquid film contour to the corresponding nearest orthogonal point at the surface of the dry target named contour-to-target-distance. Then, the minimum contour-to-target-distance h_{film} is taken into account for further analysis. Figure 5.13 illustrates this robust method in detail for an originally captured image including a liquid film and a crown formation encircle the minimal value h_{film} for this example image.

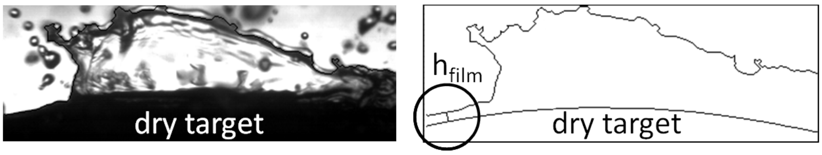

Figure 5.13: Determination of the film contour-to-target distance in an initially captured image with the help of a robust image processing tool.

For each image this minimal film contour-to-target distance h_{film} has been calculated. The fluctuating film is moving so fast that images have been definitely captured at different states. Therefore, it is guaranteed that we are not considering an identical film situation with a same h_{film}. These data have been then averaged in the work of Kyriopoulos et al. (2008a) over a series of images corresponding to the same parameter set. In Figure 5.14 the averaged values $\bar{h}_{film}$ of the minimal film contour-to-target distance h_{film} for a series of 5000 images taken on ground as well as for a series of 512 to 2048 images from parabolic flights for the given water flow rate are shown. The resulting minimal averaged value $\bar{h}_{film}$ can be taken as the characteristic thickness of the liquid layer not accounting the uprising crowns and jets. Figure 5.14 presents the results for the characteristic film thickness including the standard deviation *sdt* gained during parabolic flights (PFC) and TEXUS 45. In both experimental platforms, data have been obtained for microgravity. The results for TEXUS 45 are referring only to $\dot{V} = 0.45$ l/min and are arranged in the range of the error bar.

In addition, experiments were performed on ground and also during the 1g phase of PFC for comparison reasons. All resulting values for $\bar{h}_{film}$ of comparative measurements match pretty well in consideration of the standard deviation bars. The 2g data have been attained in the positive hypergravity phase during parabolic flights.

There are several tendencies that can be observed in this figure. By increasing the water flow rate starting at approximately 0.35 l/min the minimal film contour-to-target distance $\bar{h}_{film}$ significantly increases independent of the gravity level. It varies insignificantly with further increasing of the flow rate for ground (1g) and microgravity (μg). By comparing the results only of 1g and μg, we see a large difference between the aver-

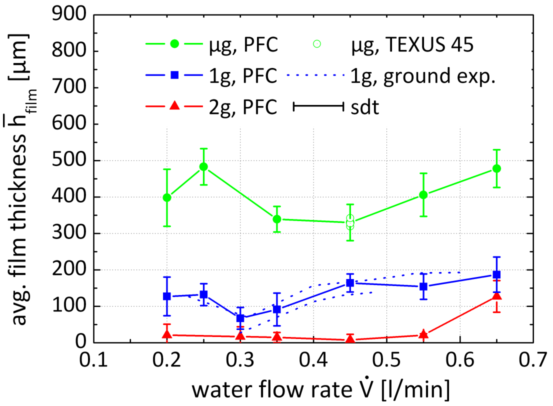

Figure 5.14: Results of the minimal averaged film contour-to-target distance $\bar{h}_{film}$ with standard deviation for various water flow rates and different gravity conditions obtained during parabolic flight campaigns (PFC), on board the sounding rocket (TEXUS 45) and on ground: μg, 1g and 2g.

aged values. The microgravity values are 180-360 μm larger than the ones for ground conditions. Regarding the results of the positive hypergravity phase, the values tend to be much smaller but in order to evaluate these results, further observations focusing only on those experimental conditions are necessary.

When adding the evaluation of the centrifuge experiments to Figure 5.14, we receive the results in Figure 5.15. Due to the amount of gravity data and equivalent progression in these results, the chosen gravity levels are spaced at approximately 4g-intervals. The standard deviation is not illustrated in the following $\bar{h}_{film}$-graphs since the results become unclear. Figure 5.14 (a) includes also the results of μg and 1g for a better comparison whereas the plot (b) only illustrates the analysis of the positive hypergravity ($+\acute{v}$g) experiments. By comparing the film thickness results from microgravity and 1g with the ones at various gravity levels a large difference between the minimal averaged values for ground and microgravity are indicated. In Figure 5.14 (b), we are zooming in on the results of $+\acute{v}$g (ZARM) including the 2g evaluation of parabolic flights (PFC).

The results for 2g agree very well that means the effect of gravity is reproducible independently of the experimental platform. In addition, we identify the tendency that the thickness of the thin liquid film decreases when the gravity component normal to the wall increases. Besides, the average film thickness increases in the majority of cases at a higher water flow rate. Nevertheless, these are only tendencies and $\bar{h}_{film}$ varies marginally when keeping in mind that approximately 30 μm correspond to 1 pixel. We are aware of the constraints of the image processing evaluation. In order

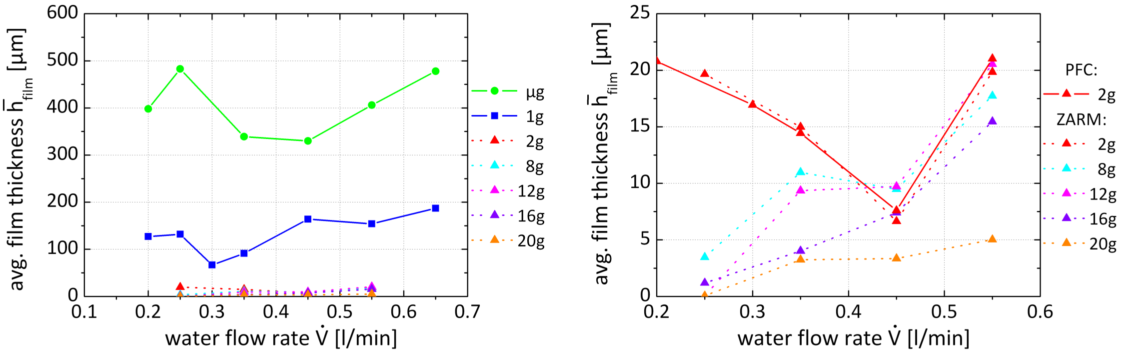

(a) (b)

Figure 5.15: Comparison of the characteristic film thickness from Figure 5.14 (μg, 1g and 2g) with various $+\acute{v}$g results (a). Zoomed in outcome only for the $+\acute{v}$g phase (ZARM) and the 2g experiment during parabolic flights (PFC) (b).

to determine $\bar{h}_{film}$ more precisely, a high-speed camera with a higher resolution is necessary.

For the negative hypergravity case (-$\acute{v}$g), the results for the average film thickness $\bar{h}_{film}$ in Figure 5.16 seem more chaotic at first sight and not in conformity with each other. But if we classify two gravity groups with g $\leq$ -12g and g $\geq$ -8g, then we can tell the outcome apart: for the gravity levels -20g, -16g and -12g $\bar{h}_{film}$ increases with an increase of the water flow rate $\dot{V}$ whereas for the gravity levels -8g, -4g and -2g, $\bar{h}_{film}$ decreases with an increase of $\dot{V}$. In both cases, we can notice that the values for $\bar{h}_{film}$ are much greater than the ones on ground and the ones at $+\acute{v}$g (compare Figure 5.15). In addition, the results for the average film thickness of the microgravity experiments (Figure 5.16, PFC) are closer to the data of the highest -$\acute{v}$g level and rather in the same range than with the data obtained on ground (Figure 5.15, 1g). Besides, we can observe that at lower water flow rates (0.25 l/min - 0.45 l/min), the results for $\bar{h}_{film}$ differ stronger than at higher ones (0.55 l/min - 0.65 l/min). Hence, the gravitational forces are rather affecting large and slow drops (lower water flow rates).

One data point that attracts attention refers to the parameter set of -20g and $\dot{V}$ = 0.25 l/min. By only taking a look at this distribution in Figure 5.16 without questioning the spray behavior itself, this data point is revealed very small (almost 0 μm) and therefore incomprehensible. But this outsider can be easily explained when keeping in mind the morphology of the liquid film and its formation from observations in Section 5.1.

For a better understanding of the effect of the secondary spray modes at negative

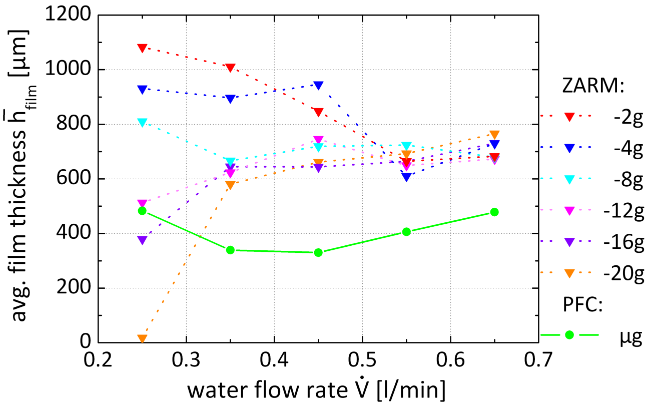

Figure 5.16: Averaged film contour-to-target distance $\bar{h}_{film}$ for different -$\acute{v}$g levels referring to various water flow rates. For comparison, the results of μg obtained during parabolic flights (PFC) are included.

hypergravity, we embed the previously defined mode types from Table 5.1 in Figure 5.16. The result is displayed in the following Figure 5.17.

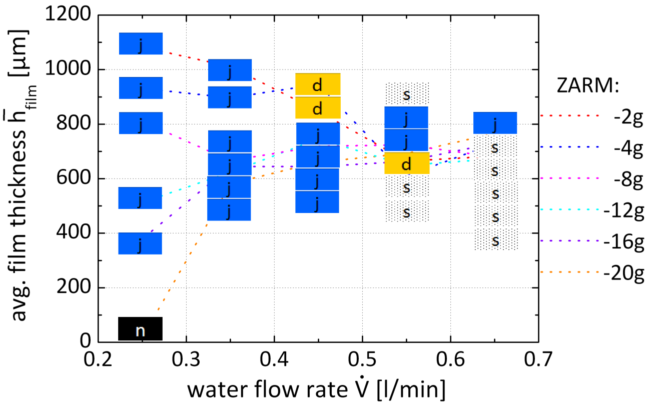

Figure 5.17: Spray modes referring to the averaged film contour-to-target distance $\bar{h}_{film}$ in Figure 5.16 for different -$\acute{v}$g levels and various water flow rates; n = no secondary spray, j = film jetting, d = drop formation, s = common secondary spray.

The diagram brings together the specific spray phenomenon for the relevant average film thickness $\bar{h}_{film}$. It stands out that at lower water flow rate, there is a marginal secondary spray formation but a strong film jetting. Hence, it is important for our studies to not only focus on the results of the investigations but to also consider observations of the phenomenon and to analyze qualitatively the spray-wall interaction. The effect of gravity on spray impact manifests itself not only in the spray drop size and the drop velocity (see Chapter 4) as well as in the change of the film thickness but also in the morphology.

5.4 Results and discussion

A further modeling correlation referring to the drop impact diameter and the film thickness parameter (see dimensionless film thickness in Equation 2.5) is presented in the following. It is still a challenging task to estimate the film thickness and to describe the film flow generated by spray impact onto a wall. Its hydrodynamics is determined by typical time and velocity scales associated with single drop impacts and is not completely understood.

In Roisman et al. (2008) the time for a single drop impact is estimated as given in Equation 5.1 for a relatively high Weber number when accounting the maximal time of a crown spreading T_{max} as the characteristic time scale and the parameter β as a function of the initial film thickness.

$$T_{max} \approx \frac{\beta H We}{8U} \quad \text{with} \quad \beta = 0.62H^{-1/3} \quad \text{and} \quad H = \frac{\bar{h}_{film}}{D_{32}} \quad \text{at} \quad 0.5 < H < 2 \tag{5.1}$$

In this expression, β is an adjustable function resulting from fittings with experiments. The given range of the dimensionless film thickness H (compare also Equation 2.5) is kept in our analysis.

In a further step, the film thickness is scaled by the thickness of the oscillating viscous boundary layer $H_v \sim \sqrt{vT_{max}}$. The following scaling solution for the film thickness applies with $H \sim H_v$ (Roisman et al. (2008)).

$$\frac{\bar{h}_{film}}{D_{32}} \sim \left(\frac{We}{Re}\right)^{3/4} = Ca^{3/4} \tag{5.2}$$

In Figure 5.18 the determined dimensionless film thickness $\bar{h}_{film}/D_{32}$ is shown as a function of the in Equation 5.2 given dimensionless group $Ca^{3/4}$ where Ca is the Capillary number. Diagram (a) displays the data evaluated for all gravity conditions: negative hypergravity (-$\acute{v}$g), microgravity (μg), ground (1g) and positive hypergravity (+$\acute{v}$g). Again, the data points for -$\acute{v}$g pointed out in this figure disagree stronger whereas the rest of the data seem in a certain order. Nevertheless, there is a tendency that the values for the dimensionless film thickness increase with $(We/Re)^{3/4}$ for all gravity levels and additionally with an increase of the water flow rate.

This becomes clearer when neglecting the -$\acute{v}$g values as realized in Figure 5.18 (b)). At higher water flow rates $\bar{h}_{film}/D_{32}$ increases significantly with $(We/Re)^{3/4}$.

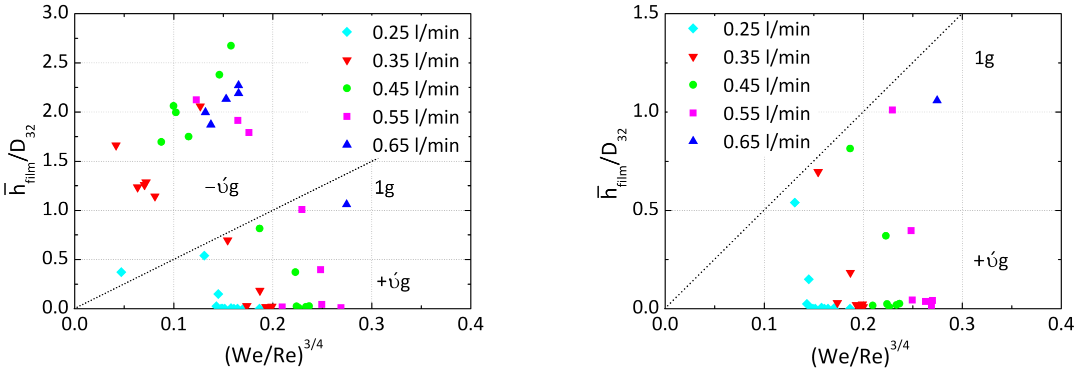

(a) (b)

Figure 5.18: Dimensionless film thickness $\bar{h}_{film}/D_{32}$ plotted against the dimensionless group $(We/Re)^{3/4}$ for negative hypergravity (-$\acute{v}$g), ground (1g) and positive hypergravity (+$\acute{v}$g) levels.

In order to filter out the influence of gravity, these data points from Figure 5.18 (b) are now assigned to the various gravity levels μg, 1g and +$\acute{v}$g (see Figure 5.19). Compared to the -$\acute{v}$g results in Figure 5.18 (a), the assumption by Roisman et al. (2008) that the dimensionless film thickness depends almost linear on $(We/Re)^{3/4}$ is clearly confirmed for μg, 1g and +$\acute{v}$g shown in Figures 5.19 (a) and (b). The effect of gravity is remarkable in both graphs: with an increase of the gravity level the linear slope of the correlation decreases.

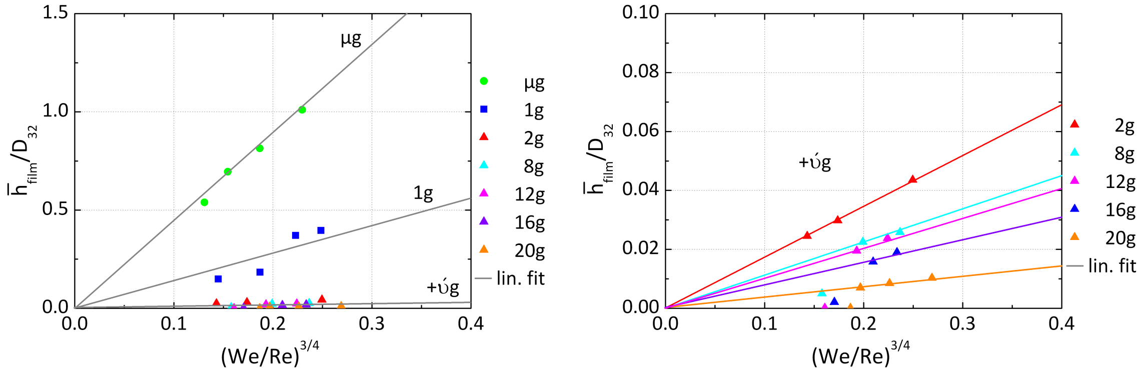

(a) (b)

Figure 5.19: Dimensionless film thickness H plotted against $Ca^{3/4}$ for (a) μg, 1g and +$\acute{v}$g and (b) zoomed in for only +$\acute{v}$g phase.

Hence, the film thickness produced by spray impact at positive hypergravity conditions can be estimated according to Equation 5.2 with a constant denoted with κ and a ratio between Weber and Reynolds number in the form of

$$\frac{\bar{h}_{film}}{D_{32}} = \kappa \left(\frac{We}{Re} \right)^{3/4} = \kappa Ca^{3/4} \tag{5.3}$$

Consequently, we can write corresponding to the various gravity levels the following expressions

$$\frac{\bar{h}_{film}}{D_{32}} = \begin{cases} 4.5 \left(\frac{We}{Re}\right)^{3/4} & \text{for microgravity } (\mu\text{g}) \\ 1.43 \left(\frac{We}{Re}\right)^{3/4} & \text{for ground (1g)} \\ 0.03 - 0.17 \left(\frac{We}{Re}\right)^{3/4} & \text{for positive hypergravity } (+\acute{v}\text{g}) \end{cases} \tag{5.4}$$

An almost linear dependency in previous analysis made by Batarseh (2008) (see Figure 5.20) is also supporting this correlation. Although the measurements of Batarseh (2008) have been performed with an airblast atomizer during spray impact onto a Plexiglas inclined wall mounted with different angles, there is a linear slope $\kappa = 8.95$.

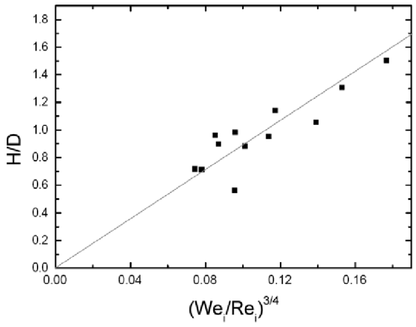

Figure 5.20: Experimental results for an inclined spray with $\kappa = 8.95$ (reprint from Batarseh (2008)).

Therefore, it seems that the constant κ depends on different factors such as spray configuration (normal or inclined), liquid properties, target geometry and Reynolds number but not on the water flow rate. With the help of these parameter changes and e.g. investigations with sprays at large Reynolds number ranges, the current data field could be extended. In addition, measurements with various target radius could lead to more reliable correlations as shown experimentally and theoretically in the work of Mustafic et al. (2004) where the characteristic film thickness increases with increasing of the radius of the spherical target. According to Batarseh (2008) measurements with very dense fuel sprays or measurements at relatively low Reynolds numbers in which the viscosity significantly influences the impact of single drops could be also of interest.

If we now determine all linear slopes for various gravity levels from Figure 5.19, then we receive a new correlation between the constant κ and the gravity illustrated in a logarithmic scaling in Figure 5.21.

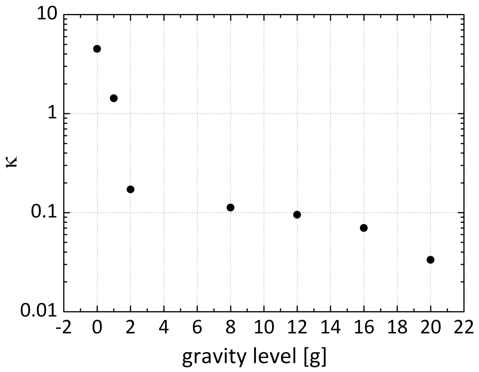

Figure 5.21: Logarithmic dependency between the linear slope κ and gravity.

To summarize, the studies of preliminary, already existing empirical models for the liquid film thickness are confirmed in this work not only for ground condition but remarkably also for further gravity levels. The hydrodynamics of the film are understood much better at the present stage of research. A universal model for the liquid film hydrodynamics can be formulated as in Equation 5.3. Referred to the in our studies generated spray impacting onto a convex target, the expanded expressions in Equation 5.4 apply.

Chapter 6

Spray cooling

The current study becomes even more challenging in the case of spray impact onto a heated surface. Spray cooling is governed by complex dynamics of the spray-wall interaction and is therefore itself a very complicated process. There are several mechanisms of convective heat removal from the target that are simultaneously active during spray cooling. In the following, some observations of spray cooling are presented and several parameters involved are discussed.

6.1 Observations

The convective heat transfer associated with spray impact is determined by the flow in the wall film. We assume that one of the significant factors affecting spray cooling and its efficiency is the minimal average liquid film thickness (see Section 5.3), created by spray impact. The work of Mühlbauer (2009) has proven that the wall temperature is almost not affecting the primary and secondary spray characteristics.

Figure 6.1 illustrates an infrared image of the spray-cooled target in microgravity (compare Kyriopoulos et al. (2007)). The oscillating liquid film completely covers the target surface and cools it down. The regions highlighted in red and yellow correspond to the already heated liquid film covering the target whereas the light blue and turquoise regions correspond to locations of recent cold drop impacts. In many cases the free liquid sheets are unstable and break up into secondary drops as previously shown in Section 5.1.1. Inertia of the impacting droplets is the main mechanism driving the near-wall two-phase flow. In addition, the flow morphology is determined by gravity, surface tension, viscosity, wettability and geometry of the target, and by phase change (stated in Celata et al. (2008)). The effect of evaporation may becomes very important far below the Leidenfrost temperature. If the wall temperature is several degrees above the saturation temperature at the given pressure, evaporation starts to play a role, sometimes a decisive role.

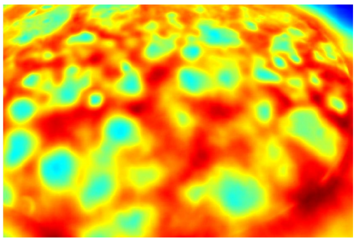

Figure 6.1: Spray-cooled target in microgravity environment captured with an infrared camera. Red and yellow regions correspond to hot water film covering the target. Light blue and turquoise regions correspond to locations of recent impingement of cold droplets.

Also, the average film thickness depends not only on the spray parameters but on the target geometry and gravity. Figure 6.2 shows that structures on a surface increase significantly the effectiveness of spray cooling. In these images a single drop impacting (a) onto an initially wetted, grooved, heated substrate is captured using a high-speed infrared camera under microgravity conditions. The impacting drop is colder than the liquid film (b) leading to a collection of its cold water in the grooves. The drop impact has created a crater in the liquid film (a large round area with irregular boundaries), which has resulted in liquid dry out at the groove crests (Figure 6.2, (c)). The groove troughs are filled with a cold liquid of a drop (d). Secondary droplets produced by splash are seen around the crater area.

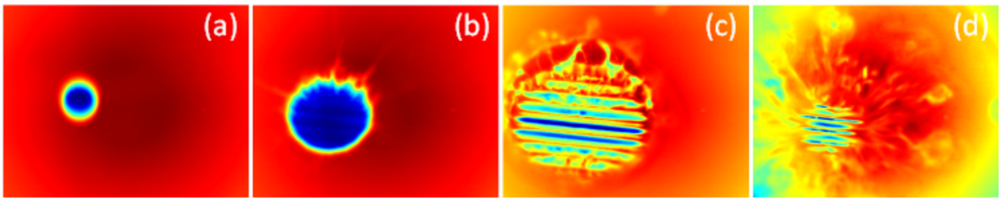

Figure 6.2: A single drop impacting onto an initially wetted, grooved, heated liquid film under microgravity conditions is captured using an infrared camera.

In our experiments, the heated target is cooled down due to contact with the colder liquid film provided by each impacting drop. The effect of gravity on spray impact and spray cooling has been firstly investigated during parabolic flights for various water flow rates and heating between 37.5 W to 150 W. Figure 6.3 (a) exemplifies a time evolution of the reference wall temperature for $\dot{V} = 0.45$ l/min together with the gravity level. These data have been obtained during one parabola sequence consisting of five parabolas within 1000 seconds. The results show that the wall temperature suddenly increases at the positive hypergravity (1.8g) to microgravity transition for each parabola. Hence, spray cooling becomes less effective in microgravity than under ground conditions and by trend more effective in positive hypergravity (see Kyriopoulos et al. (2008b)).

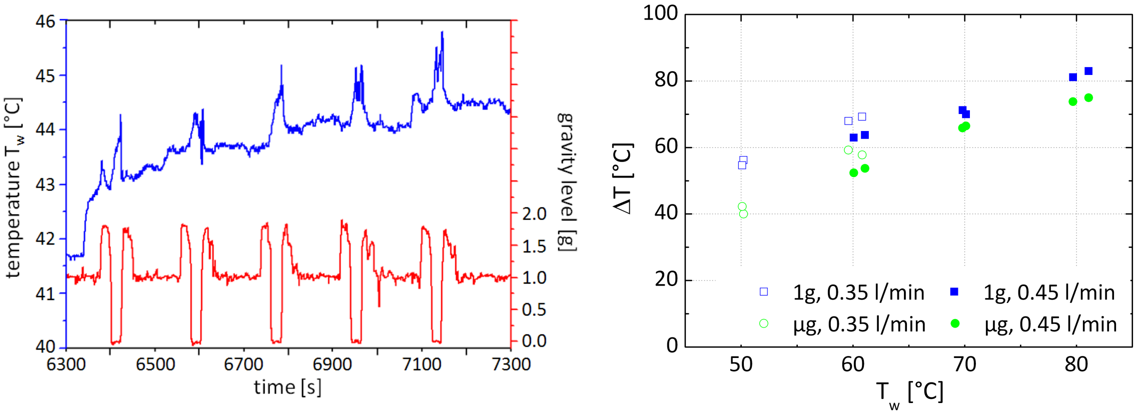

(a)

(b)

Figure 6.3: Micro-g results: (a) time evolution of the wall temperature T_w and the gravity level at a water flow rate $\dot{V} = 0.45$ l/min (PFC), (b) temperature difference ΔT plotted against the wall temperature T_w for $\dot{V} = 0.35$ l/min and 0.45 l/min (TEXUS-45).

But this indication needs to be treated carefully since the duration of a 21 seconds microgravity phase is not sufficient in order to establish a steady state temperature distribution in the system. Since these conditions are essentially nonstationary, investigations performed at a longer microgravity duration were needed. In the work of Gambaryan-Roisman et al. (2007), it has been found that the gravity effect on heat transfer becomes significant for the water flow rates $\dot{V} > 0.4$ l/min and that gravity has the strongest effect on heat transfer for a water flow rate of $\dot{V} = 0.45$ l/min. Hence, this water flow rate has been chosen additional to $\dot{V} = 0.35$ l/min for the sounding rocket experiment (TEXUS-45). Experiments in that microgravity environment allow us to investigate the effect of microgravity on heat transfer associated with spray impact in a more convenient way since the microgravity data are gained at a stationary process.

Figure 6.3 (b) presents results from the TEXUS-45 campaign (compare Kyriopoulos et al. (2008c)). It compares the results for the temperature difference ΔT (defined as T_{ref_L} - T_{ref_U}, see Section 3.4) for ground and microgravity condition, for various wall temperatures and $\dot{V} = 0.35$ l/min and $\dot{V} = 0.45$ l/min. The tendency from parabolic flights that spray cooling is less effective at microgravity is confirmed for both water flow rates and throughout all wall temperatures. The secondary drops that are leaving the spray-induced film seem to carry away the hot liquid from the fluctuating film less effectively under microgravity. Besides, the values for the temperature difference increase with an increase of the wall temperature.

6.2 Experimental determination of heat transfer parameters

In general, we can distinguish between two effects contributing to the film thinning on convex targets: (i) shear force produced by the oblique impact of the drops onto the liquid film and (ii) gravity. Only the first of these mechanisms is relevant in microgravity conditions whereas the second one is of great interest for various negative hypergravity and positive hypergravity conditions. In the following, we are taking a closer look on the effect of gravity on spray cooling by further evaluating the heat transfer coefficient at various gravity conditions. Note that our convex target, consisting of two parts, has been calibrated by EADS Astrium. It has been covered with Al_2O_3 and heated monotonously at a constant heat in order to determine the thermal conductance of the resistance layer ϑ. The heat transfer coefficient α, corresponding to spray cooling, is then defined with the wall temperature T_w, the temperature of the liquid drop T_d, the reference temperature of the upper T_{ref_U} and lower thermocouple T_{ref_L} as well as $\vartheta = 2.39\ \frac{W}{K}$ as follows. Note that the wall temperature T_w is assumed to be the reference temperature of the upper thermocouple ΔT_{ref_U}.

$$\alpha = \frac{\dot{q}}{(T_w - T_d)} = \frac{4\dot{Q}}{\pi d^2 (T_{ref_U} - T_d)} \quad \text{with} \quad \dot{Q} = \vartheta \Delta T = \vartheta (T_{ref_L} - T_{ref_U}) \qquad (6.1)$$

Figure 6.4 illustrates the results of the heat transfer coefficient α for various gravity levels and water flow rates at a constant heating rate: (a) 185 W and (b) 265 W. At both heating powers, there is a monotonous growth with gravity for negative hypergravity levels whereas the characteristics at positive hypergravity conditions are rather constant. With an increase of the gravity level, α increases which can be explained as follows. The thin fluctuating liquid film is heated up and is swept away from the hot target surface due to the effects of inertia and gravity. Under positive hypergravity conditions, the liquid film is removed very fast compared to terrestrial conditions. In combination with a decrease of the liquid film thickness (see Figure 5.15), a better heat removal is enabled. In negative hypergravity, the removal of the hot liquid from the target happens not so fast as on ground. This results in a reduction of the cooling performance as shown in Gambaryan-Roisman et al. (2007) and in an increase of the liquid film thickness. If the film produced by spray impact becomes thicker, it also reduces the film evaporation rate, which is an important cooling mechanism if the wall temperature is close to or exceeds the saturation temperature (see Celata et al. (2008)). Since we investigate below the saturation temperature, the latent heat transfer is neglected at this point.

In addition, Figure 6.4 shows us that the water flow rate $\dot{V}$ has not such a significant effect on the heat transfer coefficient α as gravity. The gravitational force is stronger affecting α, especially for the range between -20g to 1g in comparison to positive hypergravity (2g to 20g). This is a very surprising and an unexpected result at this present stage of research. It seems that the spray morphologies including a thick liquid film presented in Figure 5.8 prevent an optimal cooling of the target surface. In comparison, under positive hypergravity, the spray cools it down more efficient due to the thin liquid film and its continuous heat transmission. Every single drop impact event creates a local velocity field with a component normal to the target surface. This component leads to intensification of the heat transfer in the film in the direction normal to the target surface. The drop impact may also lead to splash, which is connected with another cooling mechanism. The secondary droplets leaving the spray-induced film are carrying the hot liquid away from the film. At this point, we can make a note of the importance of the liquid film hydrodynamics mechanism for the spray cooling efficiency.

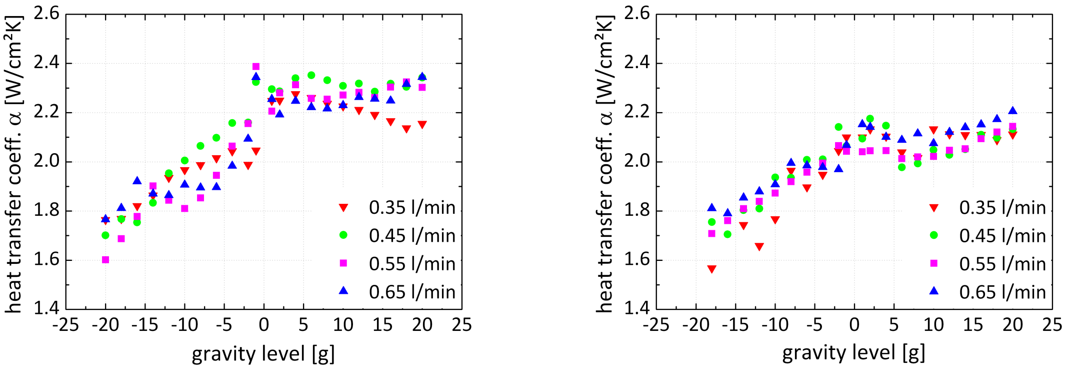

(a) 185 W (b) 265 W

Figure 6.4: Comparison of the results for the heat transfer coefficient α plotted against various gravity levels and various $\dot{V}$; different heating power (a) 185 W and (b) 265 W.

Other significant dimensionless numbers that are taken into consideration are the

Stanton number St, the Nusselt number Nu and the Péclet number Pe. The Stanton number St quantifies the ratio of heat transferred into a liquid to the thermal capacity of the liquid. Note that it is expressed in general by

$$St = \frac{\alpha}{c_p \rho v} \tag{6.2}$$

When implementing from Equation 6.1 the heat flux $\dot{Q}$, the wall temperature T_w, the temperature of the liquid drop T_d and expressing v by $A_{target}/\dot{V}$, it leads to

$$St = \frac{\dot{Q}}{\dot{m} c_p (T_w - T_d)} \tag{6.3}$$

with the water mass flow rate $\dot{m}$, the specific heat capacity of water $\mathrm{c}_p = 4187\ \frac{J}{kgK}$ and the wall temperature $T_w \mathrel{\widehat{=}} T_{ref_U}$ (reference temperature of upper thermocouple).

The Nusselt number Nu is defined in Equation 6.4. It is determined for the liquid film with the heat transfer coefficient α defined in Equation 6.1, the averaged minimum film thickness as the characteristic length $\bar{h}_{film}$ and the thermal conductivity of water $\lambda = 0.5984\ \frac{W}{mK}$

$$Nu_{film} = \frac{\alpha \bar{h}_{film}}{\lambda} \tag{6.4}$$

Another dimensionless number relevant to the study of transport phenomena in fluid flows is the Péclet number. We define this number based on the averaged minimum film thickness $\bar{h}_{film}$ as a length scale and by taking into account the spray volume flux as a velocity scale. This leads to a modified Péclet number Pe^* with the thermal diffusivity of water $a = 10^{-6}\ \frac{m^2}{s}$ and the water flow rate $\dot{m}$, the density ρ and the target diameter d_{target}

$$Pe^* = \frac{\bar{h}_{film}}{a} \frac{\dot{m}}{\rho \pi d_{target}^2} = \frac{\bar{h}_{film}}{a} \frac{\dot{m}}{4 A_{target}} \tag{6.5}$$

These two dimensionless numbers are correlated to each other in the next section in order to provide a sound basis for spray cooling modeling.

6.3 Results and discussion

In the following, the effect of gravity on spray cooling and empirical correlations are discussed. Figure 6.5 displays the Stanton number St plotted against various gravity levels for different water flow rates. The spray cooling process is more effective on ground and positive hypergravity compared to negative hypergravity and microgravity (compare Figure 6.3 (b)). We can give reasons for this behavior with the average minimal thickness of the liquid film that is increasing corresponding to Figure 5.15 (b) with an increase of the water flow rate. Additionally, the dynamics of the liquid film plays an important role for spray cooling.

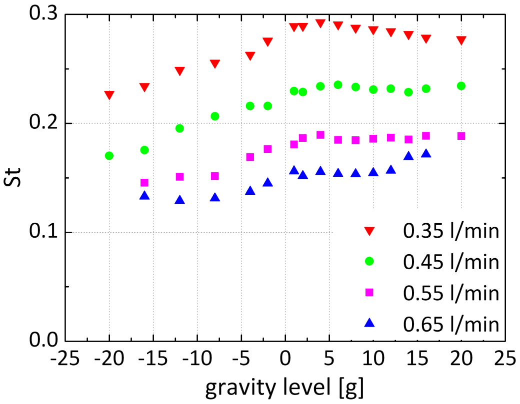

Figure 6.5: Results of the spray cooling efficiency at various water flow rates presented for diverse gravity levels.

In Figure 6.6, the Stanton number St is displayed versus the wall temperature for various gravity levels. The results for a constant heating of 185 W and various gravity levels and water flow rates are shown in (a) whereas (b) illustrates only the results for 1g to 20g, again for various water flow rates $\dot{V}$. The effectiveness of spray cooling clearly depends in both graphs on the water flow rate. Besides, for ground and positive hypergravity conditions the spray cooling process seems not to be influenced by the gravity level as for negative hypergravity, independent from the heating power. In that case, the values for the Stanton number St are almost constant for each water flow rate. These tendencies are also verified in Figure 6.5.

One of the mechanisms of convective heat removal from the target is the removal of heat with the radial outflow of the cooling liquid film from the target surface.

Figure 6.7 presents the results for the Nusselt number of the liquid film Nu_{film} plotted in a logarithmic scale against the modified Péclet number Pe^{*}. It is obvious that there is a different behavior of the spray cooling process in the regimes positive hypergravity (+$\acute{v}$g), ground condition (1g) and negative hypergravity (-$\acute{v}$g).

Firstly, it can be noticed that Nu_{film} is always less than 1.0 for the positive hypergravity field but clearly greater than 1.0 for negative hypergravity. At positive hypergravity the liquid film is thinner, hence it is heated up completely faster. Therefore, the temperature gradient at the wall, subsequently the heat flux, is small. In

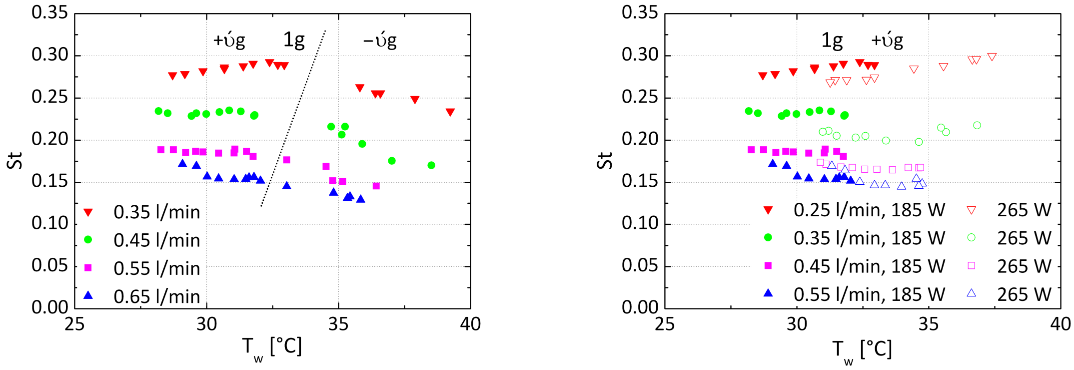

(a) (b)

Figure 6.6: Stanton number St plotted against the wall temperature for (a) all gravity levels, various water flow rates $\dot{V}$ and a constant heating (185 W), for (b) 1g and +ύg, various $\dot{V}$ and two different heating powers (185 W, 265 W).

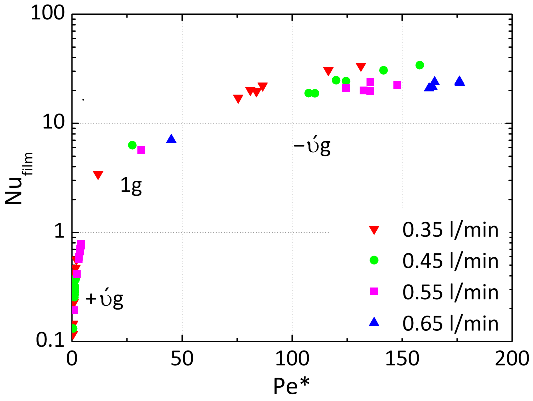

Figure 6.7: Results for the Nusselt number of the liquid film Nu_{film} versus the modified Péclet number Pe^* for various water flow rates and gravity levels (+ύg, 1g, -ύg).

comparison, at negative hypergravity where the liquid film is significantly thicker, it is rather impossible to completely heat up the film and to dissipate heat.

In order to point out the effect of gravity and spray impact parameters for the certain gravity regime, Figure 6.8 (a) magnifies linear correlations for positive hypergravity and (b) emphasizes the results for negative hypergravity between the Nusselt number of the liquid film Nu_{film} and the modified Péclet number Pe^*.

In both regimes, the values decrease with an increase of the water flow rate for a constant gravity level. Gravity appears to have a stronger influence in the negative hypergravity regime than at positive hypergravity. There, the data points corresponding to a constant water flow rate are located for all positive hypergravity levels in straight lines. The linear slope defines the Stanton number St since $St = Nu_{film}/Pe^*$.

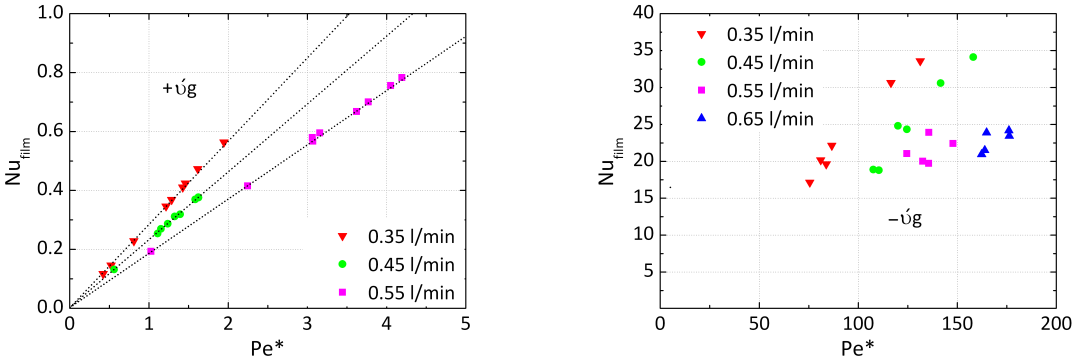

(a) (b)

Figure 6.8: Correlation between the Nusselt number Nu_{film} and the modified Péclet number Pe^* for various water flow rates and gravity levels: (a) +ύg, (b) -ύg

.

Consequently, we can write for positive hypergravity according to Figure 6.8 (a) for the different water flow rates the following expressions

$$Nu_{film} = \begin{cases} 0.28Pe^* & \text{for } 0.35 \text{ l/min} \\ 0.23Pe^* & \text{for } 0.45 \text{ l/min} \\ 0.19Pe^* & \text{for } 0.55 \text{ l/min} \end{cases} \tag{6.6}$$

Hence, there are different Stanton numbers St for a constant water flow rate. Gravity seems not to play an important role.

In Figure 6.9, results for the Stanton number St plotted against the Péclet number Pe are given there for all hypergravity regimes and various water flow rates. At negative hypergravity in Figure 6.9 (a), the values seem again chaotic and unpredictable whereas when zooming in the positive hypergravity in (b), the results confirm our previous statement that gravity has not influence. A consequence of the fact that the Nusselt number Nu_{film} increases linearly with the modified Péclet number Pe^* for the case of positive hypergravity is also confirmed in Figure 6.9 (b). When evaluating the positive hypergravity values for Stanton number St vs. the dimensionless film thickness H and a dimensionless velocity V (using $\overline{U}$ and v), then we come to the same conclusion as shown vs. the modified Péclet number Pe^* in Figure 6.9 (b).

To sum up, the gravitational force appears not directly a driving factor in spray cooling. Also, the characteristic film thickness $\bar{h}_{film}$ is not affecting the results within

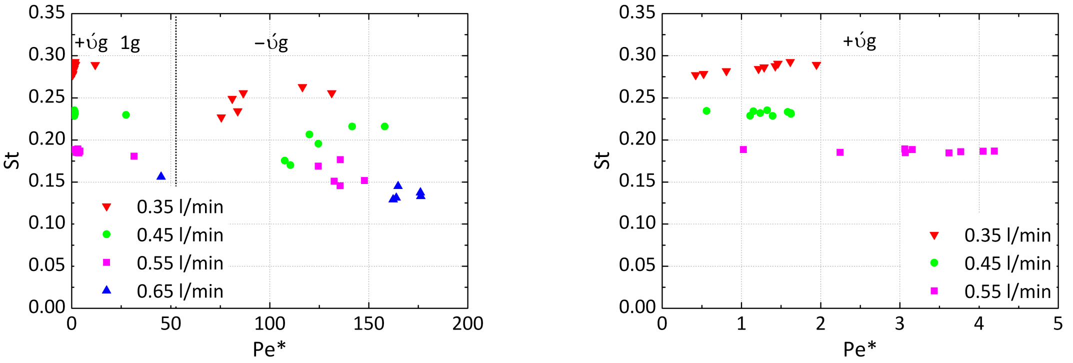

(a) (b)

Figure 6.9: Results for the Stanton number St versus the modified Péclet number Pe^* for various water flow rates $\dot{V}$ and gravity levels: (a) +ύg, 1g, -ύg, (b) zommed in for only positive hypergravity (+ύg).

the different regimes (compare Figure 5.15 for 1g and +ύg and Figure 5.16 for -ύg). Spray cooling appears more efficient when the target is covered by a thin fluctuating liquid film corresponding to a higher velocity field. The convective heat transfer is dominant.

Chapter 7

Summary and outlook

The hydrodynamics of spray-wall interaction is of fundamental interest in numerous industrial applications, among others spray cooling. Hence, it is of utmost importance to understand the fluid flow phenomena that are involved.

In this thesis, spray impact and spray cooling have been investigated under various levels of gravitational force. Experiments were performed at microgravity during parabolic flights and on board a ballistic rocket. Experiments under negative and positive hypergravity (-20g to +20g) were performed in a centrifuge at the Center of Applied Space Technology and Microgravity. Therefore, different physical setups have been constructed for various experimental platforms and modified according to the specific constraints.

The primary spray impinging onto the surface and secondary spray splashing from the surface have been characterized using the Phase Doppler technique and shadowgraphy. Both techniques have been used to determine size and velocity of primary and secondary drops. A robust image processing algorithm for shadowgraphy has been developed for the analysis of the captured images. The data for the secondary spray parameters have been compared with existing semi-empirical correlations, exhibiting a good agreement.

It has been found that the flow in the liquid film is influenced significantly by gravity. At negative hypergravity levels, new hydrodynamic phenomena have been observed. Various modes of spray-wall collision have been identified such as film jetting and drop formation. It has been demonstrated that the effect of gravity on spray impact manifests itself not only in the spray drop size and the drop velocity but also in the morphology of spray-wall interaction.

An image processing tool has been developed that determines in a robust way a characteristic film thickness and its dependence on the gravitational force. With an increase of this force, the liquid film thickness decreases. It has been shown that the characteristic film thickness can be correlated well with the Capillary number.

In a further step, the effect of gravity on spray cooling has been investigated. Heat transfer characteristics have been measured for various spray parameters, gravity levels and wall temperatures. The results have illustrated that the heat transfer coefficient is significantly affected by gravity. However, the spray cooling mechanisms are in fact influenced only indirectly by gravity but directly by the flow in the wall film. It has been demonstrated that the decrease of the averaged characteristic film thickness corresponds to higher heat transfer coefficients. It provides evidence that the decrease of the film thickness is related to a higher liquid velocity and thinner thermal boundary layer. For positive hypergravity levels, the Stanton number correlates well with a modified Péclet number and does not depend on the gravity level. It describes the heat flux over a wide range of spray parameters and for various gravity levels. For negative hypergravity levels the phenomenon becomes even more complicated.

The collected experimental data in this investigation serve as a starting point for the development of a comprehensive universal spray cooling model and, subsequently, for the design and development of improved cooling apparatus.

In spite of the understanding gained through these experiments there remain a number of open questions in the field of spray impact and spray cooling. Even basic and apparently simple elements of spray impact are not trivial and therefore need to be investigated in further experiments over a wider parameter field. Measurements with different nozzle geometries, various injection pressures and consequently different spray densities could be performed in future work. Very dense fuel sprays or measurements at relatively low Reynolds numbers in which the viscosity significantly influences the impact of single drops could be also of interest.

Furthermore, measurements with various target radii and targets with different micro structures could lead to correlations which take into account target geometry and morphology. In this regard, the spray impact on oblique targets by varying the impact angle could be also investigated in order to validate and generalize the developed empirical correlations. In addition, investigations at a higher wall temperature are necessary to broaden the experimental data base. Comparisons with existing spray cooling correlations could be then drawn and may lead to a more profound understanding of the spray cooling mechanisms.

Appendix

Table A.1: Overview of results.

g-level	$\dot{V}$ (l/min)	D_{32} (μm)	U (m/s)	$\bar{h}_{film}$ (μm)	α ($\frac{W}{cm^2K}$)
-20	0.25	644.9857	0.7363	17.7826	-
-16	0.25	920.6098	1.2348	379.0643	-
μ	0.25	901.4555	4.8339	483.1140	-
1	0.25	884.2589	5.5393	132.0145	-
2	0.25	803.0566	259.0993	19.6608	-
4	0.25	637.7771	258.7115	-	-
6	0.25	705.1677	239.4598	-	-
8	0.25	700.1350	253.8883	3.4748	-
10	0.25	784.5984	294.3266	-	-
12	0.25	617.8218	252.1596	0.0611	-
14	0.25	651.3834	228.4489	-	-
16	0.25	570.8338	217.2305	1.1969	-
20	0.25	771.6343	201.0476	0.0611	-
-20	0.35	462.0196	2.1171	581.1567	1.7639
-16	0.35	501.6407	2.1790	644.9514	1.8206
-12	0.35	545.8148	2.5480	623.5684	1.9356
-8	0.35	540.0425	1.8419	666.5755	1.9876
-4	0.35	539.6529	1.0515	896.8324	2.0439

g-level	$\dot{V}$ (l/min)	D_{32} (μm)	U (m/s)	$\bar{h}_{film}$ (μm)	α ($\frac{W}{cm^2K}$)
-2	0.35	490.9632	4.6308	1010.8159	1.9885
μ	0.35	488.2338	6.0258	339.5005	-
1	0.35	496.9781	7.7749	91.2878	2.2485
2	0.35	503.6671	7.0576	14.9861	2.2499
4	0.35	498.0586	7.6520	12.4372	2.2761
6	0.35	484.1431	7.9467	11.2358	2.2604
8	0.35	487.0320	8.4570	10.9800	2.2369
10	0.35	499.6606	8.0527	9.8950	2.2262
12	0.35	480.7717	8.1099	9.3587	2.2116
14	0.35	508.6141	8.1772	6.2307	2.1915
16	0.35	468.4502	8.5073	4.0213	2.1661
20	0.35	466.1986	8.3198	3.2488	2.1550
-20	0.45	377.8566	4.0656	661.3787	1.7015
-16	0.45	379.8474	2.8251	644.2002	1.7539
-12	0.45	373.6952	3.4754	745.8143	1.9534
-8	0.45	348.5677	3.3656	718.9078	2.0652
-4	0.45	353.8499	6.2016	946.0593	2.1582
-2	0.45	356.2782	5.5954	847.8345	2.1596
μ	0.45	405.8953	7.7655	330.2839	-
1	0.45	443.4685	9.8321	164.3469	2.2955
2	0.45	419.2132	9.0574	6.6411	2.2867
4	0.45	383.9726	9.8606	-	2.3399
6	0.45	390.9594	9.7573	-	2.3521
8	0.45	397.9258	9.9029	9.4839	2.3322
10	0.45	364.4896	9.5196	-	2.3086

g-level	$\dot{V}$ (l/min)	D_{32} (μm)	U (m/s)	$\bar{h}_{film}$ (μm)	α ($\frac{W}{cm^2K}$)
12	0.45	376.1954	10.6493	9.7220	2.3181
14	0.45	452.8004	10.3240	-	2.2851
16	0.45	390.6807	10.4652	7.4075	2.3174
20	0.45	393.3279	10.0292	3.3587	2.3429
-20	0.55	-	-	692.8165	1.6021
-16	0.55	346.8027	6.5704	664.0870	1.7774
-12	0.55	302.0106	15.4083	649.3818	1.8440
-8	0.55	340.9346	4.4371	724.1382	1.8530
-4	0.55	340.8907	7.1749	610.1029	2.0640
-2	0.55	322.4865	11.9136	664.3405	2.1555
μ	0.55	401.8027	10.2203	406.1192	-
1	0.55	389.6742	11.3628	154.2291	2.2064
2	0.55	396.2836	11.8758	19.8440	2.2800
4	0.55	439.6783	12.7826	-	2.3133
6	0.55	400.2763	11.8389	-	2.2584
8	0.55	406.3652	11.4268	17.7341	2.2545
10	0.55	452.3059	11.1512	-	2.2714
12	0.55	492.5296	12.6871	20.5402	2.2823
14	0.55	426.7576	12.6541	-	2.2617
16	0.55	419.4467	12.2518	15.4624	2.3041
20	0.55	488.4628	12.6300	5.0228	2.3026
-20	0.65	-	-	765.5026	1.7660
-16	0.65	333.5812	6.6094	730.5137	1.9209
-12	0.65	359.3770	5.1619	672.7495	1.8641
-8	0.65	340.2053	4.8885	679.1403	1.8952

g-level	$\dot{V}$ (l/min)	D_{32} (μm)	U (m/s)	$\bar{h}_{film}$ (μm)	α ($\frac{W}{cm^2K}$)
-4	0.65	342.2014	5.9484	729.7076	1.9840
-2	0.65	300.7520	6.6012	682.8441	2.0939
μ	0.65	452.0904	12.9827	478.8900	-
1	0.65	439.8090	13.6391	187.0944	2.2552
2	0.65	371.8978	12.9319	-	2.1921
4	0.65	348.9044	12.5307	-	2.2478
6	0.65	368.8519	13.2942	-	2.2220
8	0.65	446.6029	12.9683	-	2.2169
10	0.65	419.0960	13.0763	-	2.2303
12	0.65	382.3359	11.8500	-	2.2632
14	0.65	472.9934	13.1789	-	2.2565
16	0.65	388.9103	16.3291	-	2.2487
20	0.65	-	-	-	2.3446

Bibliography

Albrecht H.-E., Borys M., Damaschke N., and Tropea C. (2003). “Laser Doppler and phase Doppler measurement techniques”. In: *Springer-Verlag.* (See pp. 8, 33).

Bachalo W. and Houser M. (1984). “Phase/Doppler spray analyser for simultaneous measurement of drop size and velocity distributions”. In: *Opt. Eng.* 23, pp. 583–590. (See p. 33).

Bai C. and Gosman A. (1995). “Development of methodology for spray impingement simulation”. In: *SAE technical paper series 950283.* (See pp. 1, 12, 13).

Bai C., Rusche H., and Gosman A. (2002). “Modeling of gasoline spray impingement”. In: *Atomization and Sprays* 12, p. 1. (See pp. 12, 13).

Batarseh F. (2008). “Spray generated by an airblast atomizer: atomization, propagation and aerodynamic instability”. In: *Fachbereich Maschinenbau, Technische Universität Darmstadt.* (See pp. XIX–XXI, 75–77, 95).

Bauckhage K. and Flögel H. (1984). “Simultaneous measurement of droplet size and velocity in nozzle sprays”. In: *Proc. 2nd Int Symp of Laser Aneomom to Fluid Mech., Lisbon, Portugal* paper 18.1. (See p. 33).

Baysinger K., Yerkes K., Michalak T., Harris R., and McQuillen J. (2004). “Design of a microgravity spray cooling experiment”. In: *Proc. of the 42nd AIAA Aerospace Sciences Meeting and Exhibit, Reno, NV.* (See p. 19).

Bernardin J., Stebbins C., and Mudawar I. (1997a). “Mapping of impact and heat transfer regimes of water drops impinging on a polished surface”. In: *Int. J. Heat Mass Transfer* 40 [2], pp. 247–267. (See p. 14).

– (1997b). “Effects of surface roughness on water droplet impact history and heat transfer regimes”. In: *Int. J. Heat Mass Transfer* 40 [1], pp. 73–88. (See p. 14).

Böhm C., Weiss D., and Tropea C. (1999). “Multi–droplet impact onto solid walls: droplet–droplet interaction and collision of kinematic discontinuities”. In: *Proc. 15th Ann. Conf. on Liquid Atomization and Spray Systems, Darmstadt.* (See p. 13).

Bolle L. and Moureau J. (1982). “Spray cooling of hot surfaces”. In: *Multiphase Science and Technology, ed. by G.F. Hewitt, J.M. Delhaye, N. Zuber, Hemisphere Publishing Corporation, Washington* 1, pp. 1–97. (See p. 14).

Bonner R., Wadell R., and Popov G. (2008). “Local Heat Transfer Coefficient Measurements of Flat Angled Sprays Using Thermal Test Vehicle”. In: *Semiconductor Thermal Measurement and Management Symposium, Semi-Therm 2008, Twenty-fourth Annual IEEE.* (See p. 2).

Carey V. (1992). “Liquid-Vapor Phase-Change Phenomena”. In: *Taylor & Francis.* (See p. 15).

Celata G., Colin C., Colinet P., Dimarco P., Gambaryan-Roisman T., Kabov O., Kyriopoulos O., Stephan P., Tadrist L., and Tropea C. (2008). “Bubbles, drops, films: transferring heat in space”. In: *Europhysics News* 39, pp. 23–25. (See pp. 2, 97, 101).

Chandra S. and Avedisian C. (1991). “On the collision of a droplet with a solid surface”. In: *Proc. R. Soc. Lond. A* 432, pp. 13–41. (See p. 14).

Chigier N. (2002). “Fluid and particle mechanics of spray painting”. In: *Polymetric materials science and engineering* 38, p. 325. (See p. 1).

Chow L., Sehmbey M., and Behm J. (1996). “Thermal management issues in cryo–electronics”. In: *Proc. 31st Intersociety Energy Conversion Engineering Conference, IECEC* 2, pp. 1367–1372. (See p. 14).

Cossali G., Coghe A., and Marengo M. (1997). “The impact of a single drop on a wetted surface”. In: *Exp. Fluids* 22, p. 463. (See p. 13).

Cossali G., Marengo M., and Santini M. (2005). “Single–drop empirical models for spray impact on solid walls: a review”. In: *Atomization and Sprays* 15, pp. 699–736. (See p. 12).

DLR (2008). “COUNTDOWN 8”. In: *Topics from DLR Space Agency, November* 4/08. (See p. 35).

Durst F. and Zaré M. (1975). “Laser Doppler measurement in two–phase–flows”. In: *Proc. of the LDA Symp Copenhagen, Denmark*, pp. 403–429. (See p. 33).

Dynamics D. (2005). “BSA Flow Software Version 4”. In: *Dantec Dynamics A/S, Denmark.* (See p. 33).

Eres M. and Schwartz L. (2001). “Spraying and spreading processes on moving substrates”. In: *Proc. 4th European coating symposium ECS, Bruxelles, Belgium*, pp. 170–173. (See p. 13).

Estes K. and Mudawar I. (1995). “Correlation of Sauter mean diameter and critical heat flux for spray cooling of small surfaces”. In: *Int. J. Heat Mass Transfer* 38 [16], pp. 2985–2996. (See pp. 2, 17).

Flögel H. (1981). “Untersuchung von Teilchengeschwindigkeit und Teilchengröße mit einem Laser–Doppler–Anemometer”. In: *Universität Bremen, Bremen, Germany.* (See p. 33).

Gambaryan-Roisman T., Kyriopoulos O., Roisman I., Stephan P., and Tropea C. (2007). “Gravity Effect on Spray Impact and Spray Cooling”. In: *Microgravity Sci. Technol.* XIX, N. 3/4, pp. 151–154. (See pp. 11, 99, 101).

Hall D. and Mudawar I. (1995). “Experimental and numerical study of quenching complex-shaped metallic alloys with multiple”. In: *Int. J. Heat Mass Transfer* 38 [7], pp. 1201–1216. (See p. 14).

Han Z., Xu Z., and Trigui N. (2000). “Spray/wall interaction models for multidimensional engine simulation”. In: *Int. J. Engine Research* 1, p. 127. (See pp. 12, 13).

Harlow H. and Shannon J. (1967). “The splash of a liquid drop”. In: *J. Appl. Phys.* 38, p. 3855. (See p. 13).

Horacek B., Kiger K., and Kim J. (2005). “Single nozzle spray cooling heat transfer mechanisms”. In: *Int. J. Heat and Mass Transfer* 48, pp. 1425–1438. (See pp. 17, 18).

Huddle J., Chow L., Lei S., Marcos A., Rini D., Lindauer S., Bass M., and Delfyett P. (2000). “Thermal management of diode laser arrays”. In: *Proc. 16th Annual IEEE Semiconductor Thermal Measurement and Management Symposium*, pp. 154–160. (See p. 14).

Incropera F. and Dewitt D. (1990). “Fundamentals of Heat and Mass Transfer”. In: *John Wiley & Sons, New York.* (See p. 2).

Kim J. (2007). “Spray cooling heat transfer: The state of the art”. In: *Int. J. Heat and Fluid Flow* 28, pp. 753–767. (See pp. 2, 14, 15, 21).

Kyriopoulos O., Roisman I., Gambaryan-Roisman T., Stephan P., and Tropea C. (2006). “Hydrodynamics and heat transfer of spray/wall interaction: hardware and results of the 44th (ESA) and 9th (DLR) parabolic flight campaigns”. In: *Topical Team "DOLFIN" workshop, Darmstadt, Germany.* (See p. 22).

– (2007). “Spray impact: hydrodynamics and heat transfer under microgravity conditions”. In: *3rd Int. Symp. on Physical Science in Space, Nara, Japan.* (See p. 97).

– (2008a). “Dynamics of a liquid film produced by spray impact onto a heated target”. In: *Jap. Soc. Micro. Appl. Journal* 25, 3, pp. 231–234. (See pp. 86, 88, 89).

– (2008b). “Dynamics of a liquid film produced by spray impact onto a heated target”. In: *ILASS 2008, Sep.8-10, 2008, Como Lake, Italy.* (See p. 99).

– (2008c). “Liquid Film Dynamics and Spray Cooling: Sounding Rocket Experiment”. In: *Third International Topical Team Workshop on Two-Phase Systems for Ground and Space Applications, Brussels, Belgium.* (See p. 99).

Kyriopoulos O., Roisman I., and Tropea C. (2009a). “Dynamics of the Film produced by Spray Impact under Various Gravity Levels”. In: *ICLASS 2009, 11th Triennial*

International Annual Conference on Liquid Atomization and Spray Systems, Vail, Colorado USA, July 2009. (See p. 84).

Kyriopoulos O., Roisman I., Gambaryan-Roisman T., Stephan P., and Tropea C. (2009b). “Gravity Effect on Liquid Film Dynamics produced by Spray Impact onto a Heated Target and on Spray Cooling”. In: *Fourth International Topical Team Workshop on Two-Phase Systems for Ground and Space Applications, Novosibirsk, Russia.* (See p. 84).

Lee G., Jin Y., Park S., Ajmera P., Malek C., Wang J., and Tang F. (1999). “LIGA–like process for high–aspect ratio PZT microstructures”. In: *Proceedings of the 1999 Smart Structures and Materials - Smart Electronics and MEMS; Newport Beach, CA, USA.* (See p. 2).

Lee J. and Bergman T. (2001). “Scaling analysis and prediction of thermal aspects of the plasma spraying process using a discrete particle approach”. In: *J. Thermal Spray Technology* 11, p. 179. (See p. 13).

Lefebvre A. (1989). “Atomization and Sprays”. In: *Hemisphere Publishing Corporation, New York.* (See p. 8).

Li C., Wang Z., Wang P., Peles Y., Koratkar N., and Peterson G. P. (2008). “Nanostructured Copper Interfaces for Enhanced Boiling”. In: *Small* 4.8, pp. 1084–1088. DOI: `10.1002/smll.200700991`. (See pp. 17, 18).

Lu G., Peng X.-F., and Wang X. (2008). “An Experimental Investigation on Spreading of Droplets with Evaporation and Nucleation”. In: *Heat Transfer* 38 [1].8, pp. 40–50. DOI: `10.1002/smll.200700991`. (See p. 17).

Marconi E. (2004). “What is a Sounding Rocket?” In: *Research Aircraft, NASA.* (See p. 37).

Marengo M. (1999). “Aufprall von Tropfen auf Flüssigkeitsfilme”. In: *Final report for project Tr 194/10, Deutsche Forschungsgemeinschaft, FG-SLA, TU Darmstadt.* (See p. 13).

Matsui Y. and Sugihara K. (1986). “Sources of Hydrocarbon Emmisions from a Small Direct”. In: *Injection Diesel Engines, JSAE Review.* (See p. 1).

Mühlbauer M. (2009). “Modelling wall interactions of a high–pressure, hollow cone spray”. In: *Fachbereich Maschinenbau, Technische Universität Darmstadt.* (See p. 97).

Mudawar I. (2000). “Assessment of high–heat–flux thermal management schemes”. In: *Proc. 7th Intersociety Conference on Thermal and Thermomech. Phenomena in Electronic Systems, ITHERM*, pp. 1–20. (See p. 14).

Mudawar I. and Deiters T. (1994). "A universal approach to predicting temperature response of metallic parts to spray quenching". In: *Int. J. Heat Mass Transfer* 37 [3], pp. 347–362. (See pp. 14, 17).

Mudawar I. and Valentine W. S. (1989). "Determination of the local quench curve for spray–cooled metallic surfaces". In: *ASME J. of Heat Treating* 7, pp. 107–121. (See p. 17).

Mundo C. (1996). "Zur Sekundärzerstäubung newtonscher Fluide an Oberflächen". In: *Universität Erlangen-Nürnberg.* (See p. 12).

Mundo C., Sommerfeld M., and Tropea C. (1998). "On the modeling of liquid sprays impinging on surfaces". In: *Atomization and Sprays* 8, p. 625. (See pp. 7, 13, 75).

Mustafic I., Gambaryan-Roisman T., Roisman I., Stephan P., and Tropea C. (2004). "Liquid flow produced by spray impact onto a curved rigid wall". In: *ILASS 2004, Orléans, France.* (See pp. 11, 95).

Naber J. and Reitz R. (1988). "Modeling engine spray/wall impingement". In: *SAE Technical Paper Series* 880107. (See p. 12).

Nasr G. G., Yule J., and Bending L. (2002). "Industrial Sprays and Atomization, Design and Applications". In: *Springer-Verlag London.* (See p. 7).

Oguz H. and Prosperetti A. (1990). "Bubble entrainment by the impact of drops on liquid surfaces". In: *J. Fluid Mech.* 219, p. 143. (See p. 13).

Pais M., Chow L., and Mahefkey E. (1992). "Surface roughness and its effects on the heat transfer mechanism in spray cooling". In: *ASME J. of Heat Transfer* 114, pp. 211–219. (See p. 18).

Panão M. and Moreira A. (2009b). "Intermittent spray cooling: A new technology for controlling surface temperature". In: *International Journal of Heat and Fluid Flow* 30 [1].1, pp. 117–130. DOI: `10.1016/j.ijheatfluidflow.2008.10.005`. (See p. 20).

– (2009a). "Heat transfer correlation for intermittent spray impingement: A dynamic approach". In: *International Journal of Thermal Sciences* 48 [10].10, pp. 1853–1862. DOI: `10.1016/j.ijthermalsci.2009.02.018`. (See pp. 17, 20, 21).

Park K. and Watkins A. (1996). "Comparison of wall spray impaction models with experimental data on drop velocities and sizes." In: *Int. Journal of Heat and Fluid Flow* 17, pp. 424–438. (See p. 12).

Rioboo R., Marengo M., and Tropea C. (2001). "Outcomes from a drop impact on solid surfaces". In: *Atomization and Sprays* 11, p. 155. (See p. 13).

Roisman I., Horvat K., and Tropea C. (2006). "Spray impact: rim transverse instability initiating fingering and splash, and description of a secondary spray". In: *Phys. Fluids* 18, p. 102. (See pp. XIV, XIX, XX, 10–12, 70–72, 75–77, 80).

Roisman I., Gambaryan-Roisman T., Kyriopoulos O., Stephan P., and Tropea C. (2007). "Breakup and Atomization of a Stretching Crown". In: *Phys. Rev. E* 76, p. 026302. (See pp. 9, 12, 79, 80, 84).

Roisman I., Van Hinsberg N. P., and Tropea C. (2008). "Propagation of a Kinematic Instability in a Liquid Layer: Capillary and Gravity Effects". In: *Phys. Rev. E* 77, p. 046305. (See pp. 93, 94).

Samenfink W. (1997). "Grundlegende Untersuchung zur Tropfeninteraktion mit schubspannungsgetriebenen Wandfilmen". In: *Ph.D. Thesis, Universität Karlsruhe, Karlsruhe, Germany.* (See pp. 12, 13).

Satas D. (1984). "Web Processing and Converting Technology and Equipment". In: *Van Nostrand Reinhold, New York,* (see p. 1).

Sehmbey M., Chow L., Hahn O., and Pais M. (1995). "Spray cooling of power electronics at cryogenic temperatures". In: *J. of Thermophysics and Heat Transfer* 9 [1], pp. 123–128. (See p. 14).

Senda J., Kobayashi S., Iwashita S., and Fujimoto H. (1994). "Modeling of diesel spray impingement on a flat wall." In: *SAE Technical Paper Series* 941894. (See p. 12).

Senda J., Kanda T., Al-Roub M., Farell P., Fukami T., and Fujimoto H. (1997). "Modeling spray impingement considering fuel film formation on the wall". In: *SAE Technical Paper Series* 970047. (See p. 12).

Silk E. and Bracken P. (2010). "Spray Cooling Heat Flux Performance Using POCO HTC Foam". In: *Journal of Thermophysics and Heat Transfer* 24 [1].1, pp. 157–164. DOI: `10.2514/1.44089`. (See p. 18).

Silk E., Kim J., and Kiger K. (2004). "Investigation of enhanced surface spray cooling". In: *Proceedings of ASME International Mechanical Engineering Congress, November 13-19, 2004, Anaheim, California, USA.* (See p. 18).

Silk E., Golliher E., and Paneer Selvam R. (2008). "Spray cooling heat transfer: Technology overview and assessment of future challenges for micro–gravity application". In: *Energy Conversion and Management* 49, pp. 453–468. DOI: `10.1016/j.enconman.2007.07.046`. (See pp. 17, 19).

Sone K., Yoshida K., Oka T., Abe Y., Mori Y., and Nagashima A. (1996). "Spray cooling characteristics of water and FC–72 under reduced and elevated gravity for space applications". In: *Proc. 31st Intersociety Energy Conversion Engineering Conference, IECEC 96* 2, pp. 1500–1505. (See p. 19).

Srikar R., Gambaryan-Roisman T., Steffes C., Stephan P., Tropea C., and Yarin A. (2009). "Nanofiber coating of surfaces for intensification of drop or spray impact cooling". In: *International Journal of Heat and Mass Transfer* 52 [25-26].25-26, pp. 5814–5826. DOI: `10.1016/j.ijheatmasstransfer.2009.07.021`. (See pp. 17, 18).

Stanton D. and Rutland C. (1996). "Modeling fuel film formation and wall interaction in diesel engines". In: *SAE technical paper series 960628*. (See pp. 12, 13).

– (1998). "Multi–dimensional modeling of heat and mass transfer of fuel films resulting from impinging sprays". In: *SAE technical paper series 980132*. (See p. 12).

Strotos G., Gavaises M., Theodorakakos A., and Bergeles G. (2008a). "Numerical investigation of the cooling effectiveness of a droplet impinging on a heated surface". In: *International Journal of Heat and Mass Transfer* 51 [19-20].19-20, pp. 4728–4742. DOI: `10.1016/j.ijheatmasstransfer.2008.02.036`. (See p. 20).

– (2008b). "Numerical investigation on the evaporation of droplets depositing on heated surfaces at low Weber numbers". In: *International Journal of Heat and Mass Transfer* 51[7-8].7-8, pp. 1516–1529. DOI: `10.1016/j.ijheatmasstransfer.2007.07.045`. (See pp. 17, 21).

Thomson W. T. (1986). "Introduction to Space Dynamics". In: *Dover*, p. 91. (See p. 35).

Tilton D., Tilton C., Pais M., and Morgan M. (1992). "High–flux spray cooling in a simulated chip module". In: *Topics in Heat Transfer* 206-2, pp. 73–79. (See p. 14).

Tilton D., Tilton C., Moore C., and Ackerman R. (1994a). "Spray cooling for the 3–D cube computer". In: *Proc. Intersociety Conf. on Thermal Phenomena in Electronic Systems, I-THERM IV*, pp. 169–176. (See p. 14).

Tilton D., Kearns D., and Tilton C. (1994b). "Liquid nitrogen spray cooling of a simulated electronic chip". In: *Advances in Cryogenic Engineering* 39, pp. 1779–1785. (See pp. 2, 14).

Toda S. (1972). "A Study of mist cooling (1st Report: Investigation of Mist Cooling)". In: *Heat Transfer - Japanese Research* 2, pp. 39–50. (See p. 17).

Torres J., Nelson J., Milner T., Goodman D., and Anvari B. (1999). "Estimation of internal skin temperature in response to cryogen spray cooling: Implications for laser therapy of port wine stains". In: *IEEE Journal of Selected Topics in Quantum Electronics* 5 [4], pp. 1058–1066. (See pp. 2, 14).

Tropea C. and Roisman I. (2000). "Modeling of spray impact on solid surfaces". In: *Atomization and Sprays* 10, p. 387. (See p. 12).

Visaria M. and Mudawar I. (2008). "Theoretical and experimental study of the effects of spray inclination on two–phase spray cooling and critical heat flux". In: *International journal of heat and mass transfer* 51 [9-10].9-10, pp. 2398–2410. DOI: `10.1016/j.ijheatmasstransfer.2007.08.010`. (See pp. 17, 18).

Wendelstorf J., Spitzer K., and Wendelstorf R. (2008). “Spray water cooling heat transfer at high temperatures and liquid mass fluxes”. In: *International Journal of Heat and Mass Transfer* 51 [19-20].19-20, pp. 4902–4910. DOI: `10.1016/j.ijheatmasstransfer.2008.01.032`. (See pp. 17, 20).

Worthington A. M. (1908). “A Study of Splashes”. In: *Longmans & Green, London.* (See p. 6).

Yarin A. (2006). “Drop impact dynamics: Splashing, Spreading, Receding, Bouncing”. In: *Annu. Rev. Fluid Mech.* 38, pp. 159–192. (See pp. 6–8, 75).

Yarin A. and Weiss D. (1995). “Impact of drops on solid surfaces: self–similar capillary waves, and splashing as a new type of kinematic discontinuity”. In: *J. Fluid Mech.* 283, p. 141. (See p. 13).

Yoshida K.-I., Abe Y., Oka T., Mori Y., and Nagashima A. (2001). “Spray cooling under reduced gravity condition”. In: *ASME J. of Heat Transfer* 123, pp. 309–318. (See pp. 17, 19).

Curriculum Vitae

	Dipl.-Ing. Olympia Natalia Kyriopoulos
August 10, 1981	Born in Darmstadt, Germany
Since 07/2010	System Engineer at VEGA Deutschland GmbH Darmstadt, Germany
05/2006 - 03/2010	Research Assistant at the Chair of Fluid Mechanics and Aerodynamics Technische Universität Darmstadt, Darmstadt, Germany
09/2005 - 04/2006	Journey around the world
10/2000 - 09/2005	Studies of Mechanical and Process Engineering Degree of Diplom-Ingenieur, Technische Universität Darmstadt Darmstadt, Germany
08/2003 - 05/2004	Scholarship by DAAD (Deutscher Akademischer Austausch Dienst) for studies abroad, University of California, Berkeley, U.S.A.
08/1991 - 06/2000	Edith-Stein-Schule State-approved Catholic gymnasium (highschool), Darmstadt, Germany
08/1987 - 06/1991	Erich-Kästner-Schule Primary school, Darmstadt, Germany

Darmstadt, July 07, 2010